

박사 학위논문
Ph. D. Dissertation

이차원 푸리에 변환 분광학에서의 양자 제어

Quantum Control in Two-Dimensional Fourier Transform Optical
Spectroscopy



임종석 (林鍾碩 Lim, Jongseok)

물리학과

Department of Physics

KAIST

2011

이차원 푸리에 변환 분광학에서의 양자 제어

Quantum Control in Two-Dimensional Fourier Transform Optical
Spectroscopy



Quantum Control in Two-Dimensional Fourier Transform Optical Spectroscopy

Advisor : Professor Ahn, Jaewook

by

Lim, Jongseok

Department of Physics

KAIST

A thesis submitted to the faculty of KAIST in partial fulfillment of the requirements for the degree of Doctor of Philosophy in the Department of Physics . The study was conducted in accordance with Code of Research Ethics¹.

2011. 04. 29.

Approved by

Professor Ahn, Jaewook

[Advisor]

¹Declaration of Ethical Conduct in Research: I, as a graduate student of KAIST, hereby declare that I have not committed any acts that may damage the credibility of my research. These include, but are not limited to: falsification, thesis written by someone else, distortion of research findings or plagiarism. I affirm that my thesis contains honest conclusions based on my own careful research under the guidance of my thesis advisor.

이차원 푸리에 변환 분광학에서의 양자 제어

임 종 석

위 논문은 한국과학기술원 박사학위논문으로
학위논문심사위원회에서 심사 통과하였음.

The logo for KAIST (Korea Advanced Institute of Science and Technology) is displayed in a light blue, sans-serif font. The letters are bold and spaced out, with a subtle shadow effect beneath the text.

2011년 04월 29일

심사위원장 안 재 욱 (인)

심사위원 이 호 성 (인)

심사위원 남 창 희 (인)

심사위원 김 병 윤 (인)

심사위원 조 용 훈 (인)

DPH
20057512

임종석. Lim, Jongseok. Quantum Control in Two-Dimensional Fourier Transform Optical Spectroscopy. 이차원 푸리에 변환 분광학에서의 양자 제어. Department of Physics . 2011. 72p. Advisor Prof. Ahn, Jaewook. Text in English.

ABSTRACT

The ability of controlling the evolution of quantum systems by applying interaction with shaped laser pulse, known as coherent control or quantum control, has attracted significant interest in many fields of researches over the last two decades. Coherent control has been applied to photo-induced selective chemical reaction processes, controlling the direction of electron motions in semiconductors, multi-photon excitation fluorescence microscopy, and the optimization of nonlinear light-matter interactions. Quantum systems subjected to control have been ranged from atoms and molecules to semiconductors and biological samples. Especially, great efforts have been devoted to managing the transition probabilities between quantum states in atomic systems.

Previous transition probability controls are mostly restricted to a ladder-type system. The controlled transition in a ladder-type system is readily monitored by detecting the fluorescence decay from a target excited state. On the other hand, the two-photon transition between the excited states in a V -type quantum system is not straightforward to measure, and thus has been difficult to control. It is because the state population of the target excited state is coherently mixed with the dominant one-photon transition population from the ground state. This difficulty is overcome, in this thesis, with the combined use of two-dimensional Fourier-transform optical spectroscopy and a coherent control technique.

In this thesis, we present a new method that harnesses coherent control capability to two-dimensional Fourier-transform optical spectroscopy. For this, three ultrashort laser pulses are individually shaped to prepare and control the quantum interference involved in two-photon inter-excited state transitions of a V -type quantum system. In experiments performed with atomic rubidium, quantum control for enhancement and annihilation of $5P_{1/2} \rightarrow 5P_{3/2}$ transition is successfully tested, where the engineered transitions are distinguishably extracted in the presence of dominant one-photon transitions. Experiments for quantum interference engineering have revealed that the target transition strength is tripled in spectral phase-shaping, and enhanced by 60% in spectral amplitude shaping. Also, we show that the conventional coherent transients in a simple two-level system is mimicked by two-photon coherent control in a V -type three-level system. Here, higher order chirps of a shaped laser pulse play the roles of time and linear chirp in coherent transients. In a three-pulse coherent control experiment of atomic rubidium, the phase and amplitude of controlled transition probability is retrieved from a 2D Fourier-transform spectral peak.

Finally, we propose the application of the novel coherent control technique or advanced two-dimensional Fourier transform spectroscopy to semiconductor quantum well systems. For this, we have considered semiconductor heterostructures made of III-V compounds for the V -type three-level systems along with numerical calculations. It is hoped that the devised coherent control for excited-state transitions become useful in untangle the unknown nature of chemical and biological reaction processes.

Keywords: coherent control, 2D Fourier transform optical spectroscopy, inter-excited state transition, two-photon transition, rubidium atom

Contents

Abstract	i
Contents	ii
List of Tables	iv
List of Figures	v
Chapter 1. Introduction	1
Chapter 2. Review of coherent control	4
2.1 Femtosecond pulse shaping	6
2.1.1 Spatial light modulator	6
2.1.2 Acousto-optic pulse shaper	7
2.2 Adaptive coherent control	10
2.3 Analytic coherent control	11
2.3.1 Resonant two-photon transition	11
2.3.2 Coherent transients	14
Chapter 3. 2D Fourier transform optical spectroscopy	20
3.1 Electric field notation	20
3.2 Inter-excited state transitions in a V -type system	23
3.3 Three pulse coherent control scheme	25
Chapter 4. 2D Fourier transform coherent control spectroscopy (2D-FTCCS)	31
4.1 Experimental description	31
4.2 Controlled preparation of quantum systems	34
4.3 Coherent control of inter-excited state transition	34
4.3.1 Control of transition order	36
4.3.2 Quantum interference engineering	41
Chapter 5. Coherent transients in a V-type three-level system	45
5.1 Transitions in a ladder system	46
5.2 Coherent transients in a two-level system	47
5.3 Coherent transients mimicked in atomic rubidium	49

Chapter 6.	Shaped pulse 2D-FTOS in Quantum wells	55
6.1	Non-uniform continuum density of states on Fano resonance . .	55
6.2	Semiconductor quantum well V-type systems	61
Chapter 7.	Conclusion	66
References		67
Summary (in Korean)		73



List of Tables

3.1 Probability amplitude coefficients of $|b\rangle$ are sorted in accordance with the phase dependence on inter-pulse delays. $|b\rangle$ in Eq. (3.37) can be retrieved from this table: for example, the coefficient of fourth line, $\alpha_{ag}^{(1)}\beta_{ba}^{(2)}$, times phase dependence on τ_1 , $e^{i(\Delta\omega_{bg}-\Delta\omega_{ag})\tau_1}$, times phase dependence on τ_2 , unity, equals $\alpha_{ag}^{(1)}\beta_{ba}^{(2)}e^{i(\Delta\omega_{bg}-\Delta\omega_{ag})\tau_1}\dots\dots\dots$ 27



List of Figures

2.1	Quantum coherent control influencing the evolution of a wavefunction. The system's initial wavefunction ψ_i evolves to a coherent superposition of the all possible final states $\psi_f^{(n)}$ under the influence of the control-free Hamiltonian H_o . On the other hand, with an externally controlled term added to the Hamiltonian, for example, the interaction with a control laser pulse (electric field) in our case, the wavefunction evolution is directed along the desired direction to the target state.	5
2.2	Schematic of femtosecond pulse shaping in frequency domain with spatial light modulator. Gratings and lenses are arranged in a 4f configuration. The pulse shaping procedure is described in the text. [32]	7
2.3	(a) AOPDF top view. The output beam is diffracted by 1 degree from the input beam, in the 90-degree-rotated linear polarization. (b) Schematic of AOPDF. Mode 1 in fast ordinary axis and mode 2 in slow extraordinary axis, are coupled by acousto-optic interaction when the phase matching condition is satisfied. [38]	9
2.4	Synthesis of the pulse shaping function parameters of the acoustic wave. Acoustic wave parameters are categorized into amplitude shaping and phase shaping parts. The frequency domain acoustic wave is Fourier transformed to the time domain signal and applied to the acousto-optic medium via a transducer.	10
2.5	Experimental setup of adaptive coherent control. A SLM or femtosecond pulse shaper is used to shape the pulse with a help of feedback signal and closed-loop learning algorithm. The learning algorithm iteratively finds optimum pulses for different types of experiments.	12
2.6	(a) Drawing of the MLCT chromophore $[Ru(dpb)_3]^{2+}$. (b) Normalized absorption (dashed line) and emission spectra (solid line) collected for the molecule dissolved in methanol at 298 K. (c) The schematic of the control methodology where multiphoton absorption of a shaped 800 nm laser pulse excites the 1MLCT band, and emission from the lower energy 3MLCT state accessed via nonradiative relaxation is used as a feedback signal. [43]	13
2.7	Experimental results of adaptive control on $[Ru(dpb)_3](PF_6)_2$. Solid circles are for maximization and open circles are for minimization of the ratio excitation/SHG. [43]	13
2.8	Energy level diagram of a resonant TPA in Rb. The frequencies of the 5S-5P (ω_{ig}) and 5P-5D (ω_{fi}) resonant transitions correspond to 780.2 nm and 776.0 nm, respectively. The pulse spectrum is centered on the two-photon transition frequency ($\omega_{fg}/2$) at 778.1 nm, with a bandwidth of $\Delta\omega = 18nm$ (FWHM). The excited atoms spontaneously decay to the ground level through the 6P, emitting a fluorescence signal at ω^{flr} (≈ 420 nm) [14].	15

2.9	Experimental and calculated results performed on resonant two-photon transition in Rb atom. (a) Schematic expression of tested scheme: spectral components of the pulse was blocked symmetrically around $\omega_{fg}/2$ by an adjustable slit. (b) The transmitted power of the pulse (diamonds) and the experimental results of detected fluorescence (circles) and calculated transition(line). The two-photon transition doubled when the cutoff wavelengths approached the resonant transition wavelengths. (c) Calculated temporal intensities of the optimal shaped pulse (solid curve) and the transform-limited pulse (dashed lines), normalized to peak intensity of the transform-limited pulse. . [14]	16
2.10	Excitation scheme of rubidium. τ is the pump-probe delay. [46]	18
2.11	(a) Calculation results of excited transient population with unshaped (in amplitude) chirped pump pulse (black line) and with hole-shaped (in amplitude) in time domain chirped pulse (solid gray line) as the inset. The amount of chirp is same for both pulses. (b) Experimental results of excited state population (dots) and numerical calculation (line) with the pulse hole-shaped chirped pulse, with $\phi'' = -4.9 \times 10^5 fs^2$. [46]	19
3.1	(a) Energy diagram of a V-type three-level system with one ground state $ g\rangle$ and two excited states $ a\rangle$ and $ b\rangle$. The transition energies of $ a\rangle$ and $ b\rangle$ from $ g\rangle$ are $\hbar\omega_a$ and $\hbar\omega_b$, respectively. The transition between $ a\rangle$ and $ b\rangle$ via $ g\rangle$ is presented by a red line and transition between $ b\rangle$ and $ g\rangle$ by a blue line. (b) 2D Fourier transformed spectra $S(\omega_1, \omega_2)$. The peak positions contain the transition pathways, and, for example, the transition $ a\rangle \rightarrow b\rangle$ is presented by the red circle, and the transition $ g\rangle \rightarrow b\rangle$ by the blue circle.	21
3.2	Peaks of 2D Fourier transform plane of $ \langle b \psi\rangle ^2$ state population coefficients (left part). Row and column are Fourier transform of τ_1 and τ_2 respectively, and categorized with the coefficients of τ_1 and τ_2 . This table directly map the dependence of peak values of 2D-FT spectra on the three pulse transitions. For example, the peak at $(\Delta\omega_{ag}, \Delta\omega_{bg})$ represents the quantum interference between $ g\rangle \rightarrow a\rangle \rightarrow b\rangle \rightarrow$ and $ g\rangle \rightarrow b\rangle$ transitions. Note that, (n, m) coefficient, where n is row index and m is column index, is complex conjugate of (8-n, 8-m) coefficient.	29
3.3	Peaks of 2D Fourier transform plane of $ \langle b \psi\rangle ^2$ state population coefficients (right part). Row and column are Fourier transform of τ_1 and τ_2 respectively, and categorized with the coefficients of τ_1 and τ_2 . This table directly map the dependence of peak values of 2D-FT spectra on the three pulse transitions. For example, the peak at $(\Delta\omega_{ag}, \Delta\omega_{bg})$ represents the quantum interference between $ g\rangle \rightarrow a\rangle \rightarrow b\rangle \rightarrow$ and $ g\rangle \rightarrow b\rangle$ transitions. Note that, (n, m) coefficient, where n is row index and m is column index, is complex conjugate of (8-n, 8-m) coefficient.	30
4.1	(a) Schematic representation of the experimental setup. (b) Pulse shaping scheme. The first pulse had a spectral hole around D_2 transition and the second pulse was pulse-shaped in various methods correspond to experimental purposes. The shaped pulse sequence wwas applied to gaseous Rb and the spectrally filtered fluorescence signal was detected with a PMT. [49]	33

4.2	(a) Experimental fluorescence data of 2D-FTOS measurement given as a function of two time delays, τ_1 and τ_2 . (b) 2D Fourier-transformed spectrum $S(\omega_1, \omega_2)$ obtained from the time domain data (a). (c) Fluorescence signal decayed from $ b\rangle$ for the three pulses described in the text. (d) 2D Fourier spectrum of (c).	35
4.3	(a) Schematic diagram of the pulse shaping scenario. The first pulse has a spectral hole around D_2 transition and the second pulse is pulse-shaped to control the inter-excited state transition. The third pulse is unshaped. The three pulses are applied to gaseous Rb atom and the fluorescence signal is detected with a PMT. Depending on the chirp sign, the sequence of D_1 and D_2 transitions is time-reversed. The positive chirp case is illustrated in (b) and the negative chirp case in (c). The circled numbers indicate the transition sequence. [49]	37
4.4	Numerical calculation results of 2D Fourier transform spectra, $S(\omega_1, \omega_2)$, for the linearly chirped second pulses of the two different chirp coefficients: (a) $-1 \times 10^3 \text{ fs}^2$, and (b) $1 \times 10^3 \text{ fs}^2$. The peak at $(\omega_{ag} - \omega_0, \omega_{bg} - \omega_0)$ denotes the the controlled transition $ a\rangle \rightarrow b\rangle$.	38
4.5	Experimental results of 2D FT spectra $S(\omega_1, \omega_2)$ for shaped pulses with the five different chirp coefficients: (a) $-1 \times 10^3 \text{ fs}^2$, (b) $-5 \times 10^2 \text{ fs}^2$, (c) zero, (d) $5 \times 10^2 \text{ fs}^2$, and (e) $1 \times 10^3 \text{ fs}^2$. The peaks at $(\omega_{ag} - \omega_0, \omega_{bg} - \omega_0)$ are marked by white arrows which represent the target two-photon process, $5P_{1/2} \rightarrow 5P_{3/2}$. (f) Extracted peak amplitudes at $(\omega_{ag} - \omega_0, \omega_{bg} - \omega_0)$ plotted as a function of chirp of the second pulses (circles) are compared with the numerical calculation of $c_{ba}^{(2)}$ (line).	40
4.6	(a)-(c) Experimental results of 2D Fourier transformed spectra $S(\omega_1, \omega_2)$ in contour map representation for linear chirp values of (a) -1000 fs^2 , (b) zero, and (c) 1000 fs^2 . The peaks $(\omega_{ag} - \omega_0, \omega_{bg} - \omega_0)$ are marked by black arrows. (d)-(f) The $5S_{1/2}$ (blue line), $5P_{1/2}$ (dashed line), and $5S_{3/2}$ (red line) populations, as well as the field envelope (solid black line), corresponding to (a), (b), and (c) respectively.	42
4.7	(a) Experimental and theoretical results for the quantum interference engineering. Dots: measured transition amplitude absolutes, dashed line: numerical calculation based on Eq. (4.6), solid line: numerical calculation considering the spectrally smeared phase (see the text). Insets: (upper-left) the phase diagram for the three transition components in Eq. (4.7), (lower-right) the laser spectrum with block spectral phase, where the block spectral phase ϕ_b represents the relative phase of the spectral region in $[\omega_{ag}, \omega_{bg}]$ with respect to the other. (b-d) The phase diagrams for the maximal (b,d) and the minimal (c) quantum interference conditions. [49]	43
4.8	Coherent enhancement experiment of the $5P_{1/2} \rightarrow 5P_{3/2}$ transition of Rb by spectral amplitude shaping. The measured transition probability amplitudes, normalized to the full spectrum limit (dots), are plotted along with the calculated data (dark line) as a function of the cutoff wavelength. The laser spectrum is shown in gray line. The inset illustrates the spectral shape used in the experiment. The dashed lines are the D_1 and D_2 resonant wavelengths. [49]	44
5.1	Calculated transition probability amplitude from $ a\rangle$ to $ b\rangle$ via an intermediate state $ g\rangle$ using the Eq. (5.23): (a) is the resonant part (the first term), and (b) the nonresonant part (the second term).	51

5.2	(a) Numerical calculation of $ c_{ba}^{(2)} $ plotted as a function of linear and quadratic chirps. (b) Extracted amplitudes of $(\omega_{ag} - \omega_0, \omega_{bg} - \omega_0)$ peaks of 2D Fourier transformed spectra (experimented for the white rectangular area in (a); interpolated twice from 13×7 measurements.) (c)-(e) Two-photon transition amplitudes ($c_{ba}^{(2)}$) drawn in the complex plane as a function of linear chirp, (c) for quadratic chirp $-5 \times 10^4 \text{ fs}^3$, (d) for $-1 \times 10^4 \text{ fs}^3$, and (e) for $3 \times 10^4 \text{ fs}^3$, respectively. [60]	52
5.3	(a) Extracted transition probabilities from the experimental 2D-spectra at $(\omega_{ag} - \omega_0, \omega_{bg} - \omega_0)$ peaks (circles) together with the numerical calculations of $5P_{1/2}$ - $5P_{3/2}$ transition (lines) as a function of linear chirp for quadratic chirp of the second pulse, (a) $-5 \times 10^4 \text{ fs}^3$, (b) $-3 \times 10^4 \text{ fs}^3$, (c) $-1 \times 10^4 \text{ fs}^3$, (d) $1 \times 10^4 \text{ fs}^3$, (e) $3 \times 10^4 \text{ fs}^3$, (f) $5 \times 10^4 \text{ fs}^3$, and (g) $7 \times 10^4 \text{ fs}^3$. The left panel, sub-labeled with -I, shows the absolute value of $c_{ba}^{(2)}$, and the central panel (II) is the complex plane representation of $c_{ba}^{(2)}$. The reconstructed Cornu spirals are shown in the right panel (III) following the process explained in the context.	54
6.1	Schematic exciton energy diagram of a localized state and a Wannier-Stark mini-band in a quantum-well superlattice under an external electric Stark field. As the field varies, the mini-band becomes lifted in energy, then, the localized state couples to lower-energy states of the band. For a sufficiently wide window of field strength, the whole parabolic shape of the density of the mini-band states can play a role.	56
6.2	Excitonic spectra of a $97/17 \text{ \AA}$ superlattice for different bias Stark fields, measured in reflection.	58
6.3	(a) The conventional Fano coupling parameter Γ (asterisks) and the “bare” coupling parameter Γ_o (circles) which compensates the effects of the density of continuum states, depicted as a function of the Stark field for the hh_{-1} transition. (b) The Fano shape parameter q (asterisks) and the Fano “bare” shape parameter q_o (circles).	60
6.4	Fano resonance of an exciton state with neighboring extended Wannier-Stark states. Between the resonant couplings with the next nearest neighboring WS state in (I) and with the nearest neighboring WS state in (III), the exciton state resonantly sweeps through the energy interval, having the minimal coupling somewhere in between as in (II). The effective density of states felt by the exciton states as a function of bias electric field shows a parabolic behavior.	62
6.5	Bandgap energy and lattice constant of various III-V compounds at room temperature (adopted from Tien 1988).	63
6.6	(a) Band diagram of the double-quantum well structure and the energies of the bound states. Band diagrams are shown in black (valence band) and gray (conduction band) lines, and the excited states energies in pink (narrower well) and orange (wider well). Green line is the Fermi energy. (b) Band diagram with wavefunctions of the bound states.	64
6.7	Band diagram of the newly designed double-quantum well structure forming a V-type quantum system and the wavefunctions of one ground state and two excited states.	65
6.8	Band edges as a function of lattice constant of various III-V compounds at room temperature, relative to Fermi level of gold Schottky contact (after Tiwari and Frank, 1992).	65

Chapter 1. Introduction

Coherent control is a quantum mechanical based method for controlling the evolution of an initial wavefunction toward a desired final wavefunction [1, 2, 3]. Among many possibilities the target wavefunction is selected and, by applying shaped laser pulses, the evolution is controlled to the desired direction. Coherent control is started and used in Chemistry to generate selectivity of chemical reaction processes by light such as optimizing the branching ratios of photo-dissociation reaction channels. In the middle of 1980s, coherent control was proposed by D. J. Tannor and S. A. Rice in *Journal of Chemical Physics* with the title of “Control of selectivity of chemical reaction via control of wave packet evolution” [3] and also by M. Shapiro and P. Brumer in *Journal of Chemical Physics* with the title of “Laser control of product quantum state populations in unimolecular reactions.” [4] Both showed that chemical reaction processes can be controlled by shaped laser pulses. After their remarkable proposal, coherent control has been demonstrated for manipulating both simple and complex systems such as atoms, molecules, and semiconductors [5, 6, 7, 8]. Moreover, the complete population transfer has been achieved in atomic systems based on the adiabatic passage, and the coherent control concept has been applied to the multi-photon excitation fluorescence microscopy toward a high degree of substance classification [9].

The early approaches in coherent control used narrowband pulsed lasers or continuous-wave lasers. Target reaction channels were controlled either by the laser frequency that corresponds to the resonant frequency or the vibration frequency of chemical bonds in a reaction process. However, this method was rather limited because the temporal characteristic of intrinsic interactions, such as natural decay or intramolecular vibrations, could be shorter than the laser pulse width. In 1982, the first femtosecond Ti:sapphire laser was constructed [10, 11]. Consequently, the study of ultrafast dynamics of quantum systems in a shorter time scale than a few picoseconds of intrinsic interaction time was achieved, which was followed by the coherent manipulation the systems [12]. Furthermore, The unprecedented high peak intensity of a femtosecond laser pulse has enabled the study of nonlinear light-matter interactions in the strong-field interaction regime.

In chemical reactions involved in molecules, biological and semiconductor materials, obtaining an analytical coherent control solution is nearly impossible, because either the Hamiltonian is insufficiently known or the processes are too complicated to approach analytically. Therefore, coherent control researches have been focused on, so called, “adaptive closed-loop control” [13]. The results of adaptive control provided, however, only limited information about the system, leaving the system as a “black-box”. On the other hand, analytic control approach has been successful with a simple quantum system like atoms [14, 15, 16, 17], in which the transition probability in a multi-photon process, for example, has been found sensitively changing to the detailed shape of an interacting laser pulse. It is noted that the early studies on the transition probability control have been mostly restricted to the transitions initiated from the ground state: for example, resonant-(three-level ladder systems) [14] and nonresonant (two-level systems) two-photon absorption processes [17]. In these cases, the transition probability can be easily measured by detecting the fluorescence signal decayed from the excited states. However, in a V -type system, which is the subject of this thesis, the transition from one of the excited states to the other, or the inter-excited states transition, is not simple to measure, thus difficult to control. It is because the final population of the target state comprises transferred electrons not only from the initial excited state

but also from the ground state. This difficulty can be resolved with a special detecting scheme, known as two-dimensional Fourier transform optical spectroscopy (2D-FTOS) [18, 19, 20]. 2D-FTOS is an optical extension of the 2D NMR [21], a recently developed spectroscopic tool for probing femtosecond electronic and vibrational dynamics and can be applied to molecules as large as small proteins. The femtosecond time resolution achieved in 2D-FTOS is crucial in understanding reaction dynamics and energy transfer processes [22]. In 2D-FTOS, a sequence of three ultrashort laser pulses interacts with a quantum system, and the fluorescence signal, $S(\tau_1, \tau_2)$, is detected as a function of two inter-pulse delays τ_1 and τ_2 . Fourier transformed signal, represented as a 2D complex-valued 2D spectral function, $S(\omega_1, \omega_2)$, reveals the linear and nonlinear response of the quantum system, where ω_1 and ω_2 are the conjugate Fourier frequencies of τ_1 and τ_2 . Especially, the off-diagonal peaks of $S(\omega_1, \omega_2)$ directly map the inter-excited state coupling of great interest.

However, another great merit of 2D-FTOS is not used yet, that is coherent control pulse shaping technique. By spectrally programming the broadband spectral components of a femtosecond laser pulse, the combination of coherent control technique and 2D-FTOS is realized resulting a more powerful tool, that is 2D Fourier transform coherent control spectroscopy (2D-FTCCS). In this thesis, using this newly developed 2D-FTCCS, the preparation of a quantum systems, and an annihilation or enhancement of specific couplings, and the detection of the quantum state and coupling coefficients are described. We experimentally demonstrate the control of two-photon inter-excited state transition in a V -type system of atomic rubidium. Among the three optical pulses of 2D-FTOS, the first pulse was synthesized to selectively initiate the quantum system in a simple quantum state. The second pulse is pulse-shaped in terms of linear chirp rate or spectral block phase function to control the inter-excited state transitions. Then, quantum control enhancement and annihilation of $5P_{1/2} \rightarrow 5P_{3/2}$ transition are tested, where the engineered transitions need to be distinguishably extracted in the presence of dominant one-photon transitions. In these simple coherent control experiments with a V -type system, the ability of advanced 2D-FTOS scheme harnessed with coherent control technique, 2D-FTCCS is demonstrated. Furthermore, we show the striking similarity between a two-photon inter-excited state transition in a V -type system and a one-photon transition in two-level systems results to coherent transient phenomena along with experimental demonstration in use of 2D-FTCCS.

In this thesis, we demonstrate a combined technique of coherent control and 2D-FTOS in a quantum mechanical model system. We expect that this newly developed combined technique can be applied to various fields of research. As an application, this 2D-FTCCS technique will be useful to probe time-dependent coupling paths among multi-level electronic energy states in complex quantum systems. Also, we envision that this technique further combined with semiconductor nano fabrication may be a possible candidate for quantum computing. For example, a suitably designed multi-level system can be controlled by shaped laser pulses to perform quantum computing so that the resulting quantum wavefunction are measured with 2D-FTCCS.

This thesis contains 7 chapters. In Chapter 2, we review the two typical coherent control approaches: the adaptive control scheme and the analytic control scheme. Then, we discuss the pulse-shaping technique which provides crucial ability in coherent control. Next, we discuss the three pulse coherent control scheme, or 2D-FTOS, in Chapter 3. For a theoretical description of 2D-FTOS, the transition probability amplitudes in a V -type system are thoroughly derived. In Chapter 4, we demonstrate the combination of these two powerful techniques, the coherent control of pulse shaping and 2D-FTOS. For this, three ultrashort laser pulses are individually shaped to prepare and control the quantum interference involved in the two-photon inter-excited state transitions of a V -type quantum system. Then, an annihilation

and enhancement of the inter-excited states couplings are verified. In Chapter 5, we show that the two-photon coherent control in a V -type three level system is projected to a one-photon coherent transient in a simpler two-level system. In this experiment, it is shown that the roles of time and linear chirp in the latter are duplicated by linear and quadratic chirp rates in the former. For an experimental demonstration, we use 2D-FTCCS, to retrieve the phase and amplitude of the controlled transition probability. In Chapter 6, we propose a new coherent control experiment with a semiconductor material to further demonstrate the advanced ability of the 2D-Fourier transform coherent control spectroscopy. Finally, Chapter 7 concludes the thesis.



Chapter 2. Review of coherent control

Quantum control, or coherent control, is an active operation in a system's evolution to maximize the probability toward a desirable target state (see Fig. 2.1). The controlled evolution can be a chemical reaction pathway, a direction of electronic dynamics in semiconductors, light absorption process, or large transition probability in atomic systems. The quantum systems which may be the object of coherent control can be single atoms, molecules, and collective modes of solid-state matters such as excitons and phonons. Also, finding out how to coherently control the evolution of a system provides a refined means to understand the system itself.

Femtosecond laser pulse shaping provides a synthesized broadband coherent spectrum in optical frequency and has become one of the most useful tools for coherent control. Laser spectrum can be programmed to match the multiple resonant frequencies of the electronic and vibrational transitions of a quantum system. The shaped pulses can be simply either a shortened or stretched optical pulse in time domain, or can be of an arbitrarily complex temporal shape. The optical waveform synthesis has been rapidly developed for diverse applications such as ultra high speed optical networks, chemical reaction triggering, and biological process monitoring, etc.

After the proposal of coherent control soon followed by its experimental demonstration, a significant volume of research has been performed to develop the ability of quantum control both in a variety of quantum systems. In some simple systems, analytic solutions have been obtained directly from the interaction Hamiltonian between the quantum system and laser field. However, in a relative complex system such as molecules, biological or semiconductor materials, obtaining an analytical solution has turned out to be nearly impossible. The reason is either that the Hamiltonian is insufficiently known or that the control interaction is too complicated to trace analytically.

Instead, adaptive coherent control which tests various electric field shapes positively fed by experimental feedback has been successful in many problems. As a practical application of the coherent control, the optimization problem in many photo-induced processes, for example, determination of a photo-chemical reaction channel, the adaptive coherent control has been developed [13, 23, 24, 25, 26].

On the other hand, for a simple system like alkali atoms, analytic control approach can be more effective. The system can be easily controlled by a predetermined electric field, which is analytically designed by solving the Hamiltonian problem of the given light-matter interaction [14, 15, 16, 17, 27, 28]. The analytic approach can be accessed based on two kind of analysis: in frequency domain analysis and in time domain analysis. The time domain analysis uses the time evolution of the quantum system by directly solving the time-dependent Schrodinger equation. The evolution of the system can be alternatively controlled in frequency domain by programming the quantum interference between the several passages that lead to the target wavefunction.

In Sec. 2.1, we study two basic pulse-shaping methods: the frequency domain pulse shaping with a spatial light modulator in Sec. 2.1.1, and the time domain pulse shaping with an acousto-optic modulator in Sec. 2.1.2. In Sec. 2.2, the adaptive approach on coherent control is briefly introduced. Also in Sec. 2.3, the analytic control scheme both in frequency domain (Sec.2.3.1) and in time domain (Sec.2.3.2) will be discussed.

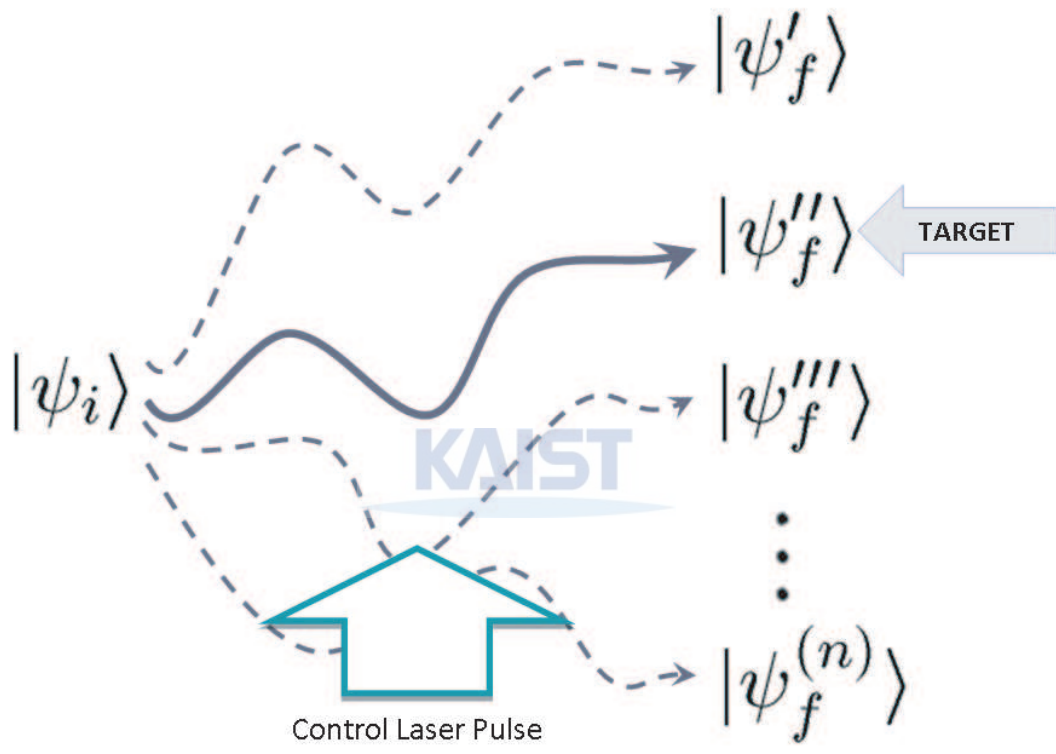


Figure 2.1: Quantum coherent control influencing the evolution of a wavefunction. The system's initial wavefunction ψ_i evolves to a coherent superposition of the all possible final states $\psi_f^{(n)}$ under the influence of the control-free Hamiltonian H_o . On the other hand, with an externally controlled term added to the Hamiltonian, for example, the interaction with a control laser pulse (electric field) in our case, the wavefunction evolution is directed along the desired direction to the target state.

2.1 Femtosecond pulse shaping

In 1981, the invention of the colliding pulse mode-locked ring dye laser enabled one to make ultrashort laser pulses below 100 fs in time duration [29]. After the subsequent nonlinear pulse compression, the even shorter pulses as short as 6 fs has been produced [30]. The femtosecond Ti:Sapphire laser has been developed in early 1990s providing a number of important advantages compared to the dye lasers: output power and stability have been considerably improved and also the laser has become a convenient turn-key system. Nowadays, a Ti:Sapphire oscillator can produce extremely short pulses below 6 fs directly from the laser without a pulse compression.

Using the Ti:sapphire short pulse lasers, optical waveform synthesis methods, or pulse shaping techniques, have been developed over the last decades. The programmed light forms have been used for ultrafast spectroscopy as well as quantum coherent control. A number of approaches for ultrafast pulse shaping have been demonstrated, but they can be grouped in the following two methods: one is, to be discussed in Sec.2.1.1, the frequency domain pulse shaping with a spatial light modulator which operates on a spatially dispersed optical frequency spectrum, and the other is the time domain pulse shaping with an acousto-optic modulator, to be described in Sec. 2.1.2.

2.1.1 Spatial light modulator

The pulse shaping apparatus in frequency domain is shown in Fig. 2.2, which was first reported by Froehly [31]. The overall pulse shaping is performed in a 4f geometry that comprises two lenses and two gratings. To achieve an exact pulse shape as programmed, the gratings and the lenses must be aligned to make a "zero dispersion pulse compressor". Simply, the output pulse should be identical to the input pulse when the spatial light modulator (SLM) is removed. However, the thickness of the lenses and their aberration, as well as the unwanted spectral deformation by the gratings, hinder the perfect operation of the pulse shaper. The perfect "zero dispersion pulse compressor" can be checked by the distortion-free propagation of the output pulse [33, 34] or an absence of spatial chirps. If the output pulse is free of any spatial chirp, the beam profile is smoothly wiped out uniformly, instead of being partially deformed, when a part of the spectrum is blocked from one side to the other in the Fourier plane of the pulse shaper.

The femtosecond pulse shaping in frequency domain is achieved in an intuitive way. First we consider the input pulse as a Fourier-transform limited (FTL) pulse, i.e., the shortest pulse in time domain, or the spectral components of the pulse are all in phase. The first step of the pulse shaping is that the individual frequency components contained within the input pulse to be dispersed spatially by a grating, as shown in Fig. 2.2. And then, the spreading envelope is collimated by a lens located at a distance of its focal length from the grating, and, in the meantime, individual spectral components are focused to small diffraction limited spots. Basically, the first lens operates as a Fourier transformer which converts the angular dispersion from the first grating to a spatial separation at the focal plane of itself. Then, spectral components pass through a programmed mask or SLM which controls amplitudes and delays, or phases, of each spectral components. The second lens performs the inverse procedure of the first lens and the second grating recombines all the spectral components to a collimated beam. As a result, the output pulse in time domain is the Fourier transform of the sum of the spectral components of which the amplitudes and phases are programmed by the SLM.

Liquid crystal SLM uses an array of nematic liquid crystals, which are made out of rod-like molecules aligned with their long axes in the absence of an external electric field, or voltage. When voltage is applied

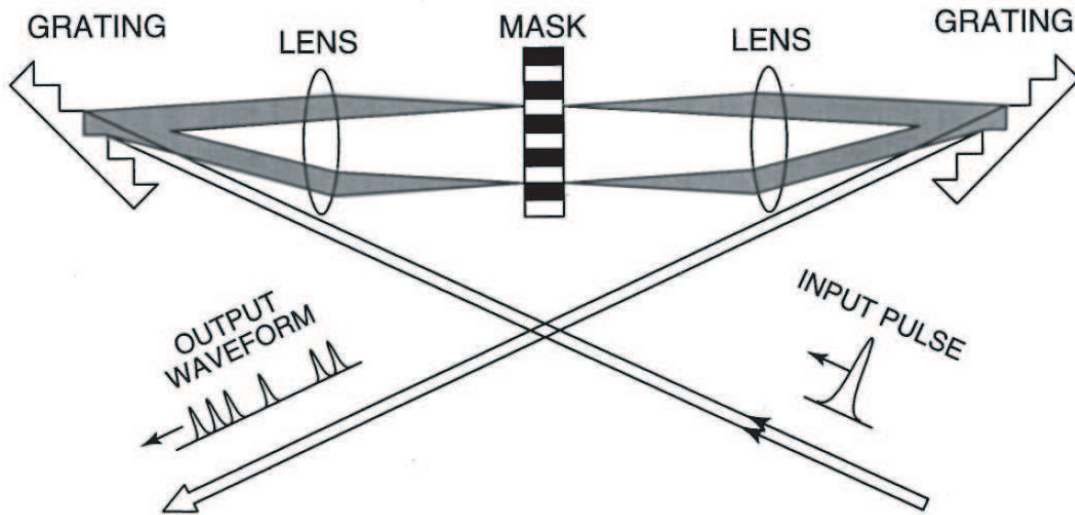


Figure 2.2: Schematic of femtosecond pulse shaping in frequency domain with spatial light modulator. Gratings and lenses are arranged in a 4f configuration. The pulse shaping procedure is described in the text. [32]

to them in the perpendicular direction relative to their long axes, the liquid crystal molecules tilt along the voltage direction and the refractive index changes for a light polarized along their long axes. Therefore, individual phases of spectral components can be controlled by the strength of the voltages applied to the corresponding liquid crystal cells. The controllable number of spectral components is limited by the pixel number of the liquid crystals, and the spectral resolution is related to the diffraction limit of the lens used in the 4f geometry.

2.1.2 Acousto-optic pulse shaper

Acousto-optics effect deals with the interaction between an optical wave and an acoustic wave in a material medium, especially the diffraction of laser light by ultrasound or sound in general. The first prediction of this interaction was achieved by Brillouin in 1922 [35] and was experimentally verified in 1932 by Debye and Sears [36] and also by Lucas and Biguard [37]. The most interesting phenomenon in acousto-optics is the diffraction of light by the acoustically perturbed medium. Acousto-optic effects are based on the change of the index of refraction of the medium by the acoustic wave. In a medium through which an acoustic wave propagates, strain field or pressure fluctuation is produced. As a periodic function of the position of the acoustic wave, a change in the index of refraction, known as the photoelastic effect occurs. Then, due to the periodic change in the index of refraction, a propagating optical wave is diverted via Bragg diffraction. The acousto-optic effect is extensively used in ultrasonic wave measurements, nondestructive testing, structural health monitoring, and biomedical applications. Also, a number of acousto-optic effect based devices such as acousto-optic modulators, filters and deflectors are developed and actively in use.

The acousto-optic programmable dispersive filter (AOPDF) which can be used in femtosecond pulse shaping [39] is based on a quasi collinear acousto-optic interaction [40]. The phase of individual frequency component of an optical wave is controlled by the corresponding acoustic frequency component which is varied as a function of time. Also, the amplitude of the optical frequency component can be tuned by the intensity of the acoustic wave launched in the AOPDF medium. AOPDF performs a good shaping

resolution without precise alignment procedure.

Figure 2.3 (a) shows the schematic of AOPDF. A piezoelectric transducer excites a programmed temporal signal into the acousto-optic medium, and the acoustic wave propagates along the z -axis with a velocity V . The acoustic wave, induced by the temporal shape of the transducer signal, builds pressure fluctuation spatially in the medium as a periodic function of position z . If we consider a monochromatic optical wave of frequency ω which is incident in fast ordinary axis to the medium, then, two optical modes, mode 1 in fast ordinary axis and mode 2 in slow extraordinary axis, can be coupled by acousto-optic interaction as shown in Fig. 2.3 (b), as long as the condition of phase matching is satisfied, i.e.,

$$\omega_2 = \omega_1 + \Omega \quad (2.1)$$

$$k_2 = k_1 + K, \quad (2.2)$$

where ω_2 and ω_1 are the frequency of the optical fields in mode 2 and mode 1, respectively, and Ω the acoustic frequency. Also k_2 and k_1 are the wavevector of the optical fields in mode 2 and mode 1, and K the acoustic wavevector. Then, the incident optical energy is transferred to the diffracted optical wave, when the phase matching conditions are satisfied, given by

$$E_2(\omega_2) \exp [i(\omega_2 t - k_2 z)] = E_1(\omega_1) \exp [i(\omega_1 t - k_1 z)] * S(\Omega) \exp [i(\Omega t - Kz)], \quad (2.3)$$

where E_2 is the diffracted optical field, E_1 the incident optical field, and S the acoustic signal. Therefore, the optical frequency is diffracted at a position z where the spatial frequency is induced by the acoustic wave at $z(\omega)$. The incident optical wave initially in mode 1 travels a distance before it faces to $z(\omega)$, and at $z(\omega)$, some amount of energy of the optical wave is diffracted to mode 2 and the amount is relative to the intensity of the acoustic signal. The travel time inside the medium is caused by the refraction index difference between mode 1 and mode 2 times the position $z(\omega)$, i.e., $\Delta t = \Delta n z(\omega)$. Likewise, if the input optical wave is a femtosecond pulse with a broadband spectrum, instead of a monochromatic wave, the spectral components diffracted to mode 2 by acoustic wave can be controlled both in amplitude and in phase by the acoustic power and the position of $z(\omega)$, respectively. The relation between the output optical pulse and the input optical pulse can be expressed with the acoustic signal as [39]

$$E_2(t) \propto E_1(t) \otimes S(t/\alpha), \quad (2.4)$$

where \otimes means convolution and the scaling factor $\alpha = \Delta n(V/c)$ is the ratio of the speed of sound to the speed of light times the index difference between the ordinary and the extraordinary waves. Also, α means the ratio of the acoustic frequency Ω to the optical frequency ω , $\alpha = \Omega/\omega$, and Eq. (2.4) can be written in the frequency domain as

$$E_2(\omega) \propto E_1(\omega) S(\alpha\omega). \quad (2.5)$$

Therefore, by generating a proper function $S(t)$, one can achieve any desired waveform. Although the above explanation is given for the case of a collinear interaction scheme, but the same formulation holds for a quasi-collinear case which has been used in our experiments [40].

The nonlinear crystal we have used in our experiment is the TeO_2 crystal of $d = 2.5\text{cm}$ length. In our case, the index difference of TeO_2 crystal between the ordinary and extraordinary polarization axes for the given propagation direction is $\Delta n = 0.04$. Therefore, the maximally achievable group delay is $\Delta T = \Delta n \cdot d/c = 3.33$ ps. The speed of sound V of TeO_2 in the z direction is 1000 m/s, and the matched acoustical frequency is $f = \Delta n \frac{V}{c} \omega_0 = 52.5$ MHz, where ω_0 is laser center frequency, 375 THz at 800 nm. The bandwidth of the transducer is about 20 MHz at 52.5 MHz, which corresponds to an optical bandwidth of 150 THz at 375 THz. Then, the associated temporal resolution is about 6.7 fs.

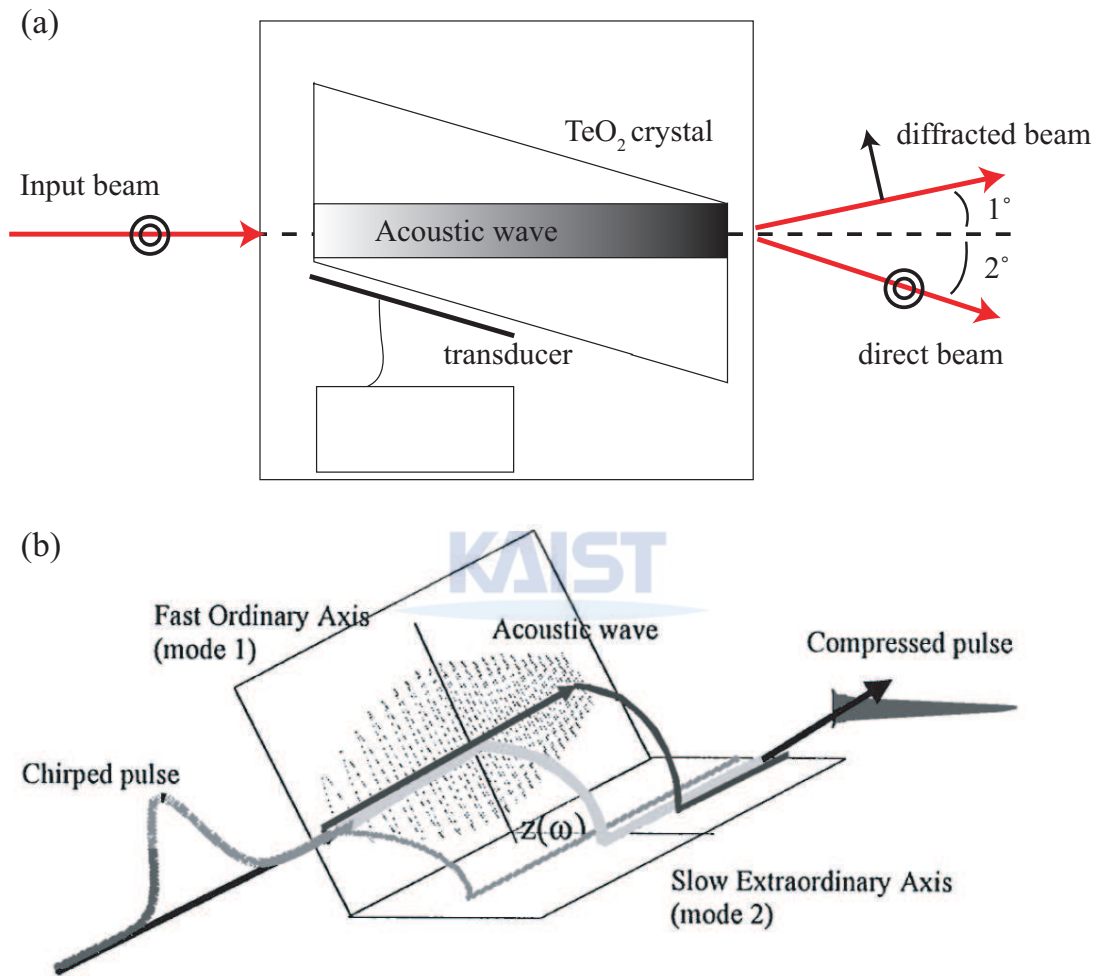


Figure 2.3: (a) AOPDF top view. The output beam is diffracted by 1 degree from the input beam, in the 90-degree-rotated linear polarization. (b) Schematic of AOPDF. Mode 1 in fast ordinary axis and mode 2 in slow extraordinary axis, are coupled by acousto-optic interaction when the phase matching condition is satisfied. [38]

Amplitude shaping $A(\omega) = f(\omega) * g(\omega)$	Phase shaping $\Phi(\omega) = h(\omega)$
$\lambda_0 = \mathbf{position}, \omega_0 = 2\pi c/\lambda_0$ $\delta\lambda_0 = \mathbf{width}, x_0 = \delta\lambda_0/(2\lambda_0)$ $\delta\omega_0 = \omega_0(x_0 - x_0^3)$ $f(\omega) = \exp\left(-\left(\frac{\omega - \omega_0}{\delta\omega_0}\right)^6\right)$	$a_1 = \mathit{delay}, \quad a_2 = \mathit{second\ order}$ $a_3 = \mathit{third\ order}, a_4 = \mathit{fourth\ order}$ $h(\omega) = -(a_1 * (\omega - \omega_0) + a_2 * \frac{(\omega - \omega_0)^2}{2} + a_3 * \frac{(\omega - \omega_0)^3}{6} + a_4 * \frac{(\omega - \omega_0)^4}{24})$
$\lambda_1 = \mathbf{hole\ position}, \omega_1 = 2\pi c/\lambda_1$ $\delta\lambda_1 = \mathbf{hole\ width}, x_1 = \delta\lambda_1/(2\lambda_1)$ $\delta\omega_1 = \omega_1(x_1 - x_1^3)/2$ $k = \mathbf{hole\ depth}$ $g(\omega) = 1 - k * \exp\left(-\left(\frac{\omega - \omega_1}{\delta\omega_1}\right)^2\right)$	Total Spectral shaping function $S(\omega) = A(\omega) * \exp(i\Phi(\omega))$ Three pulse generation $E_{out}(\omega) = (S_1(\omega) + S_2(\omega) + S_3(\omega))E_{in}(\omega)$

Figure 2.4: Synthesis of the pulse shaping function parameters of the acoustic wave. Acoustic wave parameters are categorized into amplitude shaping and phase shaping parts. The frequency domain acoustic wave is Fourier transformed to the time domain signal and applied to the acousto-optic medium via a transducer.

Figure 2.4 shows the categorized pulse shaping parameters of the acoustic wave. The actual acoustic wave signal applied to acousto-optic medium is given by

$$S(\Omega) = A(\Omega) * \exp(i\Phi(\Omega)), \quad (2.6)$$

where Ω is the calibrated acoustic wave frequency, $\Omega = \alpha\omega$. The parameters are divided into two groups, the amplitude shaping $A(\Omega)$ and the phase shaping $\Phi(\Omega)$. Also, the three pulses can be generated by summation of three acoustic waves, $S(\Omega) = S_1 + S_2 + S_3$, where S_1 , S_2 , and S_3 refer to the first, second, and third pulses with different values of the time delay, a_1 's.

2.2 Adaptive coherent control

In this section, we discuss about the adaptive quantum control scheme using a closed-loop learning algorithm [23]. For a complex system, the adaptive control has proven to find the nearly best control solution toward the desired direction, even without knowing a priori information of the Hamiltonian of the systems. The control parameters are optimized iteratively using the feedback signal of the reaction of the system. This approach might be regarded as a "active observation" rather than simple, passive observation by controlling the dynamical evolution of the wavefunctions of the system, and has been applied to a number of systems [13, 23, 24, 25, 26, 41, 42, 43].

Figure 2.5 shows an experimental setup of adaptive femtosecond coherent control. A femtosecond pulse shaper, a SLM for this case, generates a phase and amplitude profile of a pulse. After the programmed pulse interacts with the target system, the reaction of the system is given to a learning

algorithm as a feedback signal. Then, the pulse profile is re-prepared as a result of the feedback. And this sequence is iteratively performed to find the optimum pulse for the purpose. Because a brute-force full scan of the the complete control parameter space is an enormous time consuming process, the learning algorithm helps to reduce the scanning time significantly with directional change of parameters. The optimum pulse found in the iterative process may not be the ultimately optimal, but often an acceptable best solution in a local optimum.

Figure 2.6 shows (a) the drawing of the MLCT chromophore $[Ru(dpb)_3]^{2+}$, (b) the absorption and emission spectra of $[Ru(dpb)_3](PF_6)_2$ [44], and (c) the schematic of the energy level structure of $[Ru(dpb)_3](PF_6)_2$, where MLCT refers metal-to-ligand charge-transfer. Gerber and his co-workers performed adaptive coherent control on this system only by changing the phases of a femtosecond pulse with a 128-pixel SLM. The fluorescence from 3MLCT state given at 620 nm, shown in Fig. 2.6(c), was used as feedback signals which was proportional to the population of 1MLCT band. 1MLCT band of $[Ru(dpb)_3]^{2+}$ molecule could not be excited from a single 800 nm photon but, could be from two-photon excitation process. The central issue of this study was that, in this two-photon transition process, the excitation probability could be enhanced beyond the intensity maximum pulse, or a FTL pulse, and could be depressed while increasing the intensity by changing the individual phases of the pulse. Note that, the intensity of the pulse dominated the excitation in multi-photon transition process in most cases. To test this, the phase-shaped laser pulses were applied to the $[Ru(dpb)_3](PF_6)_2$ sample and the fluorescence was measured at 620nm. Also, the second-harmonic generation (SHG) intensity was measured as an intensity reference signal.

Figure 2.7 shows the experimental excitation results for the two optimization goals; maximization (solid circles) and minimization (open circles) of the ratio between the emission and SHG. From these data, it is clear that the most intense pulse does not satisfy the condition for optimal excitation, but specific pulse shapes are more adequate for the two-photon excitation of the molecular systems.

2.3 Analytic coherent control

Now, we will study about previous researches on quantum control of transition probability in atomic systems based on analytic analysis. Analytic approach of quantum control can be mainly classified to the frequency domain approach proposed by Brumer and Shapiro and the time domain approach proposed by Rice and Tannor.

In this chapter, we focus on the resonant two photon absorption case studied by Silberberg *et al.* for the frequency domain approach [14] in Sec. 2.3.1, and the coherent transient phenomena studied by Girard *et al.* for the time domain approach [46] in Sec. 2.3.2.

2.3.1 Resonant two-photon transition

In this section, we will consider a resonant two-photon absorption in an atomic system, which is sensitively changed with the shape of femtosecond pulses in weak-field regime. It was known that, in nonresonant two-photon (or multi-photon) transition cases, the Fourier-transform limited (FTL) pulse, which has the strongest peak intensity, is the most efficient pulse in weak-field regime [27]. However, in resonant two-photon transition case, this assumption does not hold and transition efficiency above the limit of FTL pulse is achievable.

In a ladder system, which comprises a ground state $|g\rangle$, an intermediate state $|n\rangle$, and an excited

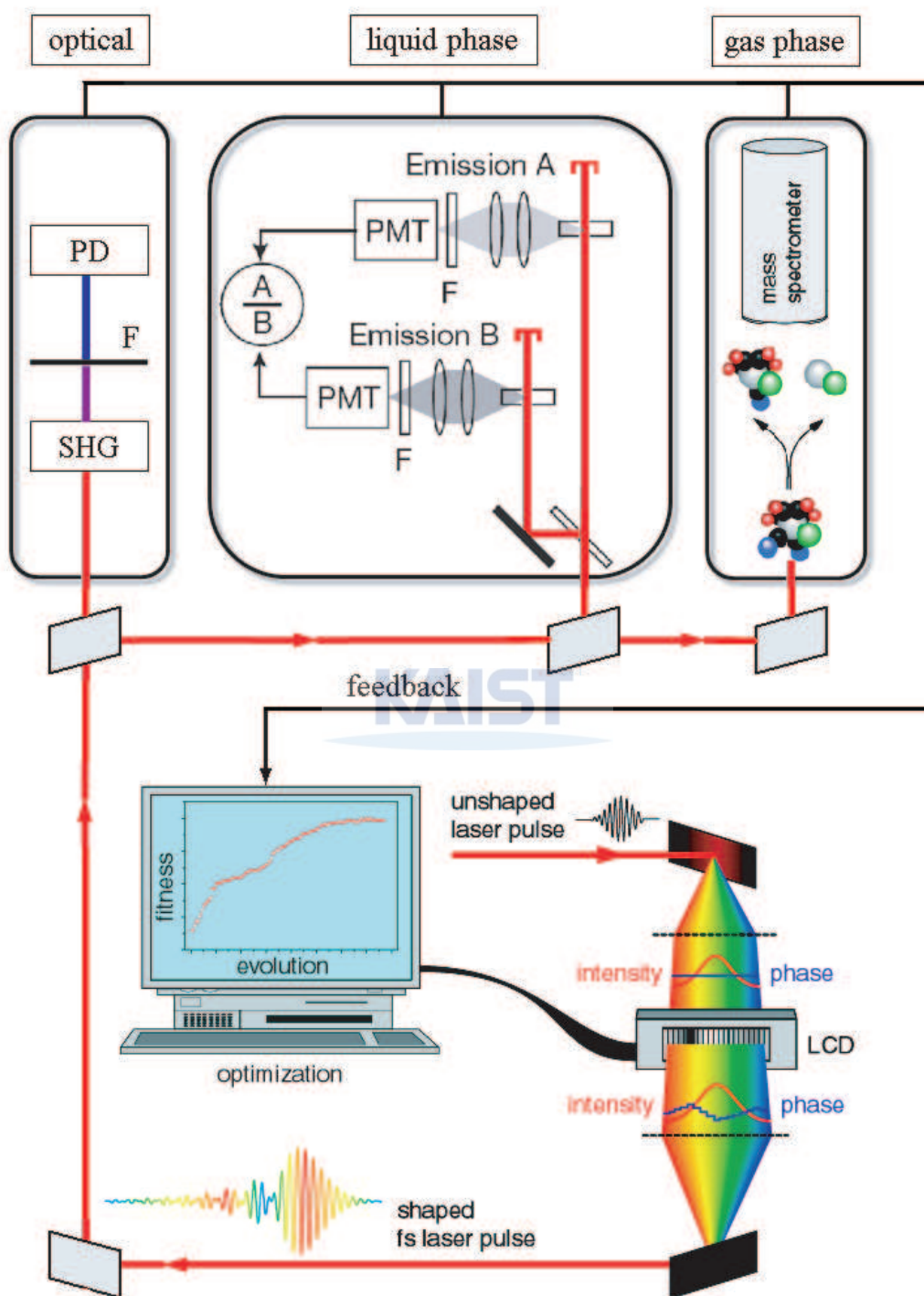


Figure 2.5: Experimental setup of adaptive coherent control. A SLM or femtosecond pulse shaper is used to shape the pulse with a help of feedback signal and closed-loop learning algorithm. The learning algorithm iteratively finds optimum pulses for different types of experiments.

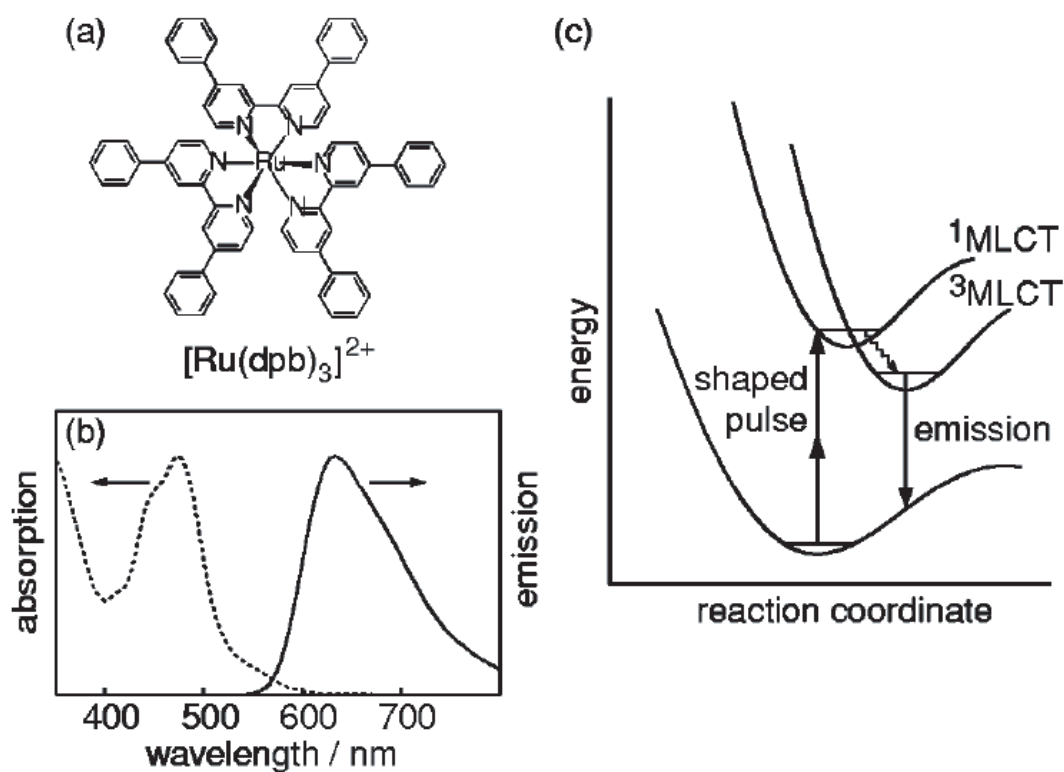


Figure 2.6: (a) Drawing of the MLCT chromophore $[Ru(dpb)_3]^{2+}$. (b) Normalized absorption (dashed line) and emission spectra (solid line) collected for the molecule dissolved in methanol at 298 K. (c) The schematic of the control methodology where multiphoton absorption of a shaped 800 nm laser pulse excites the 1MLCT band, and emission from the lower energy 3MLCT state accessed via nonradiative relaxation is used as a feedback signal. [43]

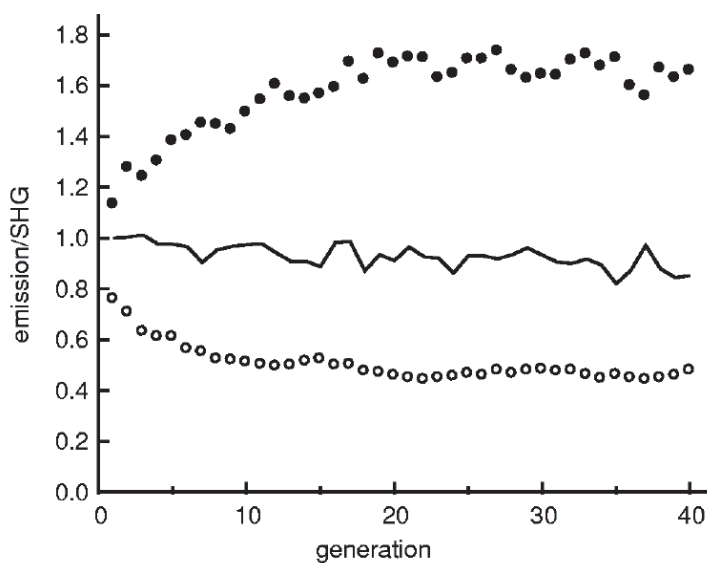


Figure 2.7: Experimental results of adaptive control on $[Ru(dpb)_3](PF_6)_2$. Solid circles are for maximization and open circles are for minimization of the ratio excitation/SHG. [43]

state $|f\rangle$, as shown in Fig. 2.8 for rubidium atom, the transition probability amplitude from $|g\rangle$ to $|f\rangle$ via $|n\rangle$ can be obtained from the second order time dependent perturbation theory as

$$a_f(t) = -\frac{1}{\hbar^2} \sum \mu_{fn} \mu_{ng} \int_{-\infty}^t \int_{-\infty}^{t_1} E(t_1) E(t_2) \exp(i\omega_{fn}t_1) \exp(i\omega_{ng}t_2) dt_2 dt_1, \quad (2.7)$$

where μ_{fn} and μ_{ng} are the dipole moment matrix elements, ω_{ij} the resonance frequencies, $\omega_{ij} \equiv (E_i - E_j)/\hbar$. In a resonant ladder system, i.e., an intermediate state $|n\rangle$ is within the spectral range of the femtosecond pulse, and $\omega_{ng}, \omega_{fn} > 0$, Eq. (2.7) can be approximated to the following form given by

$$c_{ni}^{(2)} = i \frac{\mu_{fi} \mu_{ig}}{\hbar^2} \left[i\pi E(\omega_{ig}) E(\omega_{fi}) + \wp \int d\omega \frac{E(\omega) E(\omega_{fg} - \omega)}{\omega_{ig} - \omega} \right], \quad (2.8)$$

where $|i\rangle$ is the resonant intermediate state, \wp is the principal value of Cauchy, and $\omega_{ig}, \omega_{fg} - \omega_{ig} = \omega_{fi}$ are the resonance frequencies of the transitions. Equation (2.8) shows different behavior from the nonresonant case in [27]. Equation (2.8) can be distinguished into two parts: the first term relevant to resonant part depends only on the spectral components of the pulse at the resonance frequencies, and the second term of nonresonant part integrates over the contributions of all other spectral components of the pulse. In the case of the FTL pulse, the nonresonant part destructively interferes around at the point ω_{ig} since the integration excesses over both negative and positive contributions. Therefore, a transform-limited pulse is not optimal pulse of two-photon transition for the resonant case. Simply, blocking all red (or blue) detuned spectral components around ω_{ig} can enhance the transition. Also, a larger enhancement can be achieved by applying a phase step function $\pi/2$ at ω_{ig} making constructive interference that inverts the sign of $E(\omega)E(\omega_{fg} - \omega)$ about that point.

To demonstrate the enhancement of the first guess, Silberberg and co-workers placed an adjustable slit at the Fourier plane of 4f configuration, which was described in Sec. 2.1.1, to block spectral components symmetrically around $\omega_{fg}/2$ as shown in Fig. 2.9(a). Fluorescence signal was measured as a function of "cutoff wavelengths". $\omega_{fg}/2$ is the two-photon resonance frequency as well as center frequency of the laser. The experimental and calculation results are shown in Fig. 2.9(b). As expected, the maximum enhancement was achieved when the cutoff frequency is approached, from long wavelength to short wavelength, to the one-photon resonant frequency ω_{ig} , reaching a factor of 2, while the power of the pulse at that point was reduced by 71%. As the blocking slit passing by the position corresponds to ω_{ig} , the fluorescence signal drops rapidly because the pulse through the slit becomes small and completely disappears at 778 nm, $\omega_{fg}/2$. At the point where slit approaches at ω_{ig} position, the calculated temporal profile is illustrated in Fig. 2.9(c) with a comparison with a FTL pulse. The values are normalized to the peak intensity of the FTL pulse. The peak intensity of blocked pulse was reduced a factor of 38 but, the two-photon transition was doubled.

2.3.2 Coherent transients

Coherent transient (CT) phenomena refers that the population fluctuation of an excited state during the interaction of a system with a highly linear chirped femtosecond pulse. It was directly shown experimentally for the first time by Girard *et al.* [45] and studied extensively [46, 47, 48]. Coherent transient occurs due to the interference between resonant and nonresonant excitation.

In weak field regime, the transition probability amplitude between the ground state $|g\rangle$ and the excited state $|e\rangle$ can be calculated using the Schrodinger equation within the first order perturbation

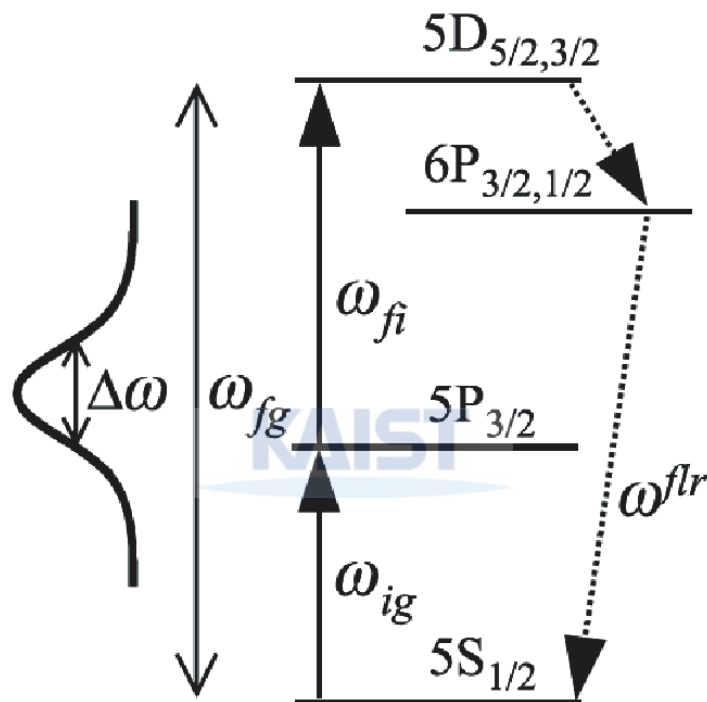


Figure 2.8: Energy level diagram of a resonant TPA in Rb. The frequencies of the 5S-5P (ω_{ig}) and 5P-5D (ω_{fi}) resonant transitions correspond to 780.2 nm and 776.0 nm, respectively. The pulse spectrum is centered on the two-photon transition frequency ($\omega_{fg}/2$) at 778.1 nm, with a bandwidth of $\Delta\omega = 18\text{nm}$ (FWHM). The excited atoms spontaneously decay to the ground level through the 6P, emitting a fluorescence signal at ω^{flr} ($\approx 420\text{ nm}$) [14].

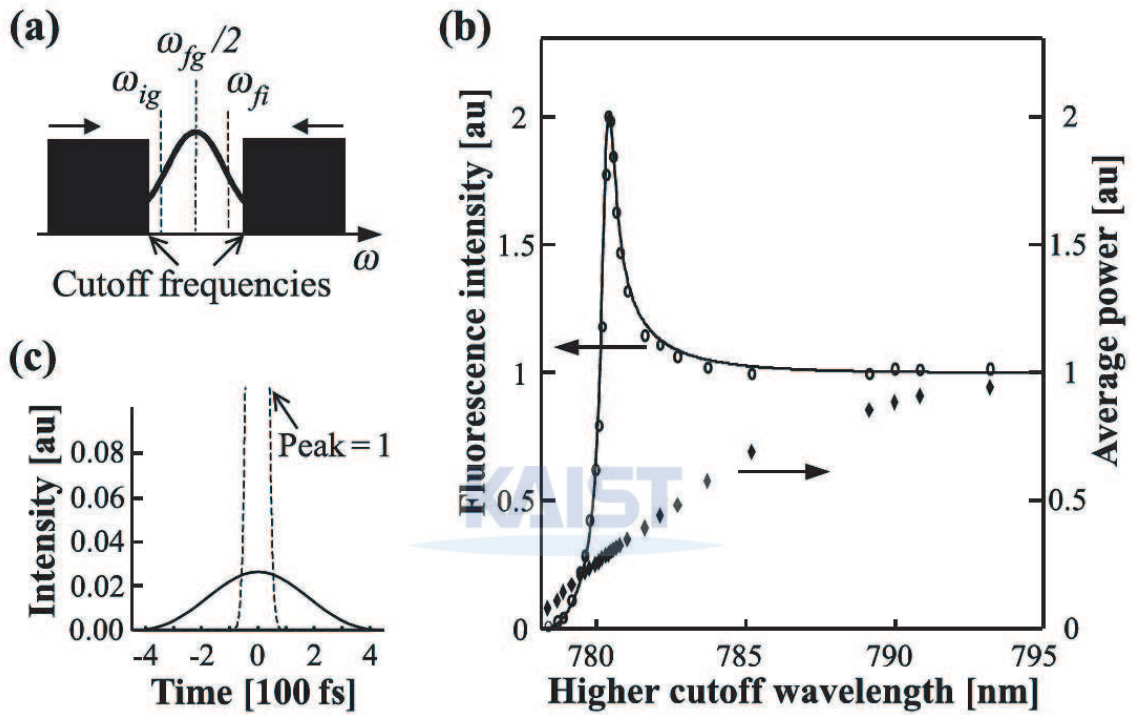


Figure 2.9: Experimental and calculated results performed on resonant two-photon transition in Rb atom. (a) Schematic expression of tested scheme: spectral components of the pulse was blocked symmetrically around $\omega_{fg}/2$ by an adjustable slit. (b) The transmitted power of the pulse (diamonds) and the experimental results of detected fluorescence (circles) and calculated transition (line). The two-photon transition doubled when the cutoff wavelengths approached the resonant transition wavelengths. (c) Calculated temporal intensities of the optimal shaped pulse (solid curve) and the transform-limited pulse (dashed lines), normalized to peak intensity of the transform-limited pulse. . [14]

theory written as

$$c_{eg}(t) \propto \int_{-\infty}^t \exp\left(-\frac{2\ln 2 t'^2}{\tau_c^2}\right) \exp\left(-i\frac{(t' - t_o)^2 - t_o^2}{2\phi''}\right), \quad (2.9)$$

where τ_c is the pulse width of the chirped pulse, ϕ'' the linear chirp coefficient, and $t_o = (\omega_{eg} - \omega)\phi''$ the time when the laser sweeping frequency goes through the atomic resonance [45]. Also, the above equation can be derived to frequency domain calculation given as [47, 46]

$$c_e(t) = \frac{\mu_{eg}}{\hbar} \left[\frac{1}{2} A(\omega_{eg}) e^{i\phi(\omega_{eg})} + \frac{i}{2\pi} \wp \int_{-\infty}^{+\infty} d\omega \frac{A(\omega) e^{-i[(\omega - \omega_{eg})t - \phi(\omega)]}}{\omega - \omega_{eg}} \right], \quad (2.10)$$

where ω_{eg} is the transition frequency, μ_{eg} the dipole moment matrix element, $|g\rangle$ and $|e\rangle$ the ground and excited states, respectively, and $A(\omega)$ and $\phi(\omega)$ the amplitude and phase of the pump electric field spectrum. \wp is the principal Cauchy value. Here again, the first term is resonant part and the second term is nonresonant part. The CT phenomena can be observed clearly during the time remnant of the pulse after the resonant frequency component interacts. It is because of the interference between the excitation and the following nonresonant transitions, when the femtosecond pulse is heavily chirped.

Girard and his co-workers used atomic rubidium for this study as shown in Fig. 2.10. The $5S_{1/2} - 5P_{1/2}$ transition at 794.7 nm is resonantly excited with a chirped shaped pulse having bandwidth of ~ 8 nm. Note that, the resonance wavelength of the transition to $5P_{3/2}$ state at 780 nm is not included in the pulse spectrum. The excited state population during the interaction with the pulse is observed by the other highly detuned pulse at 607 nm exciting the $5P_{1/2}$ state to higher levels extends from $6D$ to $10S$.

Interesting part of this study is that, by slicing the section of the pulse in time domain corresponds to the first downward oscillation, the transition probability enhanced as shown in Fig. 2.11(a). When the pulse centered at 794.7 nm has linear chirp value of $\phi'' = -4.9 \times 10^5 \text{ fs}^2$, the first downward oscillation occurs at about 2 ps. Therefore, if we slice the pulse at the section during the first decreasing part of the CT, the final population can be enhanced. The slicing the pulse in time with the order of ~ 100 fs is achieved by calculating the pulse in frequency domain and pulse shaped accordingly. As expected, the experimental results show the same results with the calculation as shown in Fig. 2.11 (b). Note that, the hole-shaped pulse in time domain to enhance the transition has a bigger spectral amplitude at the resonance frequency ω_{eg} .

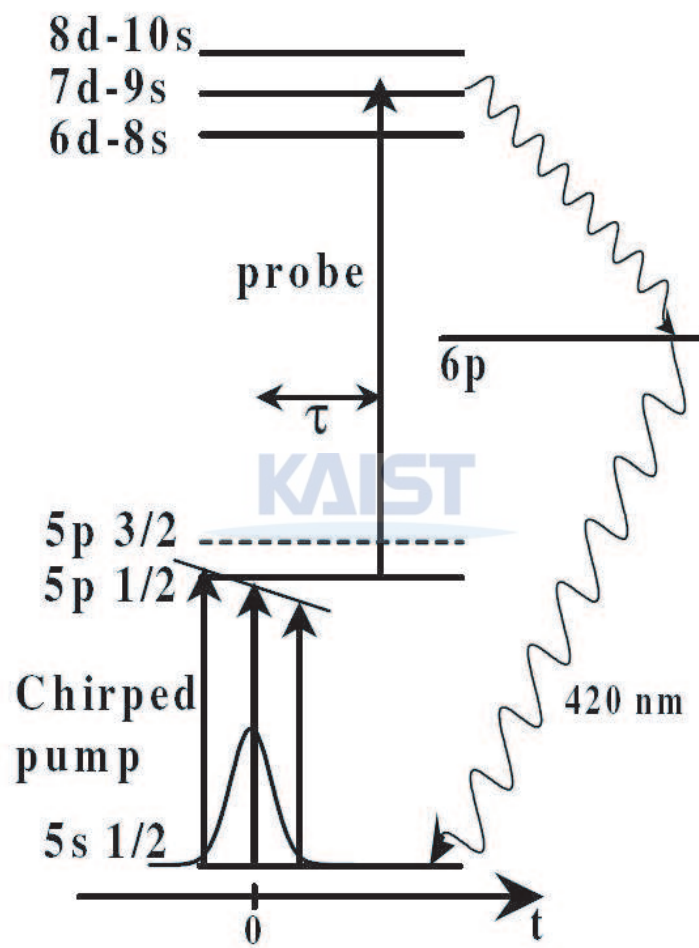


Figure 2.10: Excitation scheme of rubidium. τ is the pump-probe delay. [46]

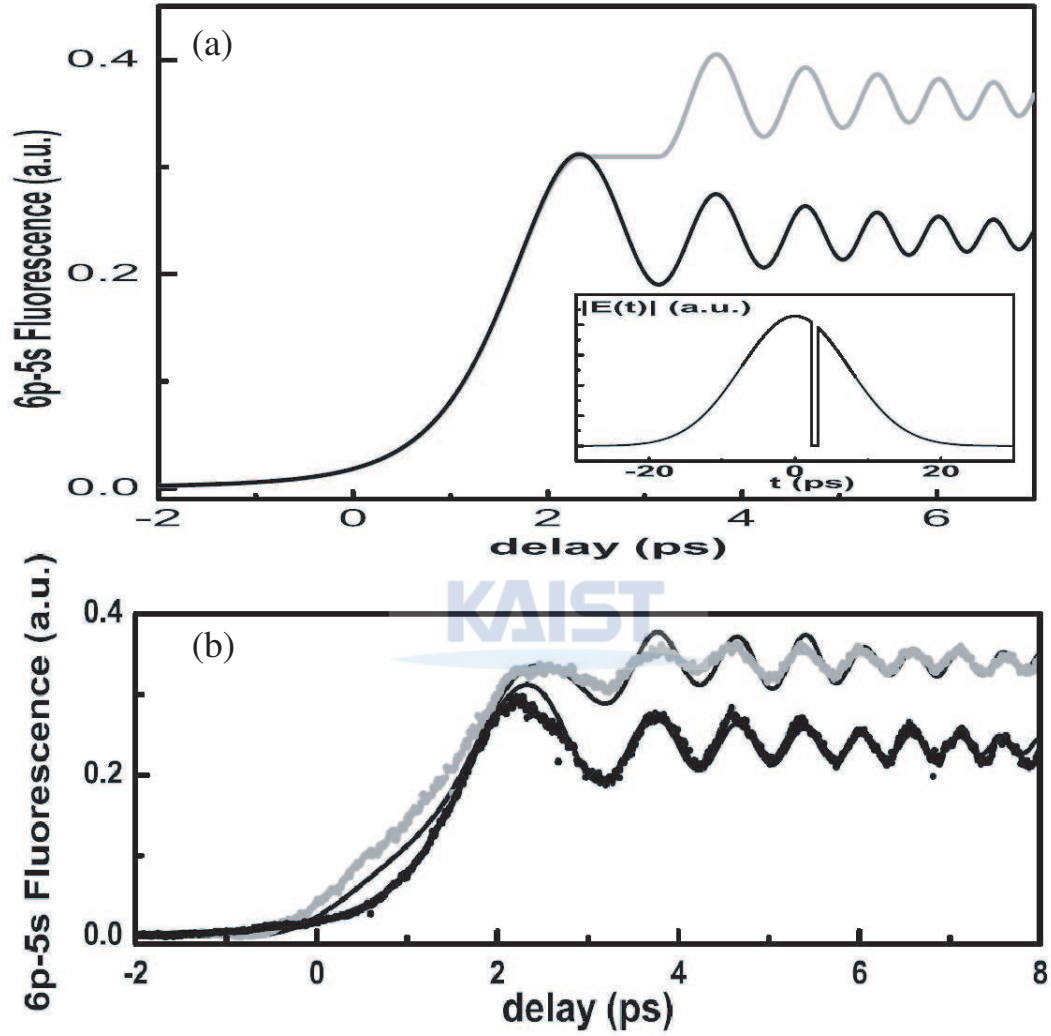


Figure 2.11: (a) Calculation results of excited transient population with unshaped (in amplitude) chirped pump pulse (black line) and with hole-shaped (in amplitude) in time domain chirped pulse (solid gray line) as the inset. The amount of chirp is same for both pulses. (b) Experimental results of excited state population (dots) and numerical calculation (line) with the pulse hole-shaped chirped pulse, with $\phi'' = -4.9 \times 10^5 fs^2$. [46]

Chapter 3. 2D Fourier transform optical spectroscopy

Today, the most important interests in Chemiphysics and Biophysics have been focused to the structural change of complex molecular systems during the chemical reactions or interactions with light and how the dynamics are related to important chemical and biological processes. Two-dimensional nuclear magnetic resonance(2D-NMR) technique simply comprises a series of one-dimensional NMR experiments, providing elevated information about molecules for the analysis of molecular structure. Despite the admirable capabilities, 2D-NMR is primarily limited to relatively small molecular systems, and their structural evolution which occurs in subpicoseconds time scale is too fast for 2D-NMR to trace. Alternatively, 2D Fourier transform optical spectroscopy (2D-FTOS), an optical extension of 2D-NMR, has been recently developed to probe femtosecond electronic and vibrational dynamics. It can be applied to molecules as large as small proteins and provides ultrafast time resolution which is crucial for understanding reaction dynamics and energy transfer processes [22].

Figure 3.1(a) shows an energy diagram of a V -type three-level system which comprises a ground state $|g\rangle$, and two adjacent excited states $|a\rangle$, and $|b\rangle$. Let us consider a case that the system interacts with a broadband laser pulse whose laser frequency, ω_0 , is near resonant to the excitation of $|a\rangle$ and $|b\rangle$. Then, for example, the population of $|b\rangle$ being transferred from $|a\rangle$ is coherently mixed with, and is difficult to separate from, the dominant one-photon transitions from the ground state. Therefore, the inter-excited state transition is difficult to measure. This difficulty of distinguishing the inter-excited state transition from the others is overcome by using quantum coherence of the system in 2D-FTOS. A 2D spectrum, which can be obtained in 2D-FTOS, represents a number of peaks as shown in Fig. 3.1(b). The peaks are inherent to their own transition pathways, and thereby the inter-excited state transition, or coupling, can be obtained from the 2D spectrum.

In this chapter, we discuss about 2D-FTOS. In Sec. 3.1, the notations used throughout the thesis for electric field is defined. In Sec. 3.2, the equation of transition probability amplitudes for a V -type system is derived in weak field interaction regime, where we use the perturbation theory. In Sec. 3.3, we discuss further about the principle of 2D-FTOS.

3.1 Electric field notation

We start by defining the electric field in frequency domain as

$$E(\omega) = A(\omega) \exp(i\phi(\omega)), \quad (3.1)$$

where $A(\omega)$ is the spectral amplitude, and $\phi(\omega)$ the spectral phase. For the case of gaussian pulse spectrally centered at ω_0 , the spectral amplitude is given as $A(\omega) = E_0 \exp[-\frac{(\omega-\omega_0)^2}{\Delta\omega^2}]$, where E_0 is the peak amplitude, $\Delta\omega$ the spectral bandwidth. $\phi(\omega)$ can be generally defined as a Taylor series expansion given by

$$\phi(\omega) = a_1(\omega - \omega_0) + \frac{a_2}{2!}(\omega - \omega_0)^2 + \frac{a_3}{3!}(\omega - \omega_0)^3 + \dots \quad (3.2)$$

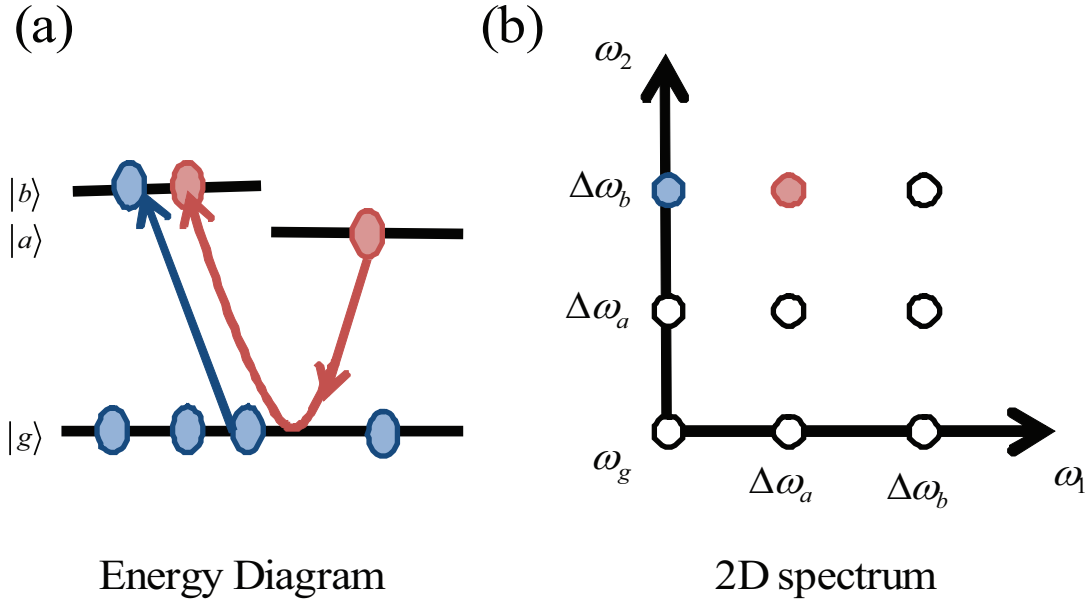


Figure 3.1: (a) Energy diagram of a V-type three-level system with one ground state $|g\rangle$ and two excited states $|a\rangle$ and $|b\rangle$. The transition energies of $|a\rangle$ and $|b\rangle$ from $|g\rangle$ are $\hbar\omega_a$ and $\hbar\omega_b$, respectively. The transition between $|a\rangle$ and $|b\rangle$ via $|g\rangle$ is presented by a red line and transition between $|b\rangle$ and $|g\rangle$ by a blue line. (b) 2D Fourier transformed spectra $S(\omega_1, \omega_2)$. The peak positions contain the transition pathways, and, for example, the transition $|a\rangle \rightarrow |b\rangle$ is presented by the red circle, and the transition $|g\rangle \rightarrow |b\rangle$ by the blue circle.

For the negative frequency regime, we use the relation $E(-\omega) = E^*(\omega)$, which is simply derived from the condition that $E(t)$ is real for all t , or

$$\begin{aligned}
\sqrt{2\pi}E(t) &= \int_{-\infty}^{\infty} d\omega E(\omega)e^{-i\omega t} \\
&= \int_{-\infty}^0 d\omega E(\omega)e^{-i\omega t} + \int_0^{\infty} d\omega E(\omega)e^{-i\omega t} \\
&= \int_0^{\infty} d\omega E(-\omega)e^{i\omega t} + \int_0^{\infty} d\omega E(\omega)e^{-i\omega t} \\
&= \int_0^{\infty} d\omega (E(-\omega)e^{i\omega t} + E(\omega)e^{-i\omega t}), \tag{3.3}
\end{aligned}$$

$$\begin{aligned}
\text{Im} [E(-\omega)e^{i\omega t}] &= -\text{Im} [E(\omega)e^{-i\omega t}] \\
\rightarrow E(-\omega) &= E^*(\omega). \tag{3.4}
\end{aligned}$$

Here, we assign $E(t)$ as the inverse Fourier transform of $E(\omega)$, and the last equation comes from that the imaginary part of the integrand must be zero for any $E(t)$. Hence, the negative frequency electric field can be defined as

$$E(\omega) = A(\omega) \exp(-i\phi(\omega)). \tag{3.5}$$

Note that the negative frequency electric field is defined only for the negative frequency region, i.e., $\omega < 0$, ω in Eq. (3.5) is positive.

Now, we derive the electric field in time domain for both in the positive and negative frequency regions. First, we start with the electric field of a gaussian pulse having the spectral components all

in phase, i.e., $\phi(\omega) = 0$. As defined in Eq. (3.3), we use the relation that $E(t)$ is the inverse Fourier transform of $E(\omega)$ for the positive spectral region. Then, the electric field is written as

$$\begin{aligned}
E(t) &= \frac{1}{\sqrt{2\pi}} \int_{-\infty}^{\infty} d\omega E(\omega) \exp(-i\omega t) \\
&= \frac{E_0}{\sqrt{2\pi}} \int_{-\infty}^{\infty} d\omega \exp\left(-\frac{(\omega - \omega_0)^2}{\Delta\omega^2}\right) \exp(-i\omega t) \\
&= \frac{E_0}{\sqrt{2\pi}} e^{-i\omega_0 t} \int_{-\infty}^{\infty} d\omega \exp\left(-\frac{\omega^2}{\Delta\omega^2} - i\omega t\right) \\
&= \frac{E_0}{\sqrt{2\pi}} \Delta\omega \sqrt{\pi} \exp(-i\omega_0 t) \exp\left(-\frac{\Delta\omega^2 t^2}{4}\right) \\
&= \frac{E_0 \Delta\omega}{\sqrt{2}} \exp\left(-\frac{t^2}{\tau_0^2} - i\omega_0 t\right), \tag{3.6}
\end{aligned}$$

where $\tau_0 = 2/\Delta\omega$ is the pulse width. Eq. (3.6) shows that the electric field spreads in time with a pulse width τ_0 centered at zero and oscillates with a laser frequency ω_0 . Likewise, the negative component can be written as

$$\begin{aligned}
E^-(t) &= \frac{1}{\sqrt{2\pi}} \int_{-\infty}^{\infty} d\omega E^*(\omega) \exp(i\omega t) \\
&= \frac{E_0 \Delta\omega}{\sqrt{2}} \exp\left(-\frac{t^2}{\tau_0^2} + i\omega_0 t\right). \tag{3.7}
\end{aligned}$$

Note that, $E^-(t)$ is Fourier transform of $E^*(\omega)$ for negative region.

Let us consider an electric field having a nonzero phase function. First, the pulse having the simplest phase function, which is the delay term, or a_1 of Taylor expansion coefficients, time domain electric field for positive frequency case is given by

$$\begin{aligned}
E(t) &= \frac{1}{\sqrt{2\pi}} \int_{-\infty}^{\infty} d\omega E(\omega) \exp(-i\omega t) \\
&= \frac{E_0}{\sqrt{2\pi}} \int_{-\infty}^{\infty} d\omega \exp\left(-\frac{(\omega - \omega_0)^2}{\Delta\omega^2}\right) \exp[ia_1(\omega - \omega_0)] \exp(-i\omega t) \\
&= \frac{E_0}{\sqrt{2\pi}} e^{-i\omega_0 t} \int_{-\infty}^{\infty} d\omega \exp\left[-\frac{\omega^2}{\Delta\omega^2} - i\omega(t - a_1)\right] \\
&= \frac{E_0 \Delta\omega}{\sqrt{2}} \exp\left(-\frac{(t - a_1)^2}{\tau_0^2} - i\omega_0 t\right). \tag{3.8}
\end{aligned}$$

The pulse in Eq. (3.8) is centered at $t = a_1$.

Another useful example of the phase function is the linear chirp (a_2). For this case, time domain electric field is

$$\begin{aligned}
E(t) &= \frac{1}{\sqrt{2\pi}} \int_{-\infty}^{\infty} d\omega E(\omega) \exp(-i\omega t) \\
&= \frac{E_0}{\sqrt{2\pi}} \int_{-\infty}^{\infty} d\omega \exp\left(-\frac{(\omega - \omega_0)^2}{\Delta\omega^2}\right) \exp\left[i\frac{a_2}{2}(\omega - \omega_0)^2\right] \exp(-i\omega t) \\
&= \frac{E_0}{\sqrt{2\pi}} e^{-i\omega_0 t} \int_{-\infty}^{\infty} d\omega \exp\left[-\frac{(1 - i\frac{a_2}{2}\Delta\omega^2)\omega^2}{\Delta\omega^2} - i\omega t\right] \\
&= \frac{E_0}{\sqrt{2\pi}} e^{-i\omega_0 t} \frac{\Delta\omega \sqrt{\pi}}{\sqrt{1 - i\frac{a_2}{2}\Delta\omega^2}} \exp\left[-\frac{\Delta\omega^2 t^2}{4(1 - i\frac{a_2}{2}\Delta\omega^2)}\right] \\
&= \frac{E_0 \Delta\omega}{\sqrt{2}} \sqrt{\frac{\tau_0}{\tau}} \exp\left[\frac{i}{2} \tan^{-1}\left(\frac{2a_2}{\tau_0^2}\right)\right] \exp\left[-\frac{t^2}{\tau_0^2} - i(\omega_0 t + \frac{2a_2}{\tau_0^4 + 4a_2^2} t^2)\right], \tag{3.9}
\end{aligned}$$

where $\tau = \tau_0 \sqrt{1 + 4a_2^2/\tau_0^4}$ is the chirped pulse width.

In the same way, the electric field in the negative frequency region can be written as following: for $\phi(\omega) = a_1(\omega - \omega_0)$,

$$E(t) = \frac{E_0 \Delta \omega}{\sqrt{2}} \exp\left(-\frac{(t - a_1)^2}{\tau_0^2} + i\omega_0 t\right), \quad (3.10)$$

and for $\phi(\omega) = \frac{a_2}{2}(\omega - \omega_0)^2$,

$$E(t) = \frac{E_0 \Delta \omega}{\sqrt{2}} \sqrt{\frac{\tau_0}{\tau}} \exp\left[-\frac{i}{2} \tan^{-1}\left(\frac{2a_2}{\tau_0^2}\right)\right] \exp\left[-\frac{t^2}{\tau_0^2} + i\left(\omega_0 t + \frac{2a_2}{\tau_0^4 + 4a_2^2} t^2\right)\right]. \quad (3.11)$$

3.2 Inter-excited state transitions in a V -type system

In this section, we derive the transition probability amplitudes for a V -type system. The system under consideration comprises one ground state $|g\rangle$ and two adjacent excited states $|a\rangle$ and $|b\rangle$ as shown in Fig. 3.1(a). Transitions of $|g\rangle \leftrightarrow |a\rangle$ and $|g\rangle \leftrightarrow |b\rangle$ are allowed and the direct transitions between $|a\rangle$ and $|b\rangle$ are forbidden. In this case, the hamiltonian of the system is

$$\begin{aligned} H(t) &= H_0 + V(t) \\ &= \begin{pmatrix} 0 & 0 & 0 \\ 0 & \hbar\omega_a & 0 \\ 0 & 0 & \hbar\omega_b \end{pmatrix} \\ &\quad + \begin{pmatrix} 0 & -\mu_{ga}E(t) & -\mu_{gb}E(t) \\ -\mu_{ag}E(t) & 0 & 0 \\ -\mu_{bg}E(t) & 0 & 0 \end{pmatrix}, \end{aligned} \quad (3.12)$$

where H_0 is time-independent bare hamiltonian of the quantum system, $\sum_n E_n |n\rangle\langle n|$, $E(t)$ the electric field interacting with the quantum system, μ_{ga} and μ_{gb} the transition dipole moments between the ground state $|g\rangle$ and the excited states $|a\rangle$ and $|b\rangle$, respectively. Note that, μ_{ng} is equal to μ_{gn} ($n=a$ or b) and μ_{ba} is zero.

The time evolution of the wavefunction $|\psi\rangle$ of the quantum system is given by the well known Schrödinger equation as

$$i\hbar \frac{\partial}{\partial t} |\psi\rangle = H |\psi\rangle. \quad (3.13)$$

The transition probability amplitudes is obtained using solely the interaction between the quantum system and the electric field. We use the interaction picture as follows. The wavefunction defined in the interaction picture, $|\psi(t)\rangle_I$, is

$$|\psi(t)\rangle_I = e^{iH_0 t/\hbar} |\psi(t)\rangle_S, \quad (3.14)$$

and the interaction picture Hamiltonian, $V_I(t)$, is

$$V_I(t) = e^{iH_0 t/\hbar} V(t) e^{-iH_0 t/\hbar}. \quad (3.15)$$

Then, the time evolution of wavefunction $|\psi\rangle$ in the interaction picture (i.e. Schrödinger equation in the

interaction picture) can be written as

$$\begin{aligned}
i\hbar \frac{\partial}{\partial t} |\psi(t)\rangle_I &= i\hbar \frac{\partial}{\partial t} (e^{iH_0 t/\hbar} |\psi(t)\rangle_S) \\
&= -H_0 e^{iH_0 t/\hbar} |\psi(t)\rangle_S + e^{iH_0 t/\hbar} H |\psi(t)\rangle_S \\
&= -H_0 e^{iH_0 t/\hbar} |\psi(t)\rangle_S + e^{iH_0 t/\hbar} (H_0 + V) |\psi(t)\rangle_S \\
&= e^{iH_0 t/\hbar} V e^{-iH_0 t/\hbar} e^{iH_0 t/\hbar} |\psi(t)\rangle_S \\
&= V_I |\psi(t)\rangle_I,
\end{aligned} \tag{3.16}$$

where the interaction picture Hamiltonian $V_I(t)$ is given by

$$\begin{aligned}
V_I(t) &= e^{iH_0 t/\hbar} V(t) e^{-iH_0 t/\hbar} \\
&= \begin{pmatrix} 0 & -\mu_{ga} E(t) e^{i\omega_{ga} t} & -\mu_{gb} E(t) e^{i\omega_{gb} t} \\ -\mu_{ag} E(t) e^{i\omega_{ag} t} & 0 & 0 \\ -\mu_{bg} E(t) e^{i\omega_{bg} t} & 0 & 0 \end{pmatrix}.
\end{aligned} \tag{3.17}$$

By integrating the Eq. (3.16), we obtain the transition probability amplitude between two states $|i\rangle$ and $|n\rangle$ as

$$c_{ni}(t) = \langle n | U_I(t, t_0) | i \rangle, \tag{3.18}$$

where U_I is a time evolution operator in the interaction picture given by

$$\begin{aligned}
U_I(t, t_0) &= 1 - \frac{i}{\hbar} \int_{t_0}^t V_I(t') U_I(t', t_0) dt' \\
&= 1 - \frac{i}{\hbar} \int_{t_0}^t V_I(t') \left[1 - \frac{i}{\hbar} \int_{t_0}^{t'} V_I(t'') U_I(t'', t_0) dt'' \right] dt' \\
&= 1 - \frac{i}{\hbar} \int_{t_0}^t V_I(t') dt' + \left(\frac{-i}{\hbar} \right)^2 \int_{t_0}^t dt' \int_{t_0}^{t'} dt'' V_I(t') V_I(t'', t_0) dt'' dt' \\
&+ \dots + \left(\frac{-i}{\hbar} \right)^n \int_{t_0}^t dt' \int_{t_0}^{t'} dt'' \dots \int_{t_0}^{t^{(n-1)}} dt^{(n)} V_I(t') V_I(t'') \dots V_I(t^{(n)}) \\
&+ \dots.
\end{aligned} \tag{3.19}$$

By separating U_I by the order of V_I , we can expand $c_{ni}(t)$ as

$$c_{ni}^{(0)}(t) = \delta_{ni} \tag{3.20}$$

$$\begin{aligned}
c_{ni}^{(1)}(t) &= \frac{-i}{\hbar} \int_{t_0}^t \langle n | V_I(t') | i \rangle dt' \\
&= \frac{-i}{\hbar} \int_{t_0}^t e^{i\omega_{ni} t'} V_{ni}(t') dt'
\end{aligned} \tag{3.21}$$

$$c_{ni}^{(2)}(t) = \left(\frac{-i}{\hbar} \right)^2 \sum_m \int_{t_0}^t dt' \int_{t_0}^{t'} dt'' e^{i\omega_{nm} t'} V_{nm}(t') e^{i\omega_{mi} t''} V_{mi}(t''), \tag{3.22}$$

where $c_{ni}^{(1)}(t)$ is the first order in $V_I(t)$, $c_{ni}^{(2)}(t)$ the second order in $V_I(t)$, and so on. The population of the state $|n\rangle$ that is transferred from the state $|i\rangle$ is

$$P(i \rightarrow n) = |c_{ni}^{(0)} + c_{ni}^{(1)} + c_{ni}^{(2)} + \dots|^2. \tag{3.23}$$

Now, we limit the integration intervals t_0 and t as $-\infty$ and ∞ respectively, because we want to obtain the transition probability amplitudes after the interaction is over. The pulse duration is assumed here

considerably shorter than all lifetimes involved. Then, the first order transition probability amplitude $c_{ni}^{(1)}$ is obtained as

$$\begin{aligned} c_{ni}^{(1)} &= \frac{i\mu_{ni}}{\hbar} \int_{-\infty}^{\infty} dt_1 E(t_1) e^{i\omega_{ni}t} \\ &= \frac{i\mu_{ni}}{\hbar} \sqrt{2\pi} E(\omega_{ni}) \end{aligned} \quad (3.24)$$

where $E(\omega_{ni})$ is the resonance frequency component of the electric field. The second order transition probability amplitude, $c_{ni}^{(2)}$, can be derived from Eq. (4.6). We consider the case that, for example, $|n\rangle$ and $|i\rangle$ are the two excited states $|b\rangle$ and $|a\rangle$. The transition is achieved via the ground state $|g\rangle$. In this case, $-\omega_{ag}$ and ω_{bg} are the resonance frequencies, respectively. Then, $c_{ba}^{(2)}$ is given by

$$\begin{aligned} c_{ba}^{(2)}(t) &= -\frac{\mu_{bg}\mu_{ga}}{\hbar^2} \int_{t_0}^t dt' \int_{t_0}^{t'} dt'' e^{i\omega_{bg}t'} E(t') e^{i\omega_{ga}t''} E(t'') \\ &= -\frac{\mu_{bg}\mu_{ga}}{2\pi\hbar^2} \int_{t_0}^t dt' \int_{t_0}^{t'} dt'' e^{i\omega_{bg}t'} \left[\int_{-\infty}^{\infty} d\omega_1 e^{-i\omega_1 t'} E(\omega_1) \right] e^{-i\omega_{ag}t''} \left[\int_{-\infty}^{\infty} d\omega_2 e^{i\omega_2 t''} E^*(\omega_2) \right]. \end{aligned} \quad (3.25)$$

Note that, since the first one-photon transition process involved in the t'' integration is de-excitation, we use the complex conjugate of the frequency domain electric field and its Fourier transform. Then, $c_{ba}^{(2)}(t)$ becomes

$$\begin{aligned} c_{ba}^{(2)}(t) &= -\frac{\mu_{bg}\mu_{ga}}{2\pi\hbar^2} \int_{-\infty}^{\infty} d\omega_1 E(\omega_1) \int_{-\infty}^{\infty} d\omega_2 E^*(\omega_2) \int_{t_0}^t dt' e^{i(\omega_{bg}-\omega_1)t'} \int_{t_0}^{t'} dt'' e^{-i(\omega_{ag}-\omega_2)t''} \\ &= -\frac{\mu_{bg}\mu_{ga}}{2\pi\hbar^2} \int_{-\infty}^{\infty} d\omega_1 E(\omega_1) \int_{-\infty}^{\infty} d\omega_2 E^*(\omega_2) \int_{t_0}^t dt' e^{i(\omega_{bg}-\omega_1)t'} \frac{e^{-i(\omega_{ag}-\omega_2)t'} - e^{-i(\omega_{ag}-\omega_2)t_0}}{-i(\omega_{ag}-\omega_2)} \\ &= -\frac{\mu_{bg}\mu_{ga}}{2\pi\hbar^2} \int_{-\infty}^{\infty} d\omega_1 E(\omega_1) \int_{-\infty}^{\infty} d\omega_2 E^*(\omega_2) \\ &\quad \times \left[\frac{e^{i(\omega_{bg}-\omega_1-\omega_{ag}+\omega_2)t} - e^{i(\omega_{bg}-\omega_1-\omega_{ag}+\omega_2)t_0}}{-i(\omega_{ag}-\omega_2) i(\omega_{bg}-\omega_1-\omega_{ag}+\omega_2)} - \frac{e^{i(\omega_{bg}-\omega_1)t} - e^{i(\omega_{bg}-\omega_1)t_0}}{-i(\omega_{ag}-\omega_2) i(\omega_{bg}-\omega_1)} e^{-i(\omega_{ag}-\omega_2)t_0} \right]. \end{aligned} \quad (3.26)$$

Finally, using the Residue Theorem, $c_{ba}^{(2)}$ is arranged as

$$c_{ba}^{(2)} = i \frac{\mu_{bg}\mu_{ga}}{\hbar^2} \left[i\pi E^*(\omega_{ag}) E(\omega_{bg}) - \wp \int d\omega \frac{E^*(\omega) E(\omega_{ba} + \omega)}{\omega_{ag} - \omega} \right], \quad (3.27)$$

where \wp is the Cauchy principal value. Further discussion of Eq. (3.27) are provided in Chap. 5 in comparison with the case of one-photon transition in a two-level system.

3.3 Three pulse coherent control scheme

Common 2D-FTOS experiments are performed with three optical pulses, which are used to interact with a quantum system. Briefly, each pulse has distinct role as follows: the first pulse (α) can be regarded as a preparation pulse which starts coherence of the quantum system, the second pulse (β) is a coupling pulse which transfers the coherence among the excited states, and the third pulse (γ) is a measurement pulse which measures the evolution trajectory of the wavefunction of the system. Here again, we consider a V -type system composes $|g\rangle$, $|a\rangle$, and $|b\rangle$. All the other conditions are the same as in the previous section except that the interacting electric field is now three optical pulses. The first pulse interacts with the system at time zero, $t = 0$, and the second and the third pulses at $t = \tau_1$ and $t = \tau_1 + \tau_2$, respectively.

The quantum system is initially in the ground state, i.e.,

$$|\psi(t = 0_-)\rangle = |g\rangle. \quad (3.28)$$

If we assume the interaction between the quantum system and the electric field is in the weak field regime, $\frac{\mu_{ni}E(t)}{\hbar} \ll 1$ for all t , we can neglect the higher order terms of V_I . By considering the lowest order for each transition path, the time evolution operator in the interaction picture for the first pulse (α) can be written as

$$U_I(\alpha) = \begin{pmatrix} 1 & \alpha_{ga}^{(1)} & \alpha_{gb}^{(1)} \\ \alpha_{ag}^{(1)} & 1 & \alpha_{ab}^{(2)} \\ \alpha_{bg}^{(1)} & \alpha_{ba}^{(2)} & 1 \end{pmatrix}. \quad (3.29)$$

Note that, if the initial and final states are switched, the one-photon transitions are simply the complex conjugates, i.e., $\alpha_{ga}^{(1)} = \alpha_{ag}^{(1)*}$. However, this relation does not hold for two-photon transitions, $\alpha_{ba}^{(2)} \neq \alpha_{ab}^{(2)*}$. The wavefunction after the interaction with the first pulse becomes

$$\begin{aligned} |\psi(t = 0_+)\rangle &= U_I(\alpha)|\psi(t = 0_-)\rangle \\ &= |g\rangle + \alpha_{ag}^{(1)}|a\rangle + \alpha_{bg}^{(1)}|b\rangle. \end{aligned} \quad (3.30)$$

During the delay time between the first pulse and the second pulse, $0 < t < \tau_1$, the interaction hamiltonian is an identity, i.e.,

$$U_I(0 < t < \tau_1) = \begin{pmatrix} 1 & 0 & 0 \\ 0 & 1 & 0 \\ 0 & 0 & 1 \end{pmatrix}. \quad (3.31)$$

So, the wavefunction is unchanged. The delay is appended to the evolution operator of the second pulse as relative phase shift corresponding to the energy of each state. To separate the effect of the delay from the transition probability amplitude, we change the variable $\tilde{t} = t' - \tau_1$, so that the center of second pulse is centered at $\tilde{t} = 0$. Then, the one-photon transition probability amplitudes becomes

$$\begin{aligned} c_{ng}^{(1)} &= \frac{-i}{\hbar} \int_{-\infty}^{\infty} e^{i\omega_{ng}t'} V_{ng}(t') dt' \\ &= \frac{-i}{\hbar} \int_{-\infty}^{\infty} e^{i\omega_{ng}\tilde{t}} e^{i\omega_{ng}\tau_1} V_{ng}(\tilde{t}) e^{-i\omega_0\tau_1} d\tilde{t} \\ &= e^{i(\omega_{ng}-\omega_0)\tau_1} \beta_{ng}^{(1)}, \end{aligned} \quad (3.32)$$

and for the two-photon transition,

$$\begin{aligned} c_{ni}^{(2)} &= \left(\frac{-i}{\hbar}\right)^2 \int_{-\infty}^{\infty} d\tilde{t} \int_{-\infty}^{\tilde{t}} d\hat{t} e^{i\omega_{ng}\tilde{t}} e^{i\omega_{ng}\tau_1} V_{ng}(\tilde{t}) e^{-i\omega_0\tau_1} e^{i\omega_{gi}\hat{t}} e^{i\omega_{gi}\tau_1} V_{mi}(\hat{t}) e^{i\omega_0\tau_1} \\ &= e^{i[(\omega_{ng}-\omega_0)\tau_1 - (\omega_{gi}-\omega_0)\tau_1]} \beta_{ni}^{(2)}, \end{aligned} \quad (3.33)$$

where the rotating wave approximation is used. In this way, if the first pulse and the second pulse are the same except for the delay, then the transition probability amplitude in both cases are the same, i.e., $\alpha_{ni} = \beta_{ni}$. Then, the interaction hamiltonian for the second pulse is given by

$$U_I(\beta) = \begin{pmatrix} 1 & e^{-i\Delta\omega_{ag}\tau_1} \beta_{ag}^{(1)*} & e^{-i\Delta\omega_{bg}\tau_1} \beta_{bg}^{(1)*} \\ e^{i\Delta\omega_{ag}\tau_1} \beta_{ag}^{(1)} & 1 & e^{i(\Delta\omega_{ag}-\Delta\omega_{bg})\tau_1} \beta_{ab}^{(2)} \\ e^{i\Delta\omega_{bg}\tau_1} \beta_{bg}^{(1)} & e^{-i(\Delta\omega_{ag}-\Delta\omega_{bg})\tau_1} \beta_{ba}^{(2)} & 1 \end{pmatrix}, \quad (3.34)$$

coeff.	τ_1	τ_2
$\alpha_{bg}^{(1)}$	0	0
$\beta_{bg}^{(1)}$	$\Delta\omega_{bg}$	0
$\gamma_{bg}^{(1)}$	$\Delta\omega_{bg}$	$\Delta\omega_{bg}$
$\alpha_{ag}^{(1)}\beta_{ba}^{(2)}$	$\Delta\omega_{bg} - \Delta\omega_{ag}$	0
$\alpha_{ag}^{(1)}\gamma_{ba}^{(2)}$	$\Delta\omega_{bg} - \Delta\omega_{ag}$	$\Delta\omega_{bg} - \Delta\omega_{ag}$
$\beta_{ag}^{(1)}\gamma_{ba}^{(2)}$	$\Delta\omega_{bg}$	$\Delta\omega_{bg} - \Delta\omega_{ag}$
$\alpha_{ag}^{(1)}\beta_{ag}^{(1)*}\gamma_{bg}^{(1)}$	$\Delta\omega_{bg} - \Delta\omega_{ag}$	$\Delta\omega_{bg}$
$\alpha_{bg}^{(1)}\beta_{bg}^{(1)*}\gamma_{bg}^{(1)}$	0	$\Delta\omega_{bg}$
$\alpha_{bg}^{(1)}\beta_{ab}^{(2)}\gamma_{ba}^{(2)}$	0	$\Delta\omega_{bg} - \Delta\omega_{ag}$

Table 3.1: Probability amplitude coefficients of $|b\rangle$ are sorted in accordance with the phase dependence on inter-pulse delays. $|b\rangle$ in Eq. (3.37) can be retrieved from this table: for example, the coefficient of fourth line, $\alpha_{ag}^{(1)}\beta_{ba}^{(2)}$, times phase dependence on τ_1 , $e^{i(\Delta\omega_{bg}-\Delta\omega_{ag})\tau_1}$, times phase dependence on τ_2 , unity, equals $\alpha_{ag}^{(1)}\beta_{ba}^{(2)}e^{i(\Delta\omega_{bg}-\Delta\omega_{ag})\tau_1}$.

where $\Delta\omega_{ag} = \omega_{ag} - \omega_0$. And the wavefunction is given by

$$|\psi_{(t=\tau_1+)}\rangle = \begin{pmatrix} 1 + \alpha_{ag}^{(1)}\beta_{ag}^{(1)*}e^{-i\Delta\omega_{ag}\tau_1} + \alpha_{bg}^{(1)}\beta_{bg}^{(1)*}e^{-i\Delta\omega_{bg}\tau_1} \\ \beta_{ag}^{(1)}e^{i\Delta\omega_{ag}\tau_1} + \alpha_{ag}^{(1)} + \alpha_{bg}^{(1)}\beta_{ab}^{(2)}e^{i(\Delta\omega_{ag}-\Delta\omega_{bg})\tau_1} \\ \beta_{bg}^{(1)}e^{i\Delta\omega_{bg}\tau_1} + \alpha_{ag}^{(1)}\beta_{ba}^{(2)}e^{-i(\Delta\omega_{ag}-\Delta\omega_{bg})\tau_1} + \alpha_{bg}^{(1)} \end{pmatrix}. \quad (3.35)$$

During the time delay between the second and the third pulses, $\tau_1 < t < \tau_1 + \tau_2$, the wavefunction remains unchanged. The interaction hamiltonian for the third pulse is given by

$$U_I(\gamma) = \begin{pmatrix} 1 & e^{-i\Delta\omega_{ag}(\tau_1+\tau_2)}\gamma_{ag}^{(1)*} & e^{-i\Delta\omega_{bg}(\tau_1+\tau_2)}\gamma_{bg}^{(1)*} \\ e^{i\Delta\omega_{ag}(\tau_1+\tau_2)}\gamma_{ag}^{(1)} & 1 & e^{i(\Delta\omega_{ag}-\Delta\omega_{bg})(\tau_1+\tau_2)}\gamma_{ab}^{(2)} \\ e^{i\Delta\omega_{bg}(\tau_1+\tau_2)}\gamma_{bg}^{(1)} & e^{-i(\Delta\omega_{ag}-\Delta\omega_{bg})(\tau_1+\tau_2)}\gamma_{ba}^{(2)} & 1 \end{pmatrix}. \quad (3.36)$$

The final wavefunction after all the interactions with three pulses is written as follows:

$$|\psi_{(t=\tau_1+\tau_2+)}\rangle = \begin{pmatrix} |g\rangle \\ |a\rangle \\ |b\rangle = \gamma_{bg}^{(1)}e^{i\Delta\omega_{bg}(\tau_1+\tau_2)} + \alpha_{ag}^{(1)}\beta_{ag}^{(1)*}\gamma_{bg}^{(1)}e^{i(\Delta\omega_{bg}-\Delta\omega_{ag})\tau_1+i\Delta\omega_{bg}\tau_2} + \alpha_{bg}^{(1)}\beta_{bg}^{(1)*}\gamma_{bg}^{(1)}e^{i\Delta\omega_{bg}\tau_2} \\ + \beta_{ag}^{(1)}\gamma_{ba}^{(2)}e^{i\Delta\omega_{bg}\tau_1+i(\Delta\omega_{bg}-\Delta\omega_{ag})\tau_2} + \alpha_{ag}^{(1)}\gamma_{ba}^{(2)}e^{i(\Delta\omega_{bg}-\Delta\omega_{ag})(\tau_1+\tau_2)} + \alpha_{bg}^{(1)}\beta_{ab}^{(2)}\gamma_{ba}^{(2)}e^{i(\Delta\omega_{bg}-\Delta\omega_{ag})\tau_2} \\ + \beta_{bg}^{(1)}e^{i\Delta\omega_{bg}\tau_1} + \alpha_{ag}^{(1)}\beta_{ba}^{(2)}e^{i(\Delta\omega_{bg}-\Delta\omega_{ag})\tau_1} + \alpha_{bg}^{(1)} \end{pmatrix}. \quad (3.37)$$

We omit the notation $|g\rangle$ and $|a\rangle$, since we can explain the entire physical meaning of the three pulse interaction from $|b\rangle$ without them. The coefficients of probability amplitude of $|b\rangle$ are sorted in TABLE 3.1 according to the frequency dependence on τ_1 and τ_2 .

The final population, or the probability, $P_b = |\langle b|\psi\rangle|^2$ is given by (up to the lowest order of each τ_1 and τ_2 dependence)

$$P_b = (\alpha_{bg}^{(2)2} + \beta_{bg}^{(2)2} + \gamma_{bg}^{(2)2} + \dots) + \dots + \alpha_{ag}^{(1)*}\beta_{ba}^{(2)*}\gamma_{bg}^{(1)}e^{i(\Delta\omega_{ag}\tau_1+\Delta\omega_{bg}\tau_2)} + \dots \quad (3.38)$$

where, for example, the term $\alpha_{ag}^{(1)*} \beta_{ba}^{(2)*} \gamma_{bg}^{(1)} \exp(i\Delta\omega_{ag}\tau_1 + i\Delta\omega_{bg}\tau_2)$ denotes the quantum interference between the two transitions $|g\rangle \rightarrow |a\rangle \rightarrow |b\rangle \rightarrow$ and $|g\rangle \rightarrow |b\rangle$. The coefficient $\alpha_{ag}^{(1)*} \beta_{ba}^{(2)*} \gamma_{bg}^{(1)}$ is retrieved from $|\langle b|\psi\rangle|^2$, as the amplitude and phase of the temporally modulated component with the function $\exp(i\Delta\omega_{ag}\tau_1 + i\Delta\omega_{bg}\tau_2)$. The modulations $\exp(i\Delta\omega_{ag}\tau_1)$ and $\exp(i\Delta\omega_{bg}\tau_2)$ are due to the phase evolutions of the atom, respectively, in state $|a\rangle$ during τ_1 and in state $|b\rangle$ during τ_2 . The 2D Fourier-transform spectrum is then defined as

$$S(\omega_1, \omega_2) = \int \int P_b(\tau_1, \tau_2) e^{-i(\omega_1 \tau_1 + \omega_2 \tau_2)} d\tau_1 d\tau_2, \quad (3.39)$$

which has 49 peaks including a zero frequency peak. The coefficients of the spectral peaks of $S(\omega_1, \omega_2)$ of the two-dimensional plane are listed in TABLE 3.2 and TABLE 3.3. Aside from the constant $\alpha_{ag}^{(1)*} \gamma_{bg}^{(1)}$, the inter-excited state transition probability amplitude $\beta_{ba}^{(2)*}$ is then retrieved from the peak located at $(\omega_1, \omega_2) = (\Delta\omega_{ag}, \Delta\omega_{bg})$. As a result, the three-pulse coherent control scheme devised for 2D Fourier-transform spectroscopy can be used to measure the two-photon inter-excited states transition coefficients.



	$-\Delta\omega_{bg}$	$-\Delta\omega_{bg} + \Delta\omega_{ag}$	$-\Delta\omega_{ag}$	0
$\Delta\omega_{bg}$	$\alpha_{bg}^{(1)*} \beta_{bg}^{(1)*} \gamma_{bg}^{(1)}$	$\alpha_{ag}^{(1)*} \beta_{bg}^{(1)*} \beta_{ba}^{(2)*} \gamma_{bg}^{(1)}$	$\alpha_{ag}^{(1)} \beta_{ag}^{(1)*} \beta_{bg}^{(1)*} \gamma_{bg}^{(1)}$	$\beta_{bg}^{(1)} \gamma_{bg}^{(1)}$
$\Delta\omega_{bg} - \Delta\omega_{ag}$	$\alpha_{bg}^{(1)*} \beta_{bg}^{(2)*} \beta_{ab}^{(2)} \gamma_{ba}^{(2)}$	$\alpha_{ag}^{(1)*} \beta_{ba}^{(2)*} \beta_{ab}^{(2)} \gamma_{ba}^{(2)}$	$\alpha_{ag}^{(1)} \beta_{bg}^{(1)*} \gamma_{ba}^{(2)}$	$\beta_{ag}^{(1)*} \beta_{bg}^{(1)} \gamma_{ba}^{(2)}$
$\Delta\omega_{ag}$	$\alpha_{bg}^{(1)*} \beta_{bg}^{(1)*} \gamma_{bg}^{(2)*} \gamma_{ba}^{(2)}$	$\alpha_{ag}^{(1)*} \beta_{bg}^{(1)*} \gamma_{bg}^{(2)*} \gamma_{ba}^{(2)}$	$\alpha_{ag}^{(1)} \beta_{ag}^{(1)*} \beta_{bg}^{(1)*} \gamma_{ba}^{(2)}$	$\beta_{ag}^{(1)} \gamma_{ba}^{(2)}$
0	$\alpha_{bg}^{(1)} \beta_{bg}^{(1)}$	$\alpha_{ag}^{(1)} \alpha_{bg}^{(1)} \beta_{ba}^{(2)}$	$\alpha_{ag}^{(1)} \beta_{bg}^{(1)} \beta_{ba}^{(2)} +$	$\alpha_{bg}^2 + \beta_{bg}^2 + \gamma_{bg}^2$
$-\Delta\omega_{ag}$	$\alpha_{bg}^{(1)} \beta_{ab}^{(2)} \gamma_{bg}^{(1)*} \gamma_{ba}^{(2)}$	$\alpha_{ag}^{(1)*} \alpha_{bg}^{(1)} \beta_{ab}^{(2)} \gamma_{bg}^{(1)*} \gamma_{ba}^{(2)}$	$\alpha_{ag}^{(1)} \gamma_{bg}^{(1)*} \gamma_{ba}^{(2)}$	$\beta_{ag}^{(1)} \gamma_{bg}^{(1)} \gamma_{ba}^{(2)}$
$-\Delta\omega_{bg} + \Delta\omega_{ag}$	$\alpha_{bg}^{(1)} \beta_{ag}^{(1)*} \gamma_{ba}^{(2)*}$	$\alpha_{ag}^{(1)*} \alpha_{bg}^{(1)} \beta_{ba}^{(2)} \gamma_{ba}^{(2)*}$	$\alpha_{ag}^{(1)} \beta_{ag}^{(1)*} \beta_{ba}^{(2)} \gamma_{ba}^{(2)*}$	$\beta_{ag}^{(1)*} \beta_{bg}^{(1)} \gamma_{ba}^{(2)}$
$-\Delta\omega_{bg}$	$\alpha_{bg}^{(1)} \gamma_{bg}^{(1)*}$	$\alpha_{ag}^{(1)*} \alpha_{bg}^{(1)} \beta_{ag}^{(1)*} \gamma_{bg}^{(1)}$	$\alpha_{ag}^{(1)} \beta_{ba}^{(2)} \gamma_{bg}^{(1)*}$	$\beta_{bg}^{(1)} \gamma_{bg}^{(1)}$

Figure 3.2: Peaks of 2D Fourier transform plane of $| \langle b | \psi \rangle |^2$ state population coefficients (left part). Row and column are Fourier transform of τ_1 and τ_2 respectively, and categorized with the coefficients of τ_1 and τ_2 . This table directly map the dependence of peak values of 2D-FT spectra on the three pulse transitions. For example, the peak at $(\Delta\omega_{ag}, \Delta\omega_{bg})$ represents the quantum interference between $|g\rangle \rightarrow |a\rangle \rightarrow |b\rangle \rightarrow$ and $|g\rangle \rightarrow |b\rangle$ transitions. Note that, (n, m) coefficient, where n is row index and m is column index, is complex conjugate of (8-n, 8-m) coefficient.

	0	$\Delta\omega_{ag}$	$\Delta\omega_{bg} - \Delta\omega_{ag}$	$\Delta\omega_{bg}$
$\Delta\omega_{bg}$	$\beta_{bg}^{(1)}\gamma_{bg}^{(1)}$	$\alpha_{ag}^{(1)*}\beta_{ba}^{(2)*}\gamma_{bg}^{(1)}$	$\alpha_{ag}^{(1)}\alpha_{bg}^{(1)*}\beta_{ag}^{(1)*}\gamma_{bg}^{(1)}$	$\alpha_{bg}^{(1)*}\gamma_{bg}^{(1)}$
$\Delta\omega_{bg} - \Delta\omega_{ag}$	$\beta_{ag}^{(1)*}\beta_{bg}^{(1)}\gamma_{ba}^{(2)}$	$\alpha_{ag}^{(1)*}\beta_{ag}^{(1)}\beta_{ba}^{(2)*}\gamma_{ba}^{(2)}$	$\alpha_{ag}^{(1)}\alpha_{bg}^{(1)*}\gamma_{ba}^{(2)}$	$\alpha_{bg}^{(1)*}\beta_{ag}^{(1)}\gamma_{ba}^{(2)}$
$\Delta\omega_{ag}$	$\beta_{ag}^{(1)}\gamma_{bg}^{(1)}\gamma_{ba}^{(2)}$	$\alpha_{ag}^{(1)*}\gamma_{bg}^{(1)}\gamma_{ba}^{(2)*}$	$\alpha_{ag}^{(1)}\alpha_{bg}^{(1)*}\beta_{ag}^{(2)*}\gamma_{bg}^{(1)}\gamma_{ba}^{(2)}$	$\alpha_{bg}^{(1)*}\beta_{ag}^{(2)*}\gamma_{bg}^{(1)}\gamma_{ba}^{(2)}$
0	$\alpha_{bg}^2 + \beta_{bg}^2 + \gamma_{bg}^2$	$\alpha_{ag}^{(1)}\beta_{bg}^{(1)}\beta_{ba}^{(2)}$	$\alpha_{ag}^{(1)}\alpha_{bg}^{(1)}\beta_{ba}^{(2)}$	$\alpha_{bg}^{(1)}\beta_{bg}^{(1)}$
$-\Delta\omega_{ag}$	$\beta_{ag}^{(1)}\gamma_{bg}^{(1)}\gamma_{ba}^{(2)}$	$\alpha_{ag}^{(1)*}\beta_{ag}^{(1)}\beta_{bg}^{(1)}\gamma_{ba}^{(2)}$	$\alpha_{ag}^{(1)}\alpha_{bg}^{(1)*}\beta_{bg}^{(1)}\gamma_{ba}^{(2)}$	$\alpha_{bg}^{(1)*}\beta_{ag}^{(1)}\beta_{bg}^{(1)}\gamma_{ba}^{(2)}$
$-\Delta\omega_{bg} + \Delta\omega_{ag}$	$\beta_{ag}^{(1)*}\beta_{bg}^{(1)}\gamma_{ba}^{(2)}$	$\alpha_{ag}^{(1)*}\beta_{ag}^{(1)}\gamma_{ba}^{(2)*}$	$\alpha_{ag}^{(1)}\alpha_{bg}^{(1)*}\beta_{ba}^{(2)*}\gamma_{ba}^{(2)}$	$\alpha_{bg}^{(1)*}\beta_{ag}^{(1)}\beta_{ba}^{(2)*}\gamma_{ba}^{(2)}$
$-\Delta\omega_{bg}$	$\beta_{bg}^{(1)}\gamma_{bg}^{(1)}$	$\alpha_{ag}^{(1)*}\beta_{ag}^{(1)}\beta_{bg}^{(1)}\gamma_{bg}^{(1)}$	$\alpha_{ag}^{(1)}\alpha_{bg}^{(1)*}\beta_{bg}^{(1)}\gamma_{bg}^{(1)}$	$\alpha_{bg}^{(1)*}\beta_{bg}^{(1)}\gamma_{bg}^{(1)}$

Figure 3.3: Peaks of 2D Fourier transform plane of $|\langle b|\psi\rangle|^2$ state population coefficients (right part). Row and column are Fourier transform of τ_1 and τ_2 respectively, and categorized with the coefficients of τ_1 and τ_2 . This table directly map the dependence of peak values of 2D-FT spectra on the three pulse transitions. For example, the peak at $(\Delta\omega_{ag}, \Delta\omega_{bg})$ represents the quantum interference between $|g\rangle \rightarrow |a\rangle \rightarrow |b\rangle \rightarrow$ and $|g\rangle \rightarrow |b\rangle$ transitions. Note that, (n, m) coefficient, where n is row index and m is column index, is complex conjugate of (8-n, 8-m) coefficient.

Chapter 4. 2D Fourier transform coherent control spectroscopy (2D-FTCCS)

Quantum mechanical control of matters, known as quantum control or coherent control, utilizes programmed light forms, and has become one of the general scientific subjects of extreme interest because of its unprecedented control capability over the dynamics of atoms and molecules as discussed in Chap. 2. However, not many analytical solutions are known despite the great efforts to describe the shaped-pulse control of transition probabilities even in simple atomic systems. Moreover, these previous researches are restricted to the transitions from a ground state to excited states, mainly due to the limitation of detection techniques. In ladder-type systems, for example, the transition probability can be easily measured by detecting the target excited-state fluorescence. On the other hand, in a V -type system, especially if we consider the transition from one of the excited states to the other, the inter-excited state transition is not straightforward to measure and thus difficult to control. This difficulty in the V -type system can be resolved in 2D-FTOS as discussed in Chap. 3.

Now, we discuss about the coherent control capability in 2D-FTOS, or 2D Fourier transform coherent control spectroscopy (2D-FTCCS) [49]. In this chapter, we give the experimental demonstration of coherent control of inter-excited states transitions in rubidium atom. To do this, we adopt the three-pulse coherent control scheme in 2D-FTOS setting [60]: the target transition probability can be retrieved from the distinct 2D Fourier-transform spectral peaks that are inherent to their transition pathways, and thereby the controlled transition probability amplitude is obtained.

This chapter contains 3 sections. The experimental setup is given in Sec. 4.1. In Sec. 4.2, we discuss the advantage of pulse-shaping of the first pulse: for example, spectral hole shaping is used to prepare special initial wave function of the quantum system. In Sec. 4.3, we represent two experiments of coherent control of inter-excited state transitions: one is the selective turn on and off of the $5P_{1/2}$ - $5P_{3/2}$ transition of atomic rubidium (Rb), and the other is the quantum interference engineering which utilizes both amplitude- and phase-shaping of the second pulse. The experimental demonstrations in this chapter are focused on effective detecting of the directional inter-excited state transitions, $|a\rangle \rightarrow |b\rangle$.

4.1 Experimental description

For the experimental demonstration of 2D-FTCCS, we have used the three-pulse coherent control scheme described in Chap. 3. Briefly to summarize, we use three optical pulses among which the second pulse (β) is the control pulse shaped to induce two-photon inter-excited state transition from $|a\rangle$ to $|b\rangle$. (See Fig. 4.1(a)). Prior to the second pulse, the atoms need to be excited to $|a\rangle$ by the first pulse (α). In addition, the third pulse (γ) induces the quantum interference which is used to measure $c_{ba}^{(2)}$. After the all three interactions, the excited state population $P_b(\tau_1, \tau_2)$ is measured as a function of two time intervals τ_1 and τ_2 . Then, from the 2D Fourier-transform spectrum of $P_b(\tau_1, \tau_2)$, that is $S(\omega_1, \omega_2)$, the spectral peak located at $(\omega_1, \omega_2) = (\omega_{ag} - \omega_0, \omega_{bg} - \omega_0)$ reveals the controlled transition probability amplitude $c_{ba}^{(2)}(a_2, a_3)$.

In the experiment, we used the lowest three energy levels of Rb (See Fig. 4.1(b)) at room temperature

273 K. The energy states $|a\rangle=5P_{1/2}$ and $|b\rangle=5P_{3/2}$ were resonantly excited from the common ground state $|g\rangle=5S_{1/2}$, so these three energy states comprise an ideally coupled V -type system. D_1 transition has resonant angular frequency at $\omega_{ag} = 2371.7$ rad. THz, which corresponds to wavelength of $\lambda_{ag} = 794.76$ nm, the dipole moment $\mu_{ag} = 2.537 \times 10^{-29}$ Cm, and the decay rate (Natural Line Width(FWHM)) $\Gamma_{ag} = 5.7468$ MHz. D_2 transition has $\omega_{bg} = 2416.5$ rad. THz ($\lambda_{bg} = 780.02$ nm), the dipole moment $\mu_{bg} = 3.584 \times 10^{-29}$ Cm, and the decay rate $\Gamma_{bg} = 6.0659$ MHz. The boiling temperature of Rb is 688° C. At room temperature, Rb is in solid phase and the vapor pressure is $P_v = 2.25 \times 10^{-7}$ Torr from the vapor-pressure model given by [88]. The corresponding density was calculated by $\rho = \frac{P}{k_B T} = 7.42 \times 10^9 / \text{cm}^3$. The mean free path can be calculated by $l = \frac{k_B T}{\sqrt{2} \pi d^2 P}$ where d is diameter of the gas particles. The Van der Waals radius of Rubidium is 303 pm, and the mean free path is 82.6 m. The most probable speed is 236.73 m/s. The corresponding collision coherence time is 349 ms. ^{87}Rb is not a stable isotope of rubidium, decaying to $\beta^- + ^{87}\text{Sr}$ with a total disintegration energy of 0.283 MeV [89], but has an extremely slow decay rate: the nuclear life time of rubidium is $4.88 \times 10^{10} \text{yr}$. Thus, ^{87}Rb is effectively stable. Therefore, we can assume ^{87}Rb as in coherent state for sub-ps time scale under considered.

The experimental setup is shown in Fig. 4.1(c). We used a homemade Ti:Sapphire laser amplifier system producing 35 fs pulses in Fourier transform-limited (FTL) condition, with a pulse energy of 600 μJ at a repetition rate of 1 kHz delivered in a beam with 3 mm diameter. A prism-dispersion-compensated Ti:Sapphire oscillator delivered sub 10 fs pulses of about 3 nJ at a 100 MHz repetition rate. Then, it was stretched by a grating pair and frequency down-converted to 1 kHz by a Pockels cell. Down-converted pulses were directed to a eight-path amplifier pumped with 15 mJ of energy from a diode-pumped frequency-doubled Nd:YLF laser. The amplified pulses were pulse-shaped with an actively controlled acousto-optic programmable dispersive filter (AOPDF) and compressed with a grating pair. The AOPDF generated independently-shaped three pulse sequence from each pulse of 1 kHz pulse train. Inter-pulse delays τ_1 and τ_2 , the time interval between the first and the second pulses, and between the second and third pulses, respectively, were varied from zero to 1638 fs with 26 fs steps to perform 2D-FTOS. The wavelength of each pulses was centered at 800 nm with bandwidth of 26 nm (FWHM) which covered both D_1 and D_2 transitions of Rb. After the three-pulse generation, each pulse had energy of 4 μJ . Therefore, the maximum intensity, I_o , of one pulse is $I_o = 2.28 \times 10^8 \text{W}/\text{cm}^2$, and $E_o = 1.75 \times 10^7$ V/m. After the three pulses were applied, the spectrally filtered (3 nm bandwidth at 780nm) fluorescence $S(\tau_1, \tau_2)$ was recorded using a photomultiplier tube. The fluorescence were collected in two-lens imaging geometry to acquire the signal from the stabilized intensity region of the electric field and to eliminate the undesired scattered photons from the input pulses.

The three pulses were shaped as follows. The first pulse was hole-shaped at 780 nm corresponds to the D_2 transition of Rb to excite only the $5P_{3/2}$ state without the $5P_{1/2}$ state. The pulse-shaping parameters for the second pulse, the control pulse of the inter-excited state transition, are chosen depending on specific coherent control experiments. There are three kinds of experiments: coherent transient mimicking, control of transition order, and quantum interference engineering. For the first experiment, the second pulse was phase-shaped in terms of linear chirp, a_2 , and quadratic chirp, a_3 . a_2 and a_3 of the second pulse are varied from -3000fs^2 to 3000fs^2 with a 500fs^2 step and from -50000fs^3 to 70000fs^3 with a 20000fs^3 step. In this experiment, the number of total waveforms including the inter-pulse delays was 372,736. The coherent transient mimicking experiment is illustrated in Sec. 5.3 in detail. The second experiment demonstrates the ability of switching the coupling between the excited states. For this, the second pulse was linearly chirped in spectral domain as $E = A(\omega) \exp[i\frac{a_2}{2}(\omega - \omega_0)^2]$ and the linear chirp coefficient a_2 was varied in the range of $[-3, 3] \times 10^3 \text{fs}^2$ with a 500fs^2 step. By changing the sign of the

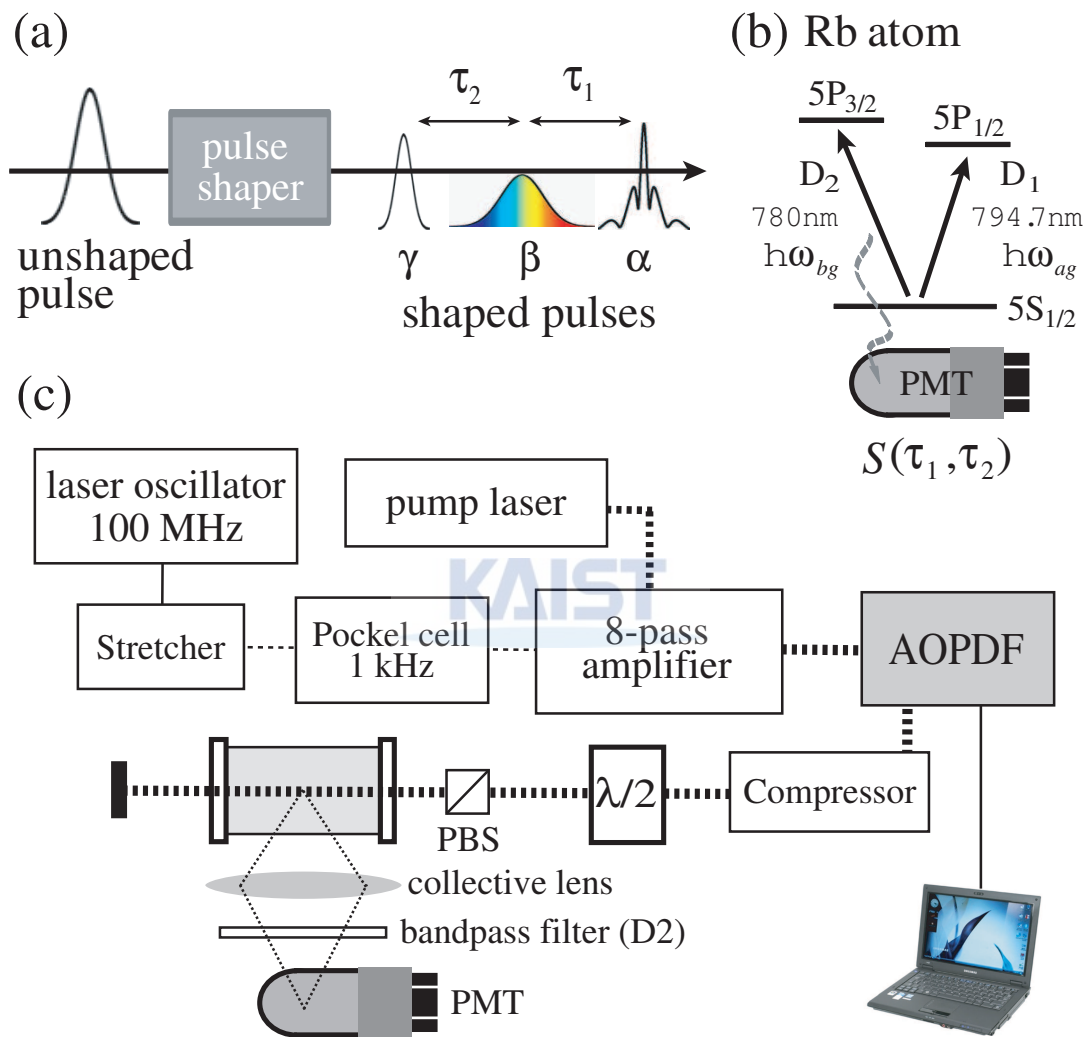


Figure 4.1: (a) Schematic representation of the experimental setup. (b) Pulse shaping scheme. The first pulse had a spectral hole around D_2 transition and the second pulse was pulse-shaped in various methods correspond to experimental purposes. The shaped pulse sequence was applied to gaseous Rb and the spectrally filtered fluorescence signal was detected with a PMT. [49]

linear chirp, the time order of D_1 and D_2 transitions was controlled because the photon energy of the pulse was linearly sorted in time depending on the value of the linear chirp. Detailed descriptions are given in Sec. 5.2. The final experiment aims to demonstrate the quantum interference engineering in a V -type system. The second pulse was either amplitude-shaped with a low-pass filter to eliminate the destructive interference, or phase-shaped by altering the phase of the spectral region $[\omega_{ag}, \omega_{bg}]$ to make constructive interference. This experiment is described in Sec. 5.3. The third pulse is maintained as a FTL pulse.

4.2 Controlled preparation of quantum systems

Foremost, we consider the first pulse in 2D-FTOS, which prepares the coherence of the quantum system. In the experiment, the first pulse, α , was shaped to have a spectral hole around the D_2 transition at 780.0 nm. By doing so, $|g\rangle \rightarrow |b\rangle$ transition is not initiated, which reduces the number of unused spectral peaks of $S(\omega_1, \omega_2)$. The other pulses were unchanged. After the three pulses were applied to Rb, the fluorescence spectrally filtered at 780 nm (3 nm bandwidth) was recorded using a photomultiplier tube.

Figures 4.2 (a) and (b) show a typical 2D-FTOS measurement, without a hole in the first pulse, of $P_a(\tau_1, \tau_2) + P_b(\tau_1, \tau_2)$ and its Fourier spectrum $S(\omega_1, \omega_2)$ respectively. The first and second pulses excited the ground state atom to first $|a\rangle$ and then to $|b\rangle$, i.e. $|g\rangle \rightarrow |a\rangle \rightarrow |b\rangle$. This transition was coherently mixed with the third pulse excitation $|g\rangle \rightarrow |b\rangle$. The quantum interference of these two transition paths was measured in the FT spectra as

$$S(\omega_{ag} - \omega_0, \omega_{bg} - \omega_0) = c_{ag}^{(1)*}(\alpha) c_{ba}^{(2)*}(\beta) c_{bg}^{(1)}(\gamma), \quad (4.1)$$

as described in Sec. 3.3. The off-diagonal peak, marked by the white arrow in Fig. 4.2(b), represents the controlled transition $c_{ba}^{(2)}$, aside from the constant one-photon transitions. Therefore, the controlled transition from $|a\rangle$ to $|b\rangle$ is well separated from the others in the 2D FT spectra.

Figures 4.2 (c) and (d) show correspondingly the measured $P_b(\tau_1, \tau_2)$ (without $P_a(\tau_1, \tau_2)$) and its Fourier spectrum for comparison with Figs. 4.2 (a) and (b). Since the primary slow oscillation component decayed from $|a\rangle$ was eliminated by the interference filter, Fig. 4.2 (c) ($P_b(\tau_1, \tau_2)$) should be filled with a speckled pattern. However, due to the spectral hole around the D_2 transition of the first pulse, the coherence between $|g\rangle$ and $|b\rangle$ was annihilated during the delay τ_1 and the slow oscillation dominates the signal along τ_1 axis. Consequently, the higher frequency components of $S(\omega_1, \omega_2)$ in Fig. 4.2 (d) were almost wiped out and the $(\omega_{ag} - \omega_0, \omega_{bg} - \omega_0)$ peak was emphasized. In this way, the unwanted higher-order transitions affecting $(\omega_{ag} - \omega_0, \omega_{bg} - \omega_0)$ peak and the background noises were greatly suppressed.

4.3 Coherent control of inter-excited state transition

In this section, we describe the experimental demonstration of coherent control of transitions between the two excited states in a V -type system. By shaping the second pulse of the three laser pulses used in 2D-FTOS, we selectively turn on and off the $5P_{1/2}$ - $5P_{3/2}$ transition of Rb. Furthermore considering the quantum interference of possible transition paths analytically, the target transition is engineered tripled relative to the FTL pulse case.

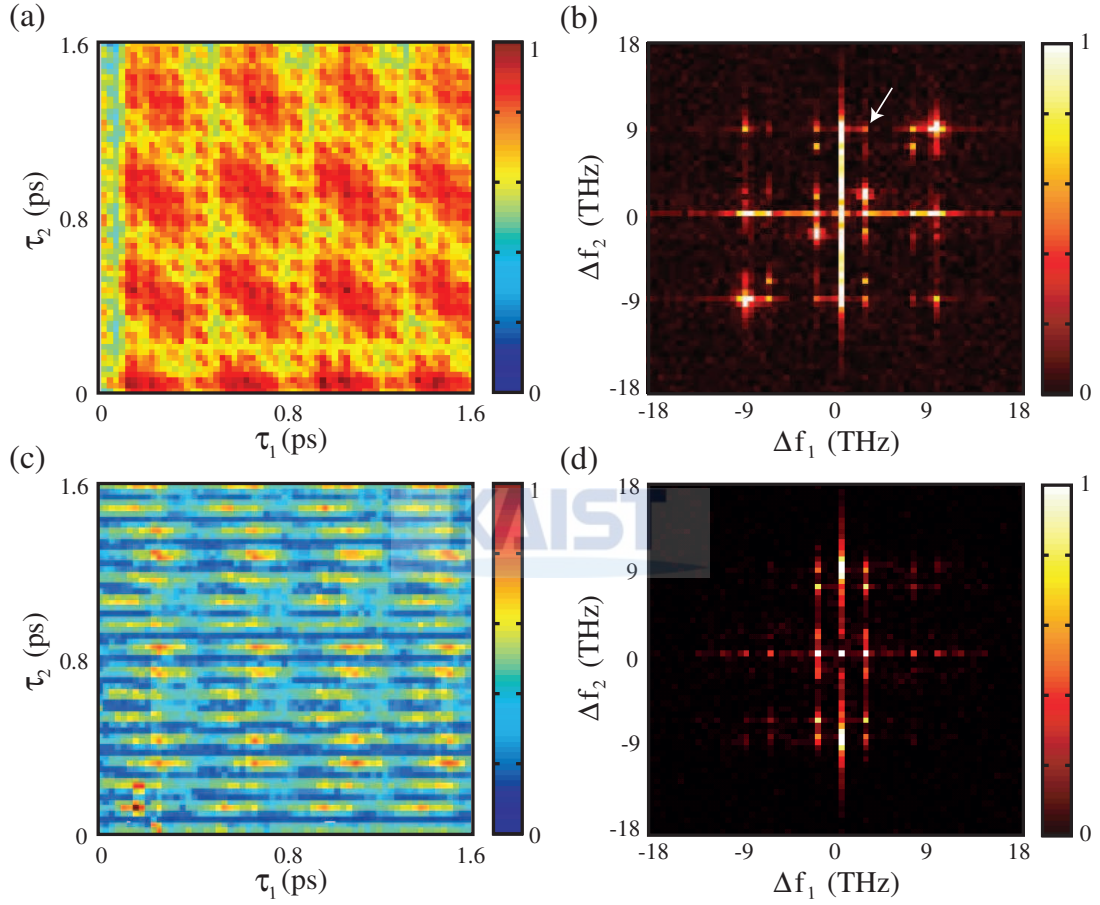


Figure 4.2: (a) Experimental fluorescence data of 2D-FTOS measurement given as a function of two time delays, τ_1 and τ_2 . (b) 2D Fourier-transformed spectrum $S(\omega_1, \omega_2)$ obtained from the time domain data (a). (c) Fluorescence signal decayed from $|b\rangle$ for the three pulses described in the text. (d) 2D Fourier spectrum of (c).

The switching experiment of the coupling strength between the excited states is given in Sec. 4.3.1, which uses a spectral phase function of linear chirp. The quantum interference engineering experiments of both the amplitude and phase shaping are described in Sec. 4.3.2.

4.3.1 Control of transition order

As the first experiment of coherent control of transition probability amplitude in a V -type system, we demonstrate selective turn-on and turn-off of the target transition from $|a\rangle$ to $|b\rangle$. For this, we applied a *linear spectral phase* to the control pulse (the second pulse). The sequence of temporally and spectrally designed ultrafast pulses was produced from an acousto-optic programmable dispersive filter as shown in Fig. 4.3(a). Each pulse was independently pulse-shaped from a single laser pulse as described in Sec. 5.1. Then, as Fig. 4.3(b) shows, a positively-chirped control pulse brought the $|a\rangle$ -state atoms, which was initially excited by the first pulse, down to the $|g\rangle$ state, and then back up to the $|b\rangle$ state. It was because the low-energy part of the spectrum arrived ahead of time compared to the high-energy part of the spectrum. On the other hand, with a negatively-chirped pulse, the spectro-temporal correlation was reversed as shown in Fig. 4.3(c). Then, with this case, the $|a\rangle$ and $|b\rangle$ states were left uncoupled. So, the chirp of the control pulse determined the strength of the $5P_{1/2} \rightarrow 5P_{3/2}$ transition.

The two-photon transition probability amplitude $c_{ba}^{(2)}$ induced by the chirped laser pulse, from the second order perturbation theory, is given by

$$c_{ba}^{(2)}(t) = -\frac{\mu_{ag}\mu_{bg}}{\hbar^2} \frac{\tau_0}{2\tau} \Delta\omega^2 \int_{-\infty}^t dt' e^{i\omega_b t'} e^{-t'^2/\tau^2} e^{-i(\omega_0 t' + 2a_2 t'^2/\tau^2 \tau_0^2)} \times \int_{-\infty}^{t'} dt'' e^{-i\omega_a t''} e^{-t''^2/\tau^2} e^{i(\omega_0 t'' + 2a_2 t''^2/\tau^2 \tau_0^2)}. \quad (4.2)$$

For this, the rotating wave approximation is used. With variable changes of $t'+t''=t_+$ and $t'-t''=t_-$ and regarding t as infinity, the full integration results to

$$c_{ba}^{(2)} = -\frac{\mu_{ag}\mu_{bg}}{\hbar^2} 2\pi E_0^2 \exp\left(-\frac{\Delta\omega_b^2 + \Delta\omega_a^2}{\Delta\omega^2}\right) \exp\left[i\frac{a_2}{2}(\Delta\omega_b^2 - \Delta\omega_a^2)\right] \times \frac{1}{2} \left(\text{Erf}\left[\frac{a_2}{2} \frac{\Delta\omega}{\sqrt{2}} (\Delta\omega_b - \Delta\omega_a) + i\frac{1}{\sqrt{2}} \left(\frac{\Delta\omega_b + \Delta\omega_a}{\Delta\omega}\right)\right] + 1 \right) = \frac{c_{bg}^{(1)} c_{ga}^{(1)}}{2} \left(\text{Erf}\left[\frac{a_2}{2} \frac{\Delta\omega}{\sqrt{2}} (\Delta\omega_b - \Delta\omega_a) + i\frac{1}{\sqrt{2}} \left(\frac{\Delta\omega_b + \Delta\omega_a}{\Delta\omega}\right)\right] + 1 \right), \quad (4.3)$$

where Erf denotes the Gauss error function, and $c_{bg}^{(1)}$ and $c_{ga}^{(1)}$ are transition probability amplitudes of the one-photon transitions $|g\rangle \rightarrow |b\rangle$ and $|a\rangle \rightarrow |g\rangle$, respectively. The error function in Eq. (4.3) approximates a sign function of a_2 for $|a_2| > 8/\Delta\omega(\omega_{bg} - \omega_{ag})$ and, therefore, the linear chirp is able to switch the $|a\rangle \rightarrow |b\rangle$ coupling. Note that, for a large positive chirp, the transition probability becomes

$$c_{ba}^{(2)} = c_{bg}^{(1)} c_{ga}^{(1)}, \quad (4.4)$$

which means the two-photon transition is de-coupled into the combination of the two one-photon transitions. We note that $|c_{bg}^{(1)} c_{ga}^{(1)}|$ becomes the absolute asymptotic value of the coherent transient mimicking experiment to be described in Sec. 5.3.

Figure 4.4 shows the Schrödinger equation calculation for the linear chirp experiment. The 2D Fourier-transformed (FT) spectra, $S(\omega_1, \omega_2)$, are shown for the linearly chirped second pulses: (a) for $a_2 = -1 \times 10^3 \text{ fs}^2$, and (b) for $1 \times 10^3 \text{ fs}^2$. The populations of $|b\rangle$ from $|a\rangle$ and directly from $|g\rangle$ are well separated in the different peak positions on the 2D spectra.

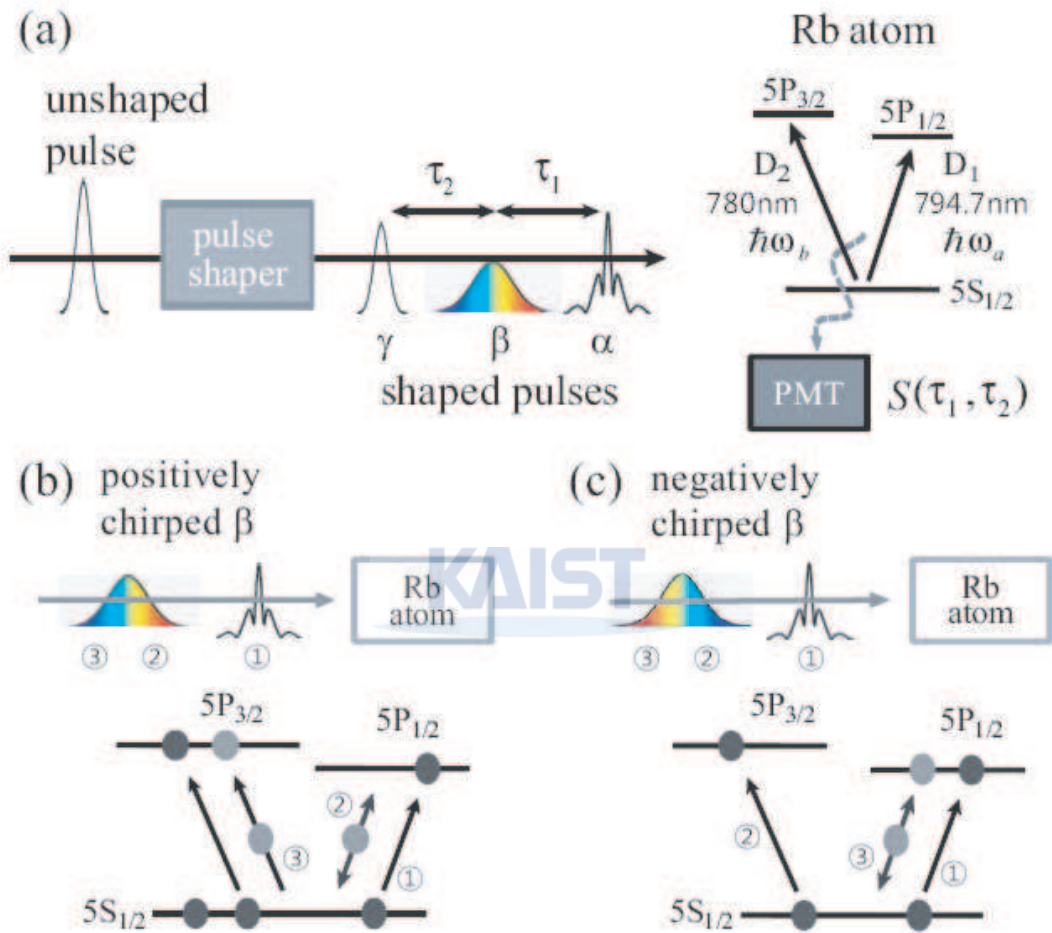


Figure 4.3: (a) Schematic diagram of the pulse shaping scenario. The first pulse has a spectral hole around D_2 transition and the second pulse is pulse-shaped to control the inter-excited state transition. The third pulse is unshaped. The three pulses are applied to gaseous Rb atom and the fluorescence signal is detected with a PMT. Depending on the chirp sign, the sequence of D_1 and D_2 transitions is time-reversed. The positive chirp case is illustrated in (b) and the negative chirp case in (c). The circled numbers indicate the transition sequence. [49]

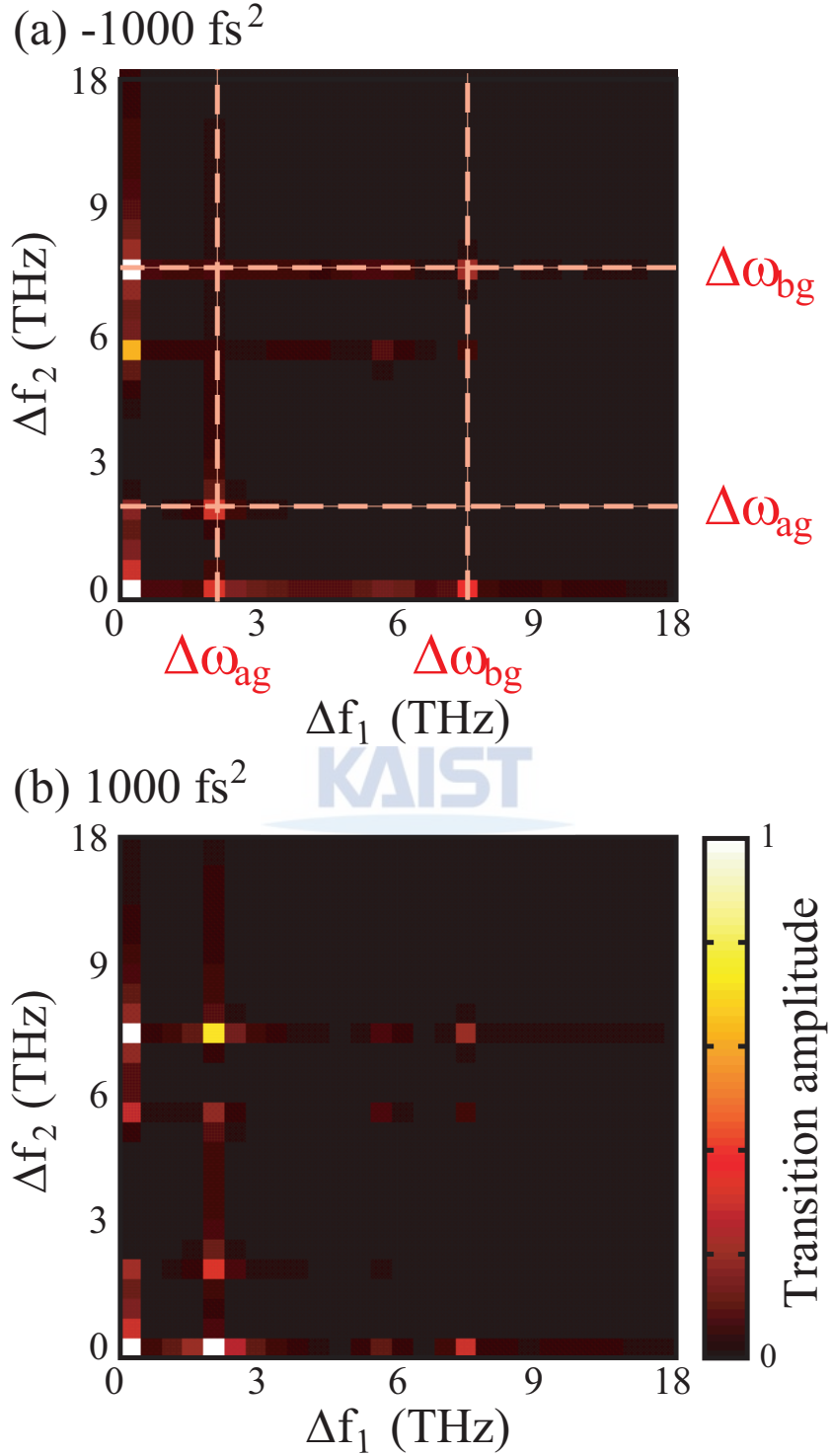


Figure 4.4: Numerical calculation results of 2D Fourier transform spectra, $S(\omega_1, \omega_2)$, for the linearly chirped second pulses of the two different chirp coefficients: (a) $-1 \times 10^3 \text{ fs}^2$, and (b) $1 \times 10^3 \text{ fs}^2$. The peak at $(\omega_{ag} - \omega_0, \omega_{bg} - \omega_0)$ denotes the the controlled transition $|a\rangle \rightarrow |b\rangle$.

Figure 4.5 shows the experimental results. The 2D Fourier transform spectra, $S(\omega_1, \omega_2)$ in Figs. 4.5(a)-(e), are shown for the various linear chirps of the second pulses. The $5P_{1/2} \rightarrow 5P_{3/2}$ transition is measured in the FT spectra given by

$$S(\omega_{ag} - \omega_0, \omega_{bg} - \omega_0) = c_{ag}^{(1)*}(\alpha)c_{ba}^{(2)*}(\beta)c_{bg}^{(1)}(\gamma), \quad (4.5)$$

where $c_{ag}^{(1)}$ and $c_{bg}^{(1)}$ are the one-photon transitions due to the first and the third pulses, respectively, and $*$ denotes complex conjugate. The off-diagonal peaks marked by the white arrows represent the target $|a\rangle \rightarrow |b\rangle$ transition. The measured transition probability amplitudes are shown in Fig. 4.5 (f) in comparison to the numerical simulation based on Eq. (4.3) for linear chirps $[-3, 3] \times 10^3 \text{fs}^2$ with 500 fs^2 steps. The suppression of $5P_{1/2} \rightarrow 5P_{3/2}$ coupling is clearly shown for the negatively chirped pulses and the enhancement for the positively chirped pulses. So, the chirp control of the $5P_{1/2} \rightarrow 5P_{3/2}$ transition is successfully demonstrated. We note that the spectral hole around D_2 transition was used in the first pulse to selectively allow those couplings initiated from $5P_{1/2}$, as a result, in this experiment, the peaks at $(\omega_{bg} - \omega_0, \omega_{bg} - \omega_0)$ and $(\omega_{bg} - \omega_0, \omega_{ag} - \omega_0)$ appeared almost wiped-out. Alternatively, when the second pulse was prepared with a spectral hole around D_1 line, then the coupling $(\omega_{bg} - \omega_0, \omega_{ag} - \omega_0)$ was enhanced by a negatively chirped pulse, meaning that the temporal sequence for the same $5P_{1/2}$ - $5P_{3/2}$ coupling was reversed.

The intuitive ordering of frequencies in the pulse for the effective transfer is that firstly the atoms are driven from the $5P_{1/2}$ to the $5S_{1/2}$ state (resonant at 794.7 nm) with the red frequency components and then from the $5S_{1/2}$ to the $5P_{3/2}$ state (resonant at 780 nm) with the blue components. And the experimental and numerical results together with analytic derivations are proved the scenario. On the other hand, in contrast to measurements of population transfer with two separated pulses making single-photon excitation each, the counterintuitive ordering of frequencies (as in STIRAP) is not effective in our situation. This contrast motivates us to examine the underlying dynamics in more detail.

Figures 4.6 (d)-(f) show the calculated populations of the $5S_{1/2}$ (blue line), $5P_{1/2}$ (dashed line), and $5S_{3/2}$ (red line) states and the field envelope (solid black line) as a function of time for the linear chirp values of (d) -1000 fs^2 , (e) zero, and (f) -1000 fs^2 respectively. For this calculation, we used a pulse energy of about five times more than that of the second pulse used in the experiment to make the transition clearly visible. Note that, the behavior was unchanged with smaller energy calculation. To consider the transition from $5P_{1/2}$ state to $5P_{3/2}$ state, the initial population is fixed as $(5S_{1/2}, 5P_{1/2}, 5P_{3/2})=(0,1,0)$.

For a positive chirp, the pulse starts red detuned in time and $5S_{1/2}$ - $5P_{1/2}$ transition frequency comes earlier than $5S_{1/2}$ - $5P_{3/2}$ transition frequency. As one can see in Fig. 4.6(f), the positive chirp pulse drives population from $5P_{1/2}$ to $5S_{1/2}$ at the time interval when the laser frequency meets the $5S_{1/2}$ - $5P_{1/2}$ transition frequency. Then as the frequency of the pulse sweeps to the blue which is resonant for the $5S_{1/2}$ - $5P_{3/2}$ transition, population is transferred to the $5P_{3/2}$ state resulting in efficient coupling between the $5P_{1/2}$ and $5P_{3/2}$ states.

However, the opposite chirp, shown in Fig. 4.6 (d), yields a different behavior. The pulse frequency starts at resonance frequency of $5S_{1/2}$ - $5P_{3/2}$ transition and can efficiently drive population of $5S_{1/2}$ state to $5P_{3/2}$ state, at about -72.7 fs in our condition, but there is no population in $5S_{1/2}$ state so no significant population transfer occurs at this time. And then, $5S_{1/2}$ - $5P_{1/2}$ transition frequency component comes to Rb atom, at about -18.9 fs in our condition, the pulse transfers population to the $5P_{1/2}$ state rapidly, but is far detuned from the $5S_{1/2}$ - $5P_{3/2}$ transition frequency. Therefore, there is ineffective transfer to the $5P_{3/2}$ state. 2D Fourier transformed spectra are shown in Figs. 4.6(a)-(c) in contour map representation.

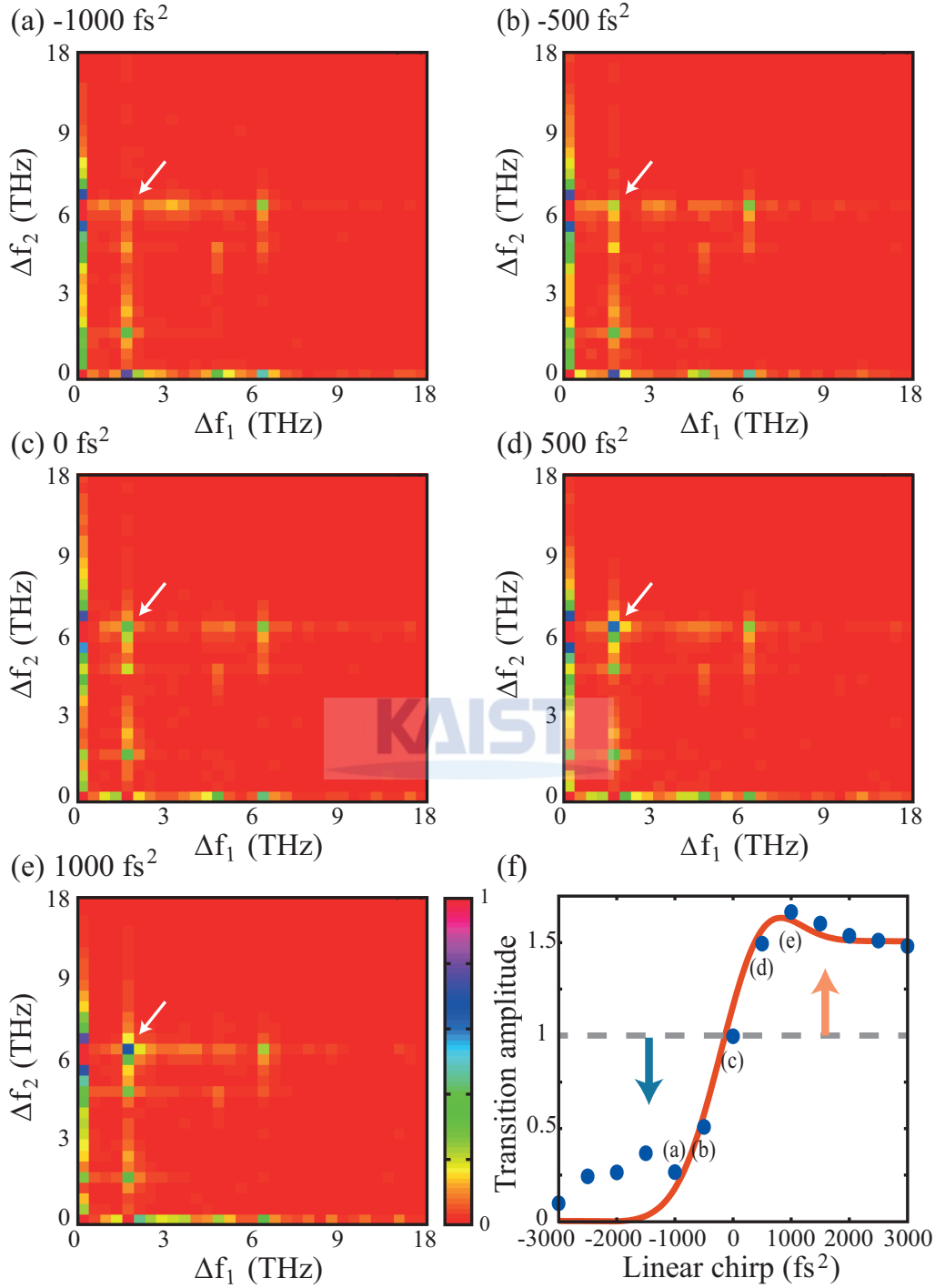


Figure 4.5: Experimental results of 2D FT spectra $S(\omega_1, \omega_2)$ for shaped pulses with the five different chirp coefficients: (a) $-1 \times 10^3 \text{ fs}^2$, (b) $-5 \times 10^2 \text{ fs}^2$, (c) zero, (d) $5 \times 10^2 \text{ fs}^2$, and (e) $1 \times 10^3 \text{ fs}^2$. The peaks at $(\omega_{ag} - \omega_0, \omega_{bg} - \omega_0)$ are marked by white arrows which represent the target two-photon process, $5P_{1/2} \rightarrow 5P_{3/2}$. (f) Extracted peak amplitudes at $(\omega_{ag} - \omega_0, \omega_{bg} - \omega_0)$ plotted as a function of chirp of the second pulses (circles) are compared with the numerical calculation of $c_{ba}^{(2)}$ (line).

4.3.2 Quantum interference engineering

In the previous section, the enhancement of the transition is clearly observed, resulting from the interference between the resonant and nonresonant pathways. Next, we aim for further enhancement by applying a general phase function to the control pulse. We start by considering the two-photon transition probability amplitude written in spectral domain given as

$$c_{ba}^{(2)} = \frac{\mu_{ga}\mu_{gb}}{\hbar^2} [-\pi E^*(\omega_{ag})E(\omega_{bg}) - i\wp \int_{-\infty}^{\infty} d\omega \frac{E^*(\omega)E(\omega_{ba} + \omega)}{\omega_{ag} - \omega}], \quad (4.6)$$

where μ_{nm} is a dipole moment matrix element, $E(\omega)$ the inverse Fourier transform of the electric field, and \wp the Cauchy principal value. For a laser pulse having the spectral components all in phase, the resonant contribution is real (the first term in Eq. (4.6)), and the two nonresonant contributions (the second term) below and above the resonance frequency ω_{ag} are both imaginary but out of phase with respect to each other. Hence, the three components, the resonant part, and the upper and lower nonresonant parts, add up to the total transition, $c_{ba}^{(2)}$, and $c_{ba}^{(2)}$ can be enhanced by engineering the interference among them. By encoding a constant phase ϕ_b over a block spectral region $[\omega_{ag}, \omega_{ag} + \omega_{ba}]$, the interference of the three transition components of the dominant spectral region can be altered. The transition probability amplitude c_{ba} in Eq. (4.6) can be disassembled as

$$c_{ba}^{(2)} = i \frac{\mu_{ga}\mu_{gb}}{\hbar^2} [i\pi E^*(\omega_{ag})E(\omega_{bg}) - e^{i\phi_b} \int_{\omega_{ag}-\omega_{ba}}^{\omega_{ag}} \frac{E^*(\omega)E(\omega_{ba} + \omega)}{|\omega_{ag} - \omega|} d\omega + e^{-i\phi_b} \int_{\omega_{ag}}^{\omega_{ag}+\omega_{ba}} \frac{E^*(\omega)E(\omega_{ba} + \omega)}{|\omega_{ag} - \omega|} d\omega], \quad (4.7)$$

where the first, second, and third terms correspond to A , B , and C in phase diagram in the upper-left inset of Fig. 4.7(a). In our experiment, the ratio of the transition amplitude absolutes is given by $|A| : |B| : |C| = 1 : 2.8 : 1.6$. Fig. 4.7 (a) shows the measured net transition probability amplitudes as a function of ϕ_b . The dots are experimental results and the black dashed line is the theoretical calculation based on Eq. (4.6). The spectral phase function was smeared by 0.2 nm in the experiment and such consideration (shown with the solid line) more accurately fits the experimental results. Two local maxima are expected from Eq. (4.7), one at $\phi_b = \pi/2$ and the other at $\phi_b = 3\pi/2$. As shown in Figs. 4.7 (b-d), the three transition components A , B , and C , interfere either constructively or destructively with each other while B and C rotate relative to A in opposite directions as depicted in the upper-left inset. For example in Fig. 4.7 (d), the three components become all in phase allowing the maximum quantum interference tripling the transition probability amplitude.

Alternatively, spectral amplitude shaping of the control pulse can be employed to enhance the given two-photon transition. For example, among the components in Eq. (4.7), the smaller nonresonant transition component C can be removed. For this, the nonresonant component of the transition probability amplitude (the second term of Eq. (4.6)) can be rephrased as

$$c_{ba}^{(2)nr} = \frac{\mu_{ga}\mu_{gb}}{i\hbar^2} \left[\int_{\infty}^{\omega_{bg}} \frac{E^*(\omega - \omega_{ba})E(\omega)}{|\omega_{bg} - \omega|} d\omega - \int_{\omega_{bg}}^{\omega_{cut}} \frac{E^*(\omega - \omega_{ba})E(\omega)}{|\omega_{bg} - \omega|} d\omega \right], \quad (4.8)$$

where the spectrum below ω_{cut} is eliminated (the second term in Eq. (4.6)) as depicted in the inset of Fig. 4.8. In the final experiment, we utilized the spectral amplitude block above the cutoff frequency

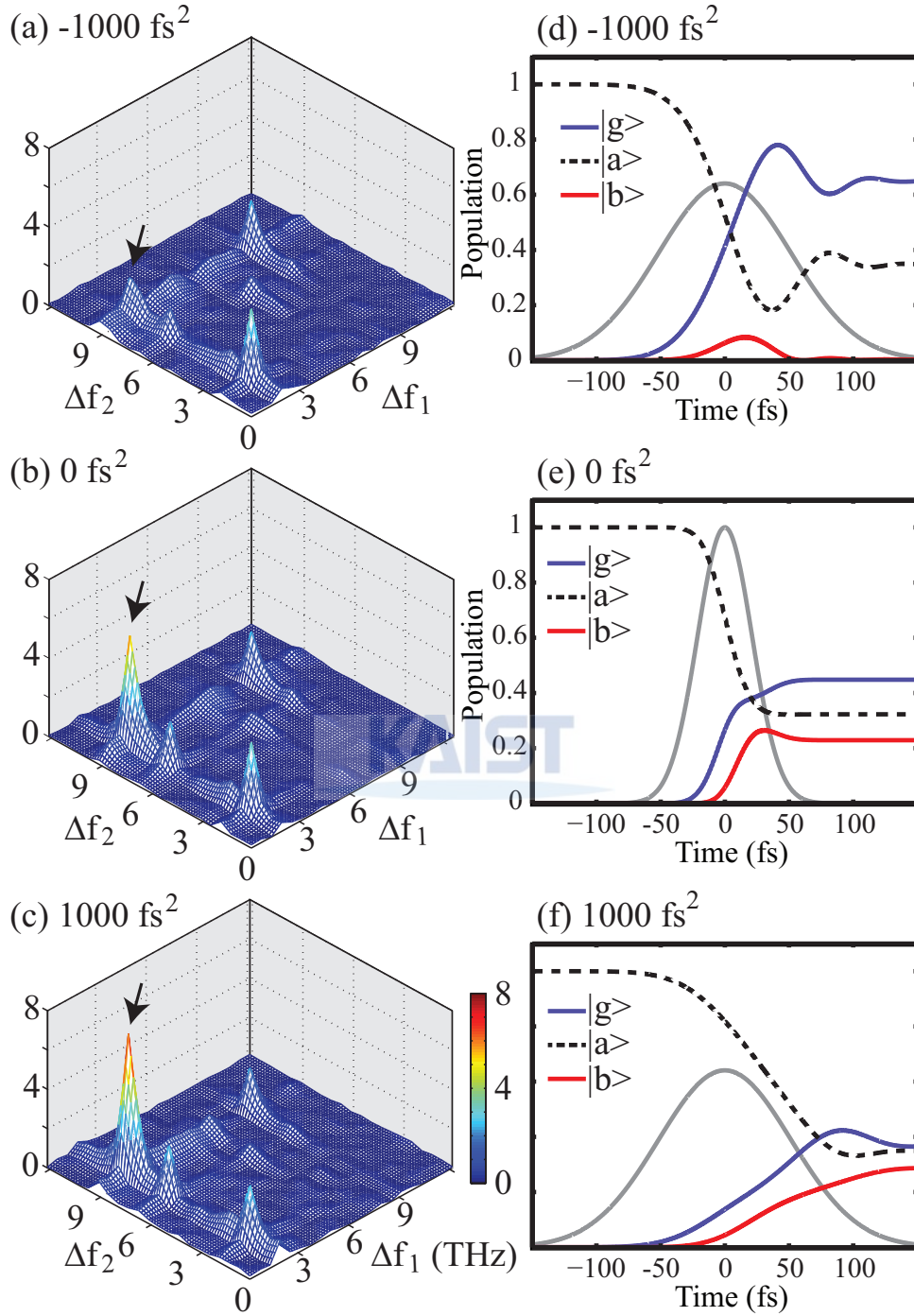


Figure 4.6: (a)-(c) Experimental results of 2D Fourier transformed spectra $S(\omega_1, \omega_2)$ in contour map representation for linear chirp values of (a) -1000 fs^2 , (b) zero, and (c) 1000 fs^2 . The peaks $(\omega_{ag} - \omega_0, \omega_{bg} - \omega_0)$ are marked by black arrows. (d)-(f) The $5S_{1/2}$ (blue line), $5P_{1/2}$ (dashed line), and $5S_{3/2}$ (red line) populations, as well as the field envelope (solid black line), corresponding to (a), (b), and (c) respectively.

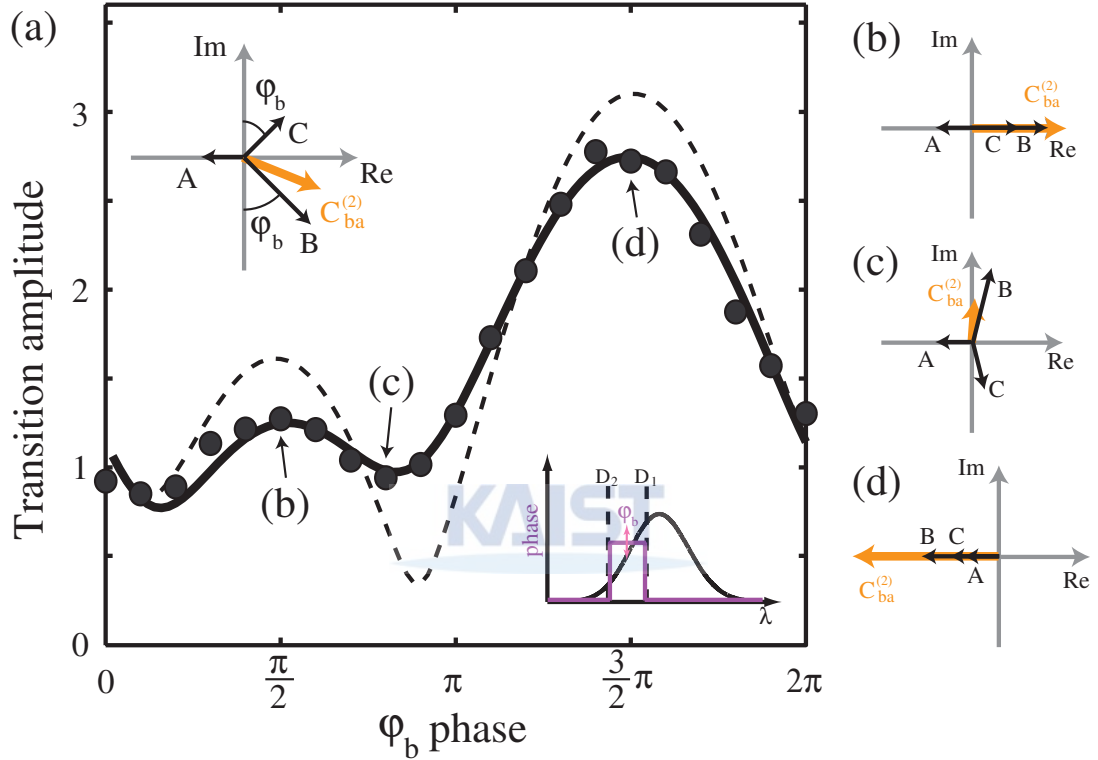


Figure 4.7: (a) Experimental and theoretical results for the quantum interference engineering. Dots: measured transition amplitude absolutes, dashed line: numerical calculation based on Eq. (4.6), solid line: numerical calculation considering the spectrally smeared phase (see the text). Insets: (upper-left) the phase diagram for the three transition components in Eq. (4.7), (lower-right) the laser spectrum with block spectral phase, where the block spectral phase ϕ_b represents the relative phase of the spectral region in $[\omega_{ag}, \omega_{bg}]$ with respect to the other. (b-d) The phase diagrams for the maximal (b,d) and the minimal (c) quantum interference conditions. [49]

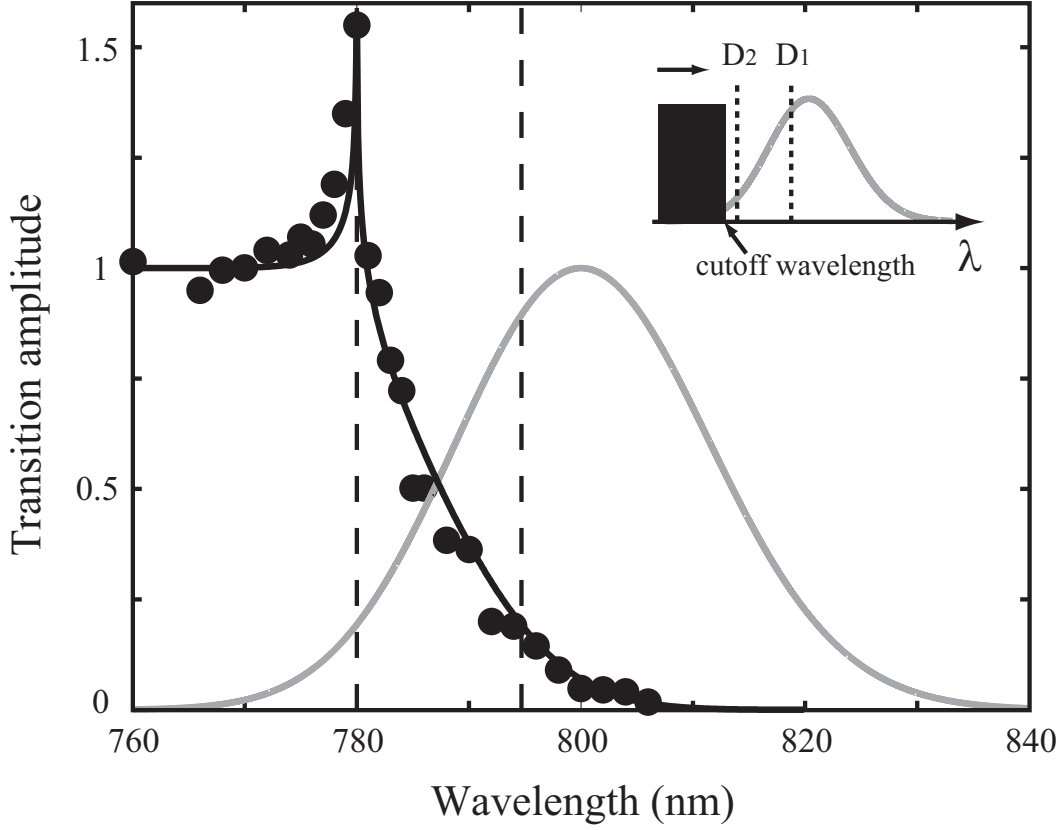


Figure 4.8: Coherent enhancement experiment of the $5P_{1/2} \rightarrow 5P_{3/2}$ transition of Rb by spectral amplitude shaping. The measured transition probability amplitudes, normalized to the full spectrum limit (dots), are plotted along with the calculated data (dark line) as a function of the cutoff wavelength. The laser spectrum is shown in gray line. The inset illustrates the spectral shape used in the experiment. The dashed lines are the D_1 and D_2 resonant wavelengths. [49]

(ω_{cut}) into the second pulse (the spectral phase is unchanged.) The tested transition probability amplitudes $c_{ba}^{(2)}$ were retrieved from the 2D spectra, $S(\omega_1, \omega_2)$, as a function of ω_{cut} . The experimental result is shown in dots in Fig. 4.8, and the theoretical results in black solid line is calculated using Eq. (4.6). The normalized laser spectrum is shown in gray solid line and the resonance wavelengths are denoted by black dashed lines in Fig. 4.8. As the cutoff wavelength λ_{cut} approaches the resonance wavelength λ_{bg} from the short-wavelength end, the second term of $c_{ba}^{(2)nr}$, or C in Eq. (4.7), becomes smaller and, therefore, the target inter-excited state transition is enhanced. The two-photon transition $c_{ba}^{(2)}$ is maximally enhanced, for $\lambda_{cut} = \lambda_{bg}$, by 60% compared to the full spectrum limit.

Chapter 5. Coherent transients in a V -type three-level system

In this chapter, we show theoretically and experimentally that the two-photon inter-excited state transition in a V -type three-level system projects one-photon coherent transients (CTs) in a two-level system. For this, we use two kinds of pulse shape parameters: linear chirp and quadratic chirp. In a V -type system we show that the transition between inter-excited state can be reduced to the transition in a two-level system. As a result of interaction with the linearly and quadratically phase-shaped pulses, the final probability amplitude of the target excited state in a V -type system can be interpreted in terms of conventional CTs in a two-level system. Here, CTs in a two-level system refer to the time evolution of the probability amplitude, of the excited state interacted with a linearly chirped pulse, which shows an oscillatory behavior as a function of time.

As a brief review of CTs, we consider one-photon transition in a two-level system of ground state $|1\rangle$ and excited state $|2\rangle$. For an optical short pulse of gaussian pulse shape with linear chirp, the electric field $E(t)$ is given by

$$E(t) = \mathcal{E}_o \exp \left[-\frac{t^2}{\tau_c^2} - i(\omega_0 t + \alpha t^2) \right], \quad (5.1)$$

where $\tau_c = \tau_o \sqrt{1 + a_2^2/\tau_o^4}$, $\alpha = 2a_2/(\tau_o^4 + 4a_2^2)$, and τ_o is the unchirped pulse duration. Then the excitation probability amplitude c_{21} at a finite time t is given in the weak-field regime as [45]

$$c_{21}(t) = \frac{i\mu_{21}\mathcal{E}_o}{\hbar} \int_{t_0}^t \exp\left(-\frac{t'^2}{\tau_c^2}\right) \exp[-i((\omega_0 - \omega_{21})t' + \alpha t'^2)] dt', \quad (5.2)$$

where the time t and the linear chirp rate a_2 are the two control parameters for the quadratic and cubic phase terms, respectively, and the finite time integration with a quadratic temporal phase $\alpha t'^2$ leads to the transient excited-state population being of a Cornu spiral shape, well known from Fresnel diffraction pattern from a sharp edge [94]. For a short pulse which has broad spectral components, putting chirp on the pulse delays some of those components with respect to others in the time domain, and the instantaneous laser frequency shifts as a function of time. So, from the time when the resonant condition is met, further off-resonant excitation interferes, with the resonant transition, either constructively or destructively. In the frequency domain representation, Eq. (5.2) is given by

$$c_{21}(t) = \frac{\mu_{21}}{\hbar} \left[i\pi E(\omega_{21}) + \wp \int_{-\infty}^{\infty} \frac{E(\omega) \exp[i(\omega_{21} - \omega)t]}{\omega_{21} - \omega} d\omega \right], \quad (5.3)$$

where $E(\omega) = E_o \exp[-(\omega - \omega_0)^2 \tau_o^2/4 + i\phi(\omega)]$ and \wp is the Cauchy principal value [47]. So, the quantum interference between the resonant and non-resonant excitation contributions shows an oscillatory transient behavior for a given chirped pulse. CTs have demonstrated many novel phenomena, including the time-domain Fresnel lens [46], Coherent transient enhancements [47], quantum state holographic measurements [48], and coherent controls of multi-state ladders [95].

This chapter is organized as following. Derivation of the transition probability amplitudes in a ladder-type system is reviewed in Sec. 5.1, in comparison to the transitions in a V -type system. There exist a number of studies performed with ladder-type systems interacting with linearly chirped pulses

(chirp parameter a_2), the oscillatory motions of the transition found as a function of a_2 have not been clearly explained. In Sec. 5.2, the one-photon transition probability amplitude in a two-level system is given in comparison with the inter-excited state transition in a V -type system. The experimental demonstration of CTs in a V -type system is given in Sec. 5.3.

5.1 Transitions in a ladder system

In this section, we derive the transition probability amplitude in a ladder type system which comprises one ground state $|g\rangle$, one resonant intermediate state $|i\rangle$, and one excited state $|e\rangle$. Both the energy differences between $|i\rangle$ and $|g\rangle$, and $|e\rangle$ and $|i\rangle$ are resonant with the laser pulse spectrum. The target state $|e\rangle$ is excited via two-photon absorption process from $|g\rangle$. In the weak field regime, the major contribution to the transition is two-photon absorption process. Therefore, by assuming the pulse duration considerably shorter than all lifetimes involved, the transition probability amplitude can be derived from the second order perturbation theory as

$$\begin{aligned}
c_{ni}^{(2)}(t) &= \left(\frac{-i}{\hbar}\right)^2 \sum_m \int_{t_0}^t dt' \int_{t_0}^{t'} dt'' e^{i\omega_{nm}t'} V_{nm}(t') e^{i\omega_{mi}t''} V_{mi}(t'') \\
&= -\frac{\mu_{fi}\mu_{ig}}{\hbar^2} \int_{t_0}^t dt' \int_{t_0}^{t'} dt'' e^{i\omega_{fi}t'} E(t') e^{i\omega_{ig}t''} E(t'') \\
&= -\frac{\mu_{fi}\mu_{ig}}{2\pi\hbar^2} \int_{t_0}^t dt' \int_{t_0}^{t'} dt'' e^{i\omega_{fi}t'} \left[\int_{-\infty}^{\infty} d\omega_1 e^{-i\omega_1 t'} E(\omega_1) \right] e^{i\omega_{ig}t''} \left[\int_{-\infty}^{\infty} d\omega_2 e^{-i\omega_2 t''} E(\omega_2) \right] \\
&= -\frac{\mu_{fi}\mu_{ig}}{2\pi\hbar^2} \int_{-\infty}^{\infty} d\omega_1 E(\omega_1) \int_{-\infty}^{\infty} d\omega_2 E(\omega_2) \int_{t_0}^t dt' e^{i(\omega_{fi}-\omega_1)t'} \int_{t_0}^{t'} dt'' e^{i(\omega_{ig}-\omega_2)t''} \\
&= -\frac{\mu_{fi}\mu_{ig}}{2\pi\hbar^2} \int_{-\infty}^{\infty} d\omega_1 E(\omega_1) \int_{-\infty}^{\infty} d\omega_2 E(\omega_2) \int_{t_0}^t dt' e^{i(\omega_{fi}-\omega_1)t'} \frac{e^{i(\omega_{ig}-\omega_2)t'} - e^{i(\omega_{ig}-\omega_2)t_0}}{i(\omega_{ig}-\omega_2)} \\
&= -\frac{\mu_{fi}\mu_{ig}}{2\pi\hbar^2} \int_{-\infty}^{\infty} d\omega_1 E(\omega_1) \int_{-\infty}^{\infty} d\omega_2 E(\omega_2) \\
&\quad \times \left[\frac{e^{i(\omega_{fi}-\omega_1+\omega_{ig}-\omega_2)t} - e^{i(\omega_{fi}-\omega_1+\omega_{ig}-\omega_2)t_0}}{i(\omega_{ig}-\omega_2)i(\omega_{fi}-\omega_1+\omega_{ig}-\omega_2)} - \frac{e^{i(\omega_{fi}-\omega_1)t} - e^{i(\omega_{fi}-\omega_1)t_0}}{i(\omega_{ig}-\omega_2)i(\omega_{fi}-\omega_1)} e^{i(\omega_{ig}-\omega_2)t_0} \right].
\end{aligned} \tag{5.4}$$

Here, t and t_0 satisfy the condition, $|t| > T$ and $t > 0$, $|t_0| > T$ and $t_0 < 0$ for large enough T . With these conditions and also using the Residue Theorem, Eq. (5.4) becomes

$$c_{ni}^{(2)} = i \frac{\mu_{fi}\mu_{ig}}{\hbar^2} \left[i\pi E(\omega_{ig})E(\omega_{fi}) + \wp \int d\omega \frac{E(\omega)E(\omega_{fg}-\omega)}{\omega_{ig}-\omega} \right], \tag{5.5}$$

where \wp is the principal value of Cauchy, and ω_{ig} , $\omega_{fg} - \omega_{ig} = \omega_{fi}$ are the resonance frequencies. The first term depends only on the spectral components of the pulse at the resonance frequencies, whereas the second term integrates over the contributions of all other spectral components of the pulse. The first term (the on-resonance contribution) is shifted by $\pi/2$ compared with the second term (the off-resonance contributions). Also, the spectral components below and above the resonance excite the system π out of phase.

The critical difference between Eq. (3.27) in a V -type system and Eq. (5.5) in a ladder-type system, is the existence of the complex conjugate term. Due to the downward transition or de-excitation process, $|a\rangle \rightarrow |g\rangle$, in the V -type system, the negative frequency component of the electric field is involved, which therefore appears in Eq. (3.27) as a complex conjugate term. Let us consider the spectral phase

function of the pulse, for example, a general phase function of Taylor expansion series, $\phi(\omega) = a_2/2(\omega - \omega_0)^2 + a_3/6(\omega - \omega_0)^3 + \dots$. Then, in the V -type system, the overall phase of the term $E^*(\omega_{ag})E(\omega_{bg})$, for example, results from the difference between the two spectral phases of the resonance frequencies. Therefore, the total phase of the transition is converted as the spectral phase function of the electric field is differentiated. On the other hand, in a ladder system, the overall phase results from the summation of them and can not be of a simpler form. The differentiated phase in the V -type system is an essential feature useful to mimic the CTs of a two-level system, and the following section describes about the relation in detail.

5.2 Coherent transients in a two-level system

In this section, we derive transition probability amplitude formula of one-photon transition in a two-level system comprises a ground state $|1\rangle$, and an excited state $|2\rangle$. And then, we show the striking similarities between the derived formula and the case of the two-photon inter-excited state transition in a V -type system.

In a two-level system, one-photon transition probability amplitude can be calculated using the first order perturbation theory. For the excitation case, the transition from the ground state $|1\rangle$ to the excited state $|2\rangle$, the amplitude is given as

$$\begin{aligned} c_{21}^{(1)}(t) &= \frac{-i}{\hbar} \int_{t_0}^t dt' \langle n | V_I(t') | i \rangle \\ &= \frac{i\mu_{21}}{\hbar} \int_{t_0}^t dt' e^{i\omega_{21}t'} E(t'). \end{aligned} \quad (5.6)$$

If we consider the electric field as a gaussian pulse with a linear chirp, i.e.,

$$E(\omega) = E_o \exp\left(-\frac{(\omega - \omega_0)^2}{\Delta\omega^2} + i\frac{a_2}{2}(\omega - \omega_0)^2\right) \quad (5.7)$$

then, electric field, $E(t)$, derived in previous Sec. 3.1, is given by

$$E(t) = \frac{E_o}{\sqrt{2}} \sqrt{\frac{\tau_o}{\tau_c}} \Delta\omega \exp\left[\frac{i}{2} \tan^{-1}\left(\frac{2a_2}{\tau_o^2}\right)\right] \exp\left(-\frac{t^2}{\tau_c^2} - i\left[\omega_0 t + \frac{2a_2}{\tau_o^4 + 4a_2^2} t^2\right]\right).$$

Substituting $E(t)$ in Eq. (5.6), the transition probability amplitude is written as a function of time and linear chirp by

$$\begin{aligned} c_{21}^{(1)}(t, a_2) &= \frac{i\mu_{21}}{\hbar} \frac{E_o}{\sqrt{2}} \sqrt{\frac{\tau_o}{\tau_c}} \Delta\omega \exp\left[\frac{i}{2} \tan^{-1}\left(\frac{2a_2}{\tau_o^2}\right)\right] \\ &\quad \times \int_{t_0}^t dt' \exp\left(-\frac{t'^2}{\tau_c^2} + i\left[(\omega_{21} - \omega_0)t' - \frac{2a_2}{\tau_o^4 + 4a_2^2} t'^2\right]\right), \end{aligned} \quad (5.8)$$

where $\tau_0 = \frac{2}{\Delta\omega}$ and $\tau_c = \tau_0 \sqrt{1 + \left(\frac{a_2}{\tau_o^2}\right)^2}$. Alternatively, we can derive the transition probability amplitude in frequency domain by the same method used in the two-photon cases (sections 3.2 and 5.1) as

$$c_{21}^{(1)}(t) = \frac{\mu_{21}}{\hbar} \left[i\pi E(\omega_{21}) + \wp \int_{-\infty}^{\infty} \frac{E(\omega) \exp(i(\omega_{21} - \omega)t)}{\omega_{21} - \omega} \right] \quad (5.9)$$

$$\begin{aligned} &= \frac{\mu_{21}}{\hbar} \exp(i(\omega_{21} - \omega_0)t) \\ &\quad \times \left[i\pi E(\omega_{21}) \exp(-i(\omega_{21} - \omega_0)t) + \wp \int_{-\infty}^{\infty} \frac{E(\omega) \exp(-i(\omega - \omega_0)t)}{\omega_{21} - \omega} \right] \end{aligned} \quad (5.10)$$

Note that, Eq. (5.9) has the same structure with that of inter-excited state transition in a V -type system except the positive sign between resonant and nonresonant parts.

If we consider the de-excitation case, the transition probability amplitude, from $|2\rangle$ to $|1\rangle$, is derived as

$$c_{12}^{(1)}(t) = \frac{\mu_{21}}{\hbar} \left[i\pi E^*(\omega_{21}) - \wp \int_{-\infty}^{\infty} \frac{E^*(\omega) \exp(i(\omega_{21} - \omega)t)}{\omega_{21} - \omega} \right] \quad (5.11)$$

$$= \frac{\mu_{21}}{\hbar} \exp(-i(\omega_{21} - \omega_0)t) \times \left[i\pi E^*(\omega_{21}) \exp(i(\omega_{21} - \omega_0)t) - \wp \int_{-\infty}^{\infty} \frac{E^*(\omega) \exp(i(\omega - \omega_0)t)}{\omega_{21} - \omega} \right], \quad (5.12)$$

which has minus sign between resonant and nonresonant parts. For a linearly chirped pulse, Eq. (5.12) is written by

$$c_{12}^{(1)}(t, a_2) = \frac{\mu_{21}}{\hbar} \exp(-i(\omega_{21} - \omega_0)t) \left[i\pi A(\omega_{21}) \exp\left(i[(\omega_{21} - \omega_0)t - \frac{a_2}{2}(\omega_{21} - \omega_0)^2]\right) - \wp \int_{-\infty}^{\infty} \frac{A(\omega) \exp\left(i[(\omega - \omega_0)t - \frac{a_2}{2}(\omega - \omega_0)^2]\right)}{\omega_{21} - \omega} \right]. \quad (5.13)$$

Now, we further develop the formula of the inter-excited state transition in a V -type system. We can obtain a simpler form of Eq. (3.27) for a gaussian pulse spectrally centered at ω_0 , i.e., $A(\omega) = E_0 \exp[-(\omega - \omega_0)^2/\Delta\omega^2]$, with the general Taylor expansion spectral phase, $\phi(\omega)$, given by

$$\phi(\omega) = a_1(\omega - \omega_0) + \frac{a_2}{2}(\omega - \omega_0)^2 + \frac{a_3}{6}(\omega - \omega_0)^3 + \dots \quad (5.14)$$

With conventional analytic calculation, Eq. (3.27) becomes

$$c_{ba}^{(2)} = i \frac{\tilde{\mu}_{ba}}{\hbar^2} \left[i\pi \tilde{\mathbb{E}}(\bar{\omega}) - \wp \int_{-\infty}^{\infty} \frac{\tilde{\mathbb{E}}(\omega)}{\bar{\omega} - \omega} d\omega \right], \quad (5.15)$$

where $\tilde{\mu}_{ba} = \mu_{ga}\mu_{bg} \exp[-\omega_{ba}^2/2\Delta\omega^2 + ia_3\omega_{ba}^3/24]$, $\bar{\omega} = (\omega_{ag} + \omega_{bg})/2$, and

$$\tilde{\mathbb{E}}(\omega) = E_0^2 \exp\left[-2\frac{(\omega - \omega_0)^2}{\Delta\omega^2} + i\omega_{ba} \frac{d\phi}{d\omega}\right]. \quad (5.16)$$

It is noted that Eq. (5.15) is of a functional form strikingly similar to Eq. (5.11), the one-photon transition in a two-level system. Also, for a pulse having spectral phase function of linear and quadratic chirps, Eq. (5.15) can be written as

$$c_{ba}^{(2)}(a_2, a_3) = i \frac{\mu_{bg}\mu_{ga}}{\hbar^2} \exp\left(-\frac{\omega_{ba}^2}{2\Delta\omega_0^2} + i\frac{a_3}{24}\omega_{ba}^3\right) \times \left[i\pi \exp\left(-2\frac{(\frac{\omega_{bg} + \omega_{ag}}{2} - \omega_0)^2}{\Delta\omega_0^2} + i\left[a_2\omega_{ba}\left(\frac{\omega_{bg} + \omega_{ag}}{2} - \omega_0\right) + \frac{a_3}{2}\omega_{ba}\left(\frac{\omega_{bg} + \omega_{ag}}{2} - \omega_0\right)^2\right]\right) - \wp \int d\omega \frac{\exp\left(-2\frac{(\omega - \omega_0)^2}{\Delta\omega_0^2} + i\left[a_2\omega_{ba}(\omega - \omega_0) + \frac{a_3}{2}\omega_{ba}(\omega - \omega_0)^2\right]\right)}{\frac{\omega_{bg} + \omega_{ag}}{2} - \omega} \right] \quad (5.17)$$

$$= i \frac{\tilde{\mu}_{ba}}{\hbar^2} \left[i\pi \mathbb{A}(\bar{\omega}) \exp\left(i\left[a_2\omega_{ba}(\bar{\omega} - \omega_0) + \frac{a_3\omega_{ba}}{2}(\bar{\omega} - \omega_0)^2\right]\right) - \wp \int_{-\infty}^{\infty} \frac{\mathbb{A}(\omega) \exp\left(i\left[a_2\omega_{ba}(\omega - \omega_0) + \frac{a_3\omega_{ba}}{2}(\omega - \omega_0)^2\right]\right)}{\bar{\omega} - \omega} d\omega \right]. \quad (5.18)$$

As evident from the same structure, the two-photon inter-excited states transition in a V -type system projects one-photon transition (de-excitation) in a simple two-level system. Tantalizing part is that, since $\tilde{\mathbb{E}}(\omega)$ has differentiated phase, linear chirp in V -type system corresponds to time in two-level

system, and minus quadratic chirp to linear chirp. So, the obtained solution in Eq. (5.15), which is the transition probability amplitude $c_{ba}^{(2)}$ for the two-photon inter-excited state transition in a V -type system, has become formally a one-photon transition probability amplitude, more specifically a de-excitation process, in a two-level system of energies 0 and $\bar{\omega}$, induced by the newly defined electric field $\tilde{\mathbb{E}}(\omega)$.

Therefore, if we consider the interaction of the V -type system with a shaped pulse of linear and quadratic chirps, then we can achieve duplicated results of Coherent transients in a two-level system interacting with a linearly chirped pulse. With this information, we can derive the "transient" excitation probability amplitude, a similar form to Eq. (5.2), for the V -type system. For this, the electric field $\mathbb{E}(t)$ is the inverse Fourier transformation of the complex conjugate of electric field in frequency domain $\tilde{\mathbb{E}}(\omega)$ given by

$$\begin{aligned}
\mathbb{E}(t) &= \frac{E_o^2}{\sqrt{2\pi}} \int_{-\infty}^{\infty} d\omega \exp\left(-\frac{(\omega - \omega_0)^2}{\Delta\omega'^2} - i[-(\omega - \omega_0)\omega_{ba}a_2 - (\omega - \omega_0)^2\frac{\omega_{ba}a_3}{2}]\right) \exp(i\omega t) \\
&= \frac{E_o^2}{\sqrt{2\pi}} \exp(i\omega_0 t) \int_{-\infty}^{\infty} d\omega \exp\left(-\frac{\omega^2(1 - i\frac{\omega_{ba}a_3}{2}\Delta\omega'^2) - i\Delta\omega'^2(t + \omega_{ba}a_2)\omega}{\Delta\omega'^2}\right) \\
&= \frac{E_o^2}{\sqrt{2\pi}} \exp(i\omega_0 t) \exp\left(-\frac{(t + \omega_{ba}a_2)^2\Delta\omega'^2}{4(1 - i\frac{\omega_{ba}a_3}{2}\Delta\omega'^2)}\right) \int_{-\infty}^{\infty} d\omega \exp\left(-\frac{(1 - i\frac{a_3}{2}\Delta\omega'^2)(\omega - \frac{i\Delta\omega'^2(t + \omega_{ba}a_2)}{2(1 - i\frac{\omega_{ba}a_3}{2}\Delta\omega'^2)})^2}{\Delta\omega'^2}\right) \\
&= \frac{E_o^2}{\sqrt{2\pi}} \exp\left(-\frac{t^2}{\tau_c^2} + i\left[\omega_0 t - \frac{2\omega_{ba}a_3}{\tau_o^4 + 4\omega_{ba}^2 a_3^2}(t + \omega_{ba}a_2)^2\right]\right) \sqrt{\frac{\pi}{\frac{1 - i\frac{\omega_{ba}a_3}{2}\Delta\omega'^2}{\Delta\omega'^2}}} \\
&= \frac{E_o^2}{\sqrt{2}} \sqrt{\frac{\tau_o}{\tau_c}} \Delta\omega' \exp\left[\frac{i}{2} \tan^{-1}\left(\frac{2\omega_{ba}a_3}{\tau_o^2}\right)\right] \exp\left(-\frac{(t + \omega_{ba}a_2)^2}{\tau_c^2} + i\left[\omega_0 t - \frac{2\omega_{ba}a_3}{\tau_o^4 + 4\omega_{ba}^2 a_3^2}(t + \omega_{ba}a_2)^2\right]\right), \tag{5.19}
\end{aligned}$$

where $\Delta\omega'$ is the reduced spectral bandwidth, $\Delta\omega/\sqrt{2}$. Substituting linear and quadratic chirps to reduced time and linear chirp, $\tilde{t} = \omega_{ba}a_2$ and $\tilde{a}_2 = -\omega_{ba}a_3$, and fix the time to $t = 0$, reduced electric field is written as

$$\mathbb{E}(t) = \frac{E_o^2}{\sqrt{2}} \sqrt{\frac{\tau_o}{\tau_c}} \Delta\omega' \exp\left[-\frac{i}{2} \tan^{-1}\left(\frac{2\tilde{a}_2}{\tau_o^2}\right)\right] \exp\left(-\frac{\tilde{t}^2}{\tau_c^2} + i\left[\omega_0 t + \frac{2\tilde{a}_2}{\tau_o^4 + 4\tilde{a}_2^2}\tilde{t}^2\right]\right). \tag{5.20}$$

Then, the "CT-like" transition probability amplitude in a V -type system is obtained as

$$c_{ba}^{(2)}(a_2, a_3) = -\frac{\tilde{\mu}_{ba}E_o^2 e^{i\theta}}{\hbar^2} \frac{\Delta\omega}{\sqrt{\tilde{\tau}_c/\tilde{\tau}_o}} \int_{-\infty}^{\tilde{t}} \exp(-\frac{t'^2}{\tilde{\tau}_c^2}) \exp[-i((\omega_{ba} - \omega_0)t' - \tilde{\alpha}t'^2)] dt', \tag{5.21}$$

where $\theta = -\frac{1}{2} \tan^{-1} 2\tilde{a}_2/\tilde{\tau}_o^2 + (\bar{\omega} - \omega_0)\tilde{t}$, $\tilde{\tau}_o = 2\sqrt{2}/\Delta\omega$, $\tilde{\tau}_c = \tilde{\tau}_o\sqrt{1 + \tilde{a}_2^2/\tilde{\tau}_o^4}$, and $\tilde{\alpha} = 2\tilde{a}_2/(\tilde{\tau}_o^4 + 4\tilde{a}_2^2)$.

5.3 Coherent transients mimicked in atomic rubidium

We verify experimentally that coherent transient phenomena are mimicked in a V -type system. For the experiment, briefly to summarize, we used the lowest three energy levels of Rb. To generate broadband femtosecond pulses, we used a homemade Ti:Sapphire laser amplifier system. Each pulse was separated into three pulses to perform 2D-FTOS. In the meantime, three pulses were independently pulse-shaped to apply advanced coherent controlled 2D-FTOS technique.

Now, let us go back to the transition probability amplitude of the two-photon transition in the V -type system, $c_{ba}^{(2)}$. Considering a general phase function $\phi(\omega)$ for the pulse with linear and quadratic

chirps together, i.e.,

$$\phi(\omega) = \frac{a_2}{2}(\omega - \omega_0)^2 + \frac{a_3}{6}(\omega - \omega_0)^3. \quad (5.22)$$

$c_{ba}^{(2)}$ was represented in Sec. 3.2 as

$$c_{ba}^{(2)} = i \frac{\mu_{bg} \mu_{ga}}{\hbar^2} \left[i\pi E^*(\omega_{ag}) E(\omega_{bg}) - \wp \int d\omega \frac{E^*(\omega) E(\omega_{ba} + \omega)}{\omega_{ag} - \omega} \right]. \quad (5.23)$$

The first term of Eq. (5.23) only depends on the spectral components of the pulse at the resonance frequencies, whereas the second term integrates over the contributions of all the other spectral components of the pulse. Therefore, the absolute value of the resonant part is not affected by the change of the phase $\phi(\omega)$ of the pulse, as depicted in Fig. 5.1(a). However, the non-resonant part is changed drastically with $\phi(\omega)$ as shown in Fig. 5.1(b). And as a result of the interference between the resonant and nonresonant parts, total transition probability amplitude becomes as shown in Fig. 5.2 (a).

Also, we have shown in Sec. 5.2 that the two-photon process in a V -type system can be reduced to a one-photon de-excitation in a two-level system. The result in Eq. (5.15) is a reminiscence of femtosecond coherent transient (CT) experiments by Girard and co-workers [45, 46, 48]. Therefore, the linear and quadratic chirp coefficients a_2 and a_3 in Eq. (5.22) play the same roles of time and linear chirp, respectively, in a perturbative chirped pulse excitation. (See, for example, Eq. (1) in Ref. [46].) Therefore, the transition amplitude is given as

$$c_{21}^{(2)} \propto \int_{-\infty}^{\hat{t}} dt_1 \exp\left(-\frac{t_1^2}{\tau_c^2}\right) \exp\left[-i \frac{(t_1 + T_0)^2 - T_0^2}{2\hat{a}_2}\right], \quad (5.24)$$

where $\hat{t} = \omega_{ba} a_2$, $\hat{a}_2 = -\omega_{ba} a_3$, and $T_0 = (\bar{\omega} - \omega_0) \hat{a}_2$ [48]. The approximation holds when $\tau_0 \ll |2\hat{a}_2|$.

To verify the ‘‘CT-like behavior’’ of the two-photon inter-excited states transition in a V -type system, experiments were performed with the second pulses with linear and quadratic chirps, as shown in Fig. 5.2. The surface plot in Fig. 5.2(a) shows the absolutes of the numerical calculation of $5P_{1/2}$ - $5P_{3/2}$ transition probability in Eq. (5.15). Transition probability amplitudes were calculated from $a_2 = [-9, 9] \times 10^3$ fs² and $a_3 = [-15, 15] \times 10^4$ fs³ with step size of 1×10^2 fs² for a_2 and 5×10^3 fs³ for a_3 . The boxed region in Fig. 5.2(a) was tested with the spectral phase function $\phi(\omega)$ in Eq. (5.22). The second pulse was programmed with various chirp coefficients that were sampled from $a_2 = [-3, 3] \times 10^3$ fs² and $a_3 = [-5, 7] \times 10^4$ fs³ with step size of 5×10^2 fs² for a_2 and 2×10^4 fs³ for a_3 . The result is shown in Fig. 5.2(b). The results are linearly interpolated twice from 13×7 measurements in use of the MATLAB’s built-in function ‘‘interp2’’. The extracted absolutes of $c_{ba}^{(2)}$ from the $(\omega_{ag} - \omega_0, \omega_{bg} - \omega_0)$ peaks in 2D FT spectra are plotted in Figs. 5.2(c)-(e) for $a_3 = -5 \times 10^4$, -1×10^4 , and 3×10^4 fs³, respectively, together with the theoretical curves calculated by Eq. (5.15). For a given quadratic chirp, the transition probability shows an oscillatory behavior as a function of the linear chirp, a typical feature of CT [45]. Note that, the experiments are carried on relatively small ranges of a_2 and a_3 . It is because the energy of the diffracted pulses from AOPDF are differed when the pulse shapes are significantly changed, and constant energy of the second pulse is required to measure the inter-excited state transition consistently. Note also that, 13×7 measurements utilized 372736 number of waveforms including the inter-pulse delays, and performed in more than four days.

Figure 5.3 illustrates the retrieval of $5P_{1/2} \rightarrow 5P_{3/2}$ transition probability amplitude from the coherently controlled 2D spectral peak. The left panel of Fig. 5.3 (sub-labeled with -I) shows $|S(\omega_{ag} - \omega_0, \omega_{bg} - \omega_0)|$, the absolute of the extracted 2D-FTOS peaks. The experimental results (circles) and the calculations (lines) are shown as a function of linear chirp, for various quadratic chirps of (a) -5×10^4 fs³,

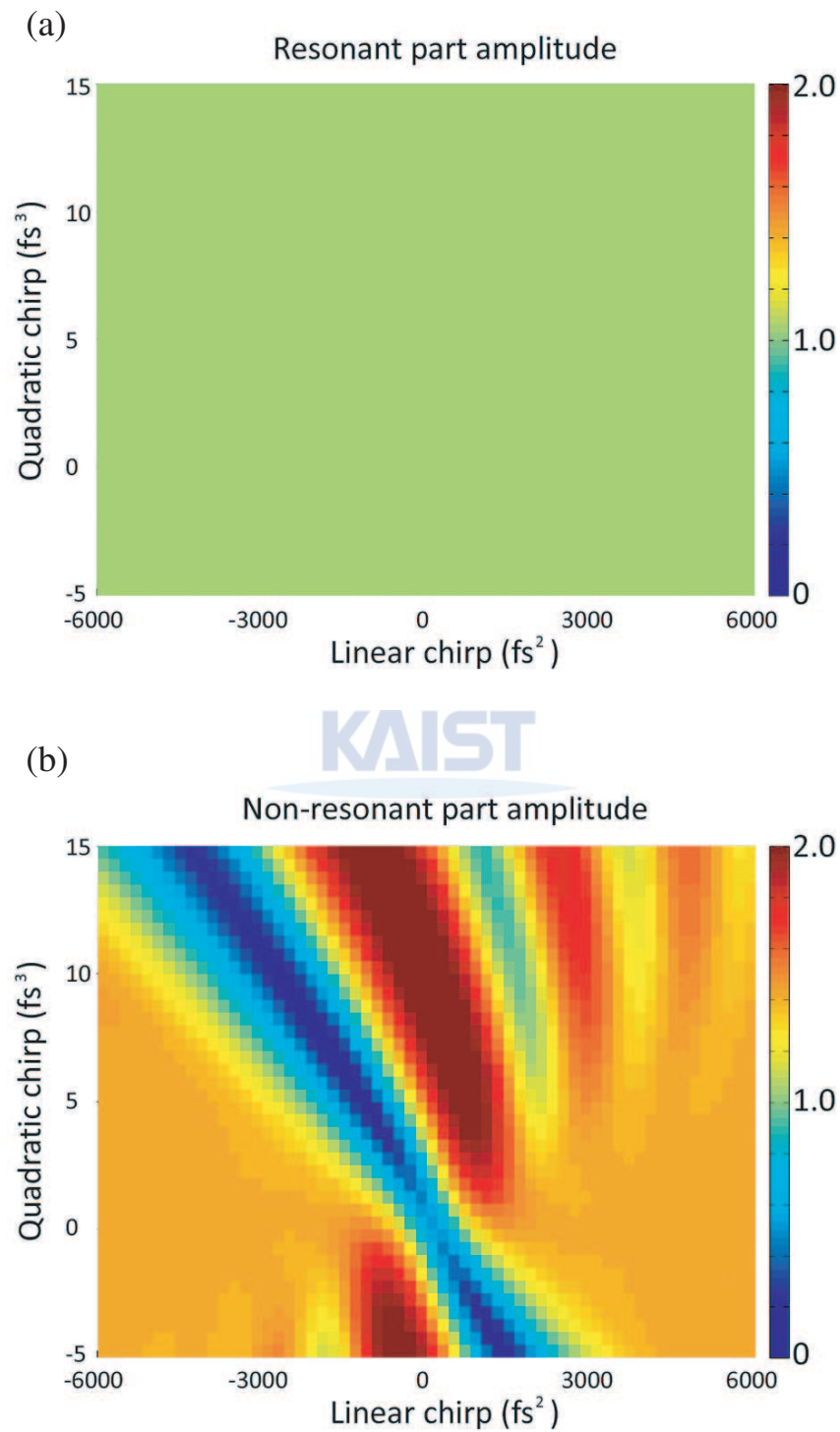


Figure 5.1: Calculated transition probability amplitude from $|a\rangle$ to $|b\rangle$ via an intermediate state $|g\rangle$ using the Eq. (5.23): (a) is the resonant part (the first term), and (b) the nonresonant part (the second term).

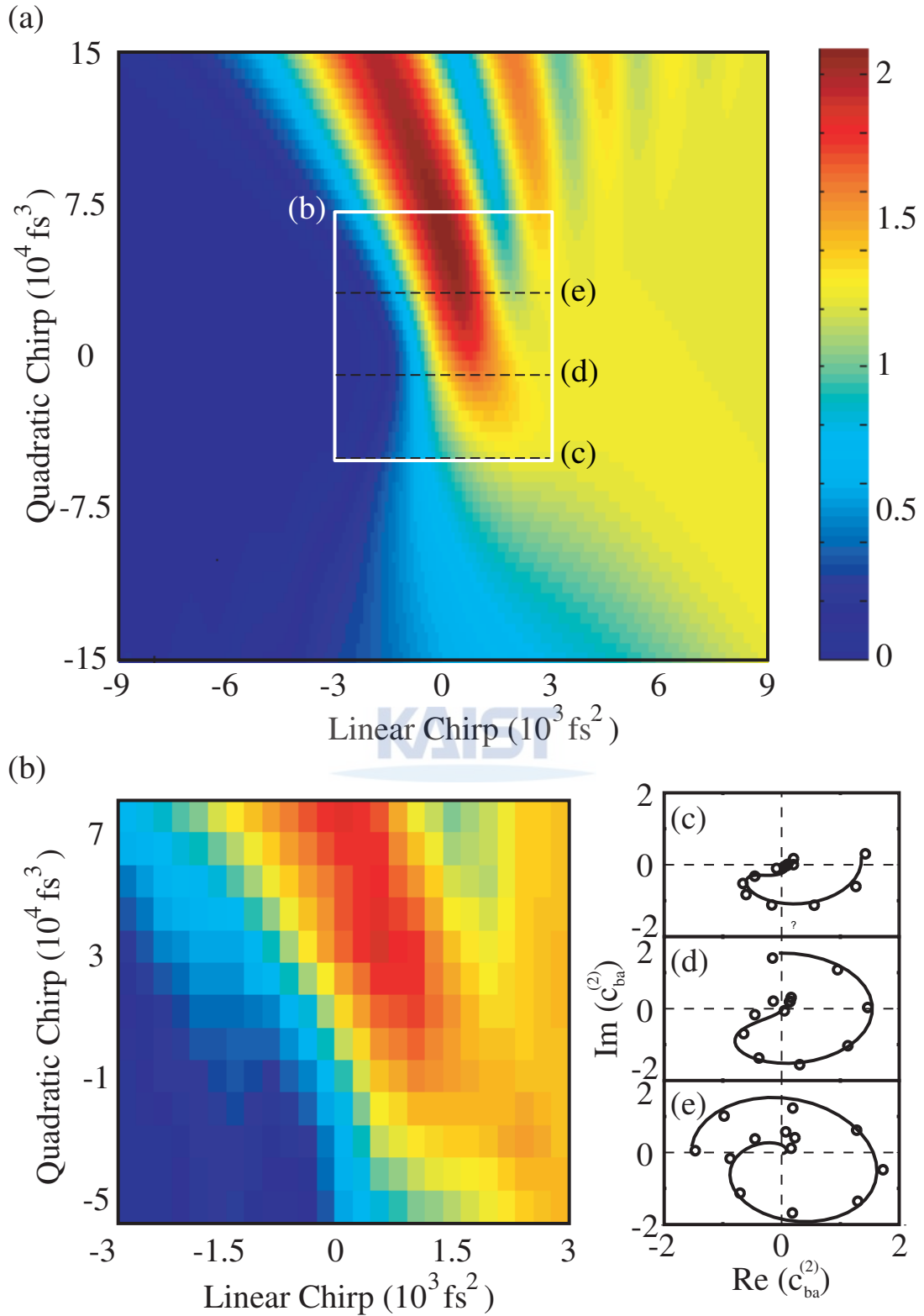


Figure 5.2: (a) Numerical calculation of $|c_{ba}^{(2)}|$ plotted as a function of linear and quadratic chirps. (b) Extracted amplitudes of $(\omega_{ag} - \omega_0, \omega_{bg} - \omega_0)$ peaks of 2D Fourier transformed spectra (experimented for the white rectangular area in (a); interpolated twice from 13×7 measurements.) (c)-(e) Two-photon transition amplitudes ($c_{ba}^{(2)}$) drawn in the complex plane as a function of linear chirp, (c) for quadratic chirp $-5 \times 10^4 \text{ fs}^3$, (d) for $-1 \times 10^4 \text{ fs}^3$, and (e) for $3 \times 10^4 \text{ fs}^3$, respectively. [60]

(b) $-3 \times 10^4 \text{ fs}^3$, (c) $-1 \times 10^4 \text{ fs}^3$, (d) $1 \times 10^4 \text{ fs}^3$, (e) $3 \times 10^4 \text{ fs}^3$, (f) $5 \times 10^4 \text{ fs}^3$, and (g) $7 \times 10^4 \text{ fs}^3$. The numerical calculations are carried on wider range of linear chirp, $a_2 = [-6, 6] \times 10^3 \text{ fs}^2$, with finer step size of 50 fs^2 , to show the overall behavior of CTs. The calculations are normalized with the transition probability amplitude at $a_2 = 6 \times 10^3 \text{ fs}^2$, $a_3 = 0$, and the experiments accordingly. The experimental results are in a good agreement with the numerical calculation, although the population of $5P_{3/2}$ state was primarily covered by the one-photon transition from the $5S_{1/2}$ state.

Finally, the phase information of $5P_{1/2} \rightarrow 5P_{3/2}$ transition probability amplitude is retrieved. As described in Sec. 3.3, the peaks represent the value of the product of three-pulse transitions given by

$$S(\omega_{ag} - \omega_0, \omega_{bg} - \omega_0) = c_{ag}^{(1)*}(\alpha) c_{ba}^{(2)*}(\beta) c_{bg}^{(1)}(\gamma), \quad (5.25)$$

and since the first and third pulses were in a FTL pulse condition, $5P_{1/2} \rightarrow 5P_{3/2}$ transition probability amplitude obtained directly from the phase of $(\omega_{ag} - \omega_0, \omega_{bg} - \omega_0)$ peaks in 2D Fourier spectrum as well as the absolutes. The central panel of Fig. 5.3 (sub-labeled with -II) represents the phase and amplitude of extracted $c_{ba}^{(2)}$ shown in complex plane representation. The values start from the origin at negative linear chirp, and spread out with rotating counter-clock wise as the linear chirp goes to positive, which can be easily predicted from Eq. (3.27). The well-known Cornu spirals of CTs [48] are reconstructed by compensating the phase difference $\phi_c = \exp(-i(\bar{\omega} - \omega_0)\omega_{ba}a_2)$, between Eq. (5.13) and Eq. (5.18). We note that the another phase $-\frac{1}{2} \tan^{-1} 2\tilde{a}_2/\tilde{\tau}_o^2$ in Eq. (5.18) is already included in \mathcal{E}_o of Eq. (5.13). The results are summarized in the right panel of Fig. 5.3 (sub-labeled with -III). The phase-compensated transition probability amplitudes, $e^{i\phi_c} c_{ba}^{(2)}$, perfectly reconstruct a Cornu spiral which starts from the origin and approaches to an asymptotic point. It is noted that the asymptotic points have the same radius from the origin for all quadratic chirps, which is equivalent to the fact that the transition probability amplitude of the two-level problem is dependent only on the resonant spectral amplitude $A(\omega_{21})$. The absolute of asymptotic points is given by

$$|c_{ba}^{(2)}| = |c_{ag}^{(1)} c_{bg}^{(1)}|, \quad (5.26)$$

which is the product of de-coupled one-photon transitions, $c_{ag}^{(1)}$ and $c_{bg}^{(1)}$, from the two-photon inter-excited states transition.

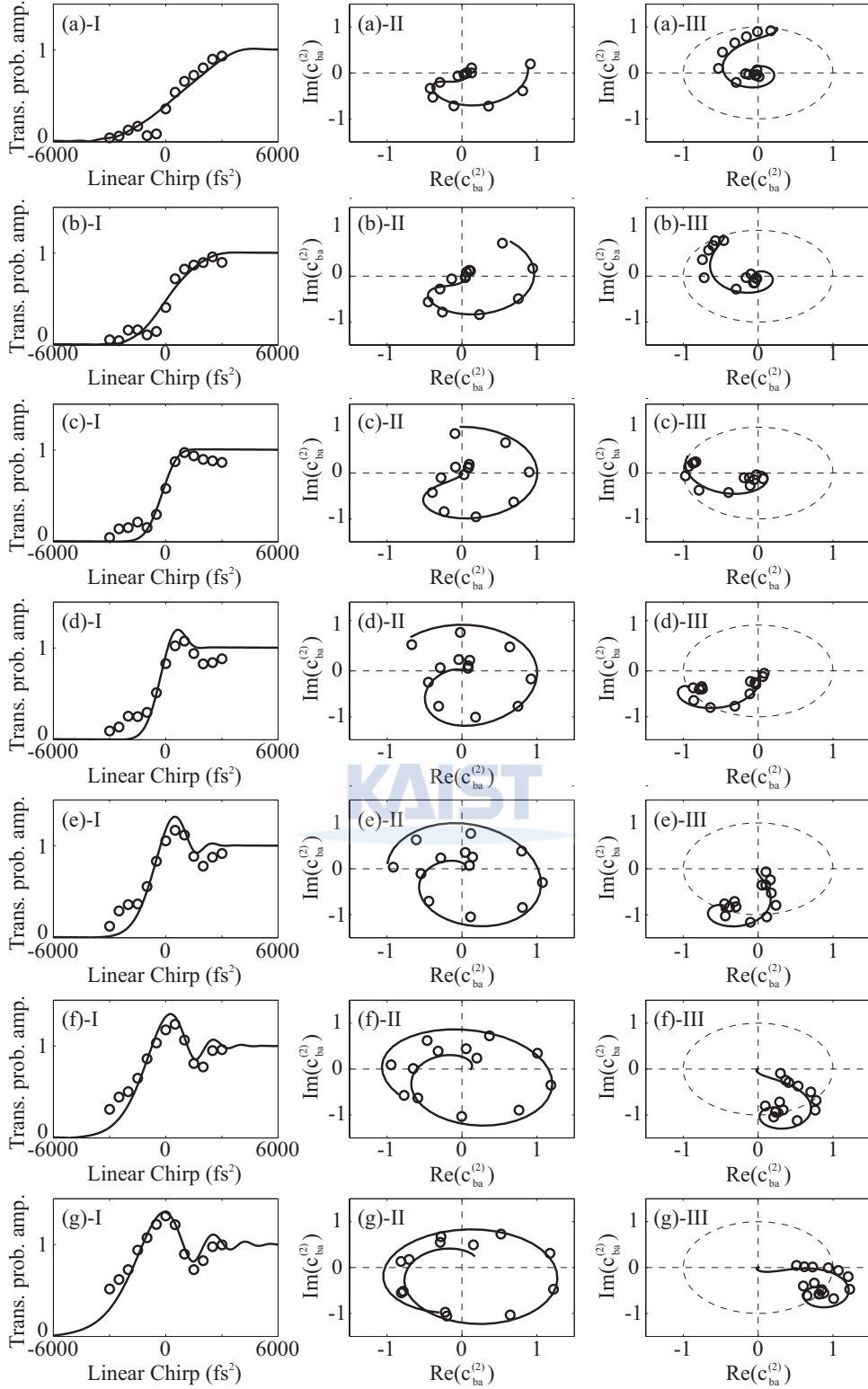


Figure 5.3: (a) Extracted transition probabilities from the experimental 2D-spectra at $(\omega_{ag}-\omega_0, \omega_{bg}-\omega_0)$ peaks (circles) together with the numerical calculations of $5P_{1/2}-5P_{3/2}$ transition (lines) as a function of linear chirp for quadratic chirp of the second pulse, (a) -5×10^4 fs³, (b) -3×10^4 fs³, (c) -1×10^4 fs³, (d) 1×10^4 fs³, (e) 3×10^4 fs³, (f) 5×10^4 fs³, and (g) 7×10^4 fs³. The left panel, sub-labeled with -I, shows the absolute value of $c_{ba}^{(2)}$, and the central panel (II) is the complex plane representation of $c_{ba}^{(2)}$. The reconstructed Cornu spirals are shown in the right panel (III) following the process explained in the context.

Chapter 6. Shaped pulse 2D-FTOS in Quantum wells

In this chapter, we propose an extended 2D-FTCCS experiment applied to semiconductor quantum well system. For this, we study the effect of density of states on exciton states in a semiconductor superlattice system [61]. Also, we consider the asymmetric double quantum well systems as a possible V -type system candidate.

This chapter contains the study of the effect on the quantum states from non-uniform density of states in Sec 6.1, and the study of the proposed asymmetric double quantum well systems in Sec 6.2.

6.1 Non-uniform continuum density of states on Fano resonance

The Fano resonance (FR) is due to quantum mechanical coupling between a discrete energy state and a degenerate energy continuum and appears in many optically measured absorption and reflection spectra as an asymmetric line-shape known as Fano shape,

$$I(\epsilon) = I_o(\epsilon) \frac{(q + \epsilon)^2}{1 + \epsilon^2}, \quad (6.1)$$

where I_o is a fictitious “background” spectrum from only the continuum state, q is the Fano shape parameter, and the reduced energy $\epsilon = 2(E - E_r)/\Gamma$ measures the energy difference from a resonance in terms of the half-width of coupling strength [62]. It is understood that the shape parameter q is a ratio between two excitation amplitudes: one for the direct transition to the modified discrete state due to the continuum, and the other for the two-step transition to the discrete state via the continuum [63]. These two quantum pathways for an optical transition, red or blue detuned from the resonant energy, results in either destructive or constructive interference.

While FR has been reported ubiquitously in a variety of quantum mechanical systems including atoms, molecules, semiconductors and even in optical resonators [64, 65, 66, 67, 68, 69, 71], a direct control of Fano coupling, thus a controllable FR, has been first performed with a semiconductor system [72]. This control experiment has a certain similarity to the optical coherent control experiments for an atomic system where the interference between resonant and non-resonant transitions of atomic energy levels are controlled by spectrally encoded broadband laser pulses [73, 74, 75]. In semiconductors, if the densities of the continuum energy states are tunable, a similar but new kind of coherent control of optical transitions, in conjunction with the interference in FR, may be possible. We report a possible effect of such tunable densities of states in this Letter.

In semiconductor quantum wells, resonant exciton transitions generate a FR via the interference between the two channels, a discrete state of one subband of an electron-hole pair and energetically degenerate exciton continua pertaining to other subbands [76, 77]. Among the quantum wells, a GaAs/ $\text{Al}_x\text{Ga}_{1-x}\text{As}$ superlattice (SL) is interesting, as its continuum states for FR are supported by exciton mini-bands of the lower-lying Wannier-Stark ladder (WSL) [78, 79]. The continuum states are activated and controlled by an external Stark electric field, therefore the Fano coupling parameter Γ and the Fano shape parameter q may strongly depend on the field. Indeed, in a recent experiment [72], a monotonic decrease of

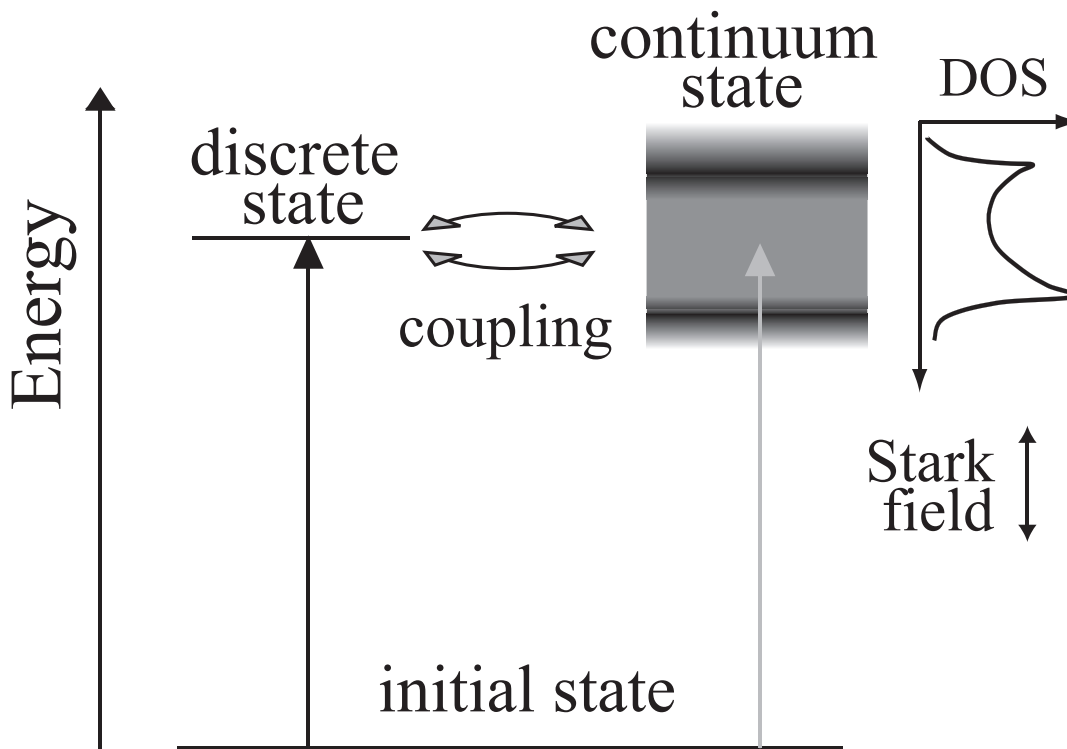


Figure 6.1: Schematic exciton energy diagram of a localized state and a Wannier-Stark mini-band in a quantum-well superlattice under an external electric Stark field. As the field varies, the mini-band becomes lifted in energy, then, the localized state couples to lower-energy states of the band. For a sufficiently wide window of field strength, the whole parabolic shape of the density of the mini-band states can play a role.

Γ was observed as the Stark field increases. This behavior is attributed to the fact that for a stronger Stark field, the WSL spacing and thus the momentum mismatch between the discrete exciton and the continuum at higher momentum increases, leading to a decrease of the coupling strength. Also, axial localization of the wave function develops as the field increases, contributing to the reduction of the Fano coupling [72].

The homogeneous broadening of the exciton transition described by Γ depends not only on the coupling matrix element but also on the density of states (DOS) of the continuum mini-band or the spectral shape and width of the continuum states. Therefore, the Fano profile is expected to depend on DOS of the continuum state, as depicted in Fig. 6.1, especially when the DOS is narrow or nonuniform near the resonance. However, the possible effects of the DOS on FR have been ignored or unnoticed, maybe because the Fano profile is a transition to the system of discrete and continuum states, *normalized with* the bare transition to the continuum state. Note that the original Fano formula does not include such effects but assumes a flat and wide DOS [62].

In this chapter, we report an experimental observation of the modified FR due to a non-uniform DOS in a GaAs/Al_{0.3}Ga_{0.7}As superlattice biased by a Stark field. We have observed an anomalous behavior of the Fano coupling parameter Γ , which does not follow the expected decreasing behavior [72] with increasing field strength. We attribute the anomalous behavior to the effect of the nonuniform DOS of continuum mini-bands sharply modified by the Stark field. By extending the original Fano formula to include the contribution of the energy-dependent DOS, we obtain the “bare” coupling parameter Γ_o .

with which the decreasing behavior of Fano coupling without the DOS contribution is then recovered.

The effect of the non-uniform DOS of continuum energy states is reflected on the Fano coupling and shape parameters. Following the approach of Ref. [80] based on a simple matrix algebra, we generally derive the DOS dependence of the Fano coupling and shape parameters. We start with a model system consisting of one discrete bound exciton state, $|\phi\rangle$, and a continuum of lower-lying Wannier-Stark (WS) states, $|\psi_E\rangle$, which are optically excited from an initial state $|i\rangle$. We assume that each of these states is nondegenerate, and the continuum has a non-uniform DOS, $\rho(E)$. We, then, have the Hamiltonian of which matrix elements are given as: $\langle\phi|H|\phi\rangle = E_\phi$, $\langle\psi_E|H|\phi\rangle = V_E$, $\langle\psi_{E'}|H|\psi_E\rangle = E \delta(E' - E)$. The optical absorption coefficient is determined as

$$A(\omega) = \text{Im}\langle i|\hat{T}\frac{1}{H - (\omega + i\eta)}\hat{T}|i\rangle \quad (6.2)$$

where \hat{T} is the transition operator. After straightforward calculations, we find the Fano formula of the absorption spectra

$$\frac{A(\omega)}{A(\infty)} = \frac{(\epsilon + q)^2}{\epsilon^2 + 1} \quad (6.3)$$

where the reduced energy is defined by $\epsilon = (2/\Gamma)(\omega - E_r)$. The *Fano coupling parameter* is given by

$$\Gamma = 2\pi\rho(E)|V_E|^2, \quad (6.4)$$

which explicitly represents the DOS dependence on the level broadening of the discrete state $|\phi\rangle$ due to coupling to the continuum state $|\psi_E\rangle$. The DOS effect on the *Fano shape parameter* q is also obtained as

$$q = \frac{1}{\pi\rho(E)V_E^*} \frac{\langle\Phi|\hat{T}|i\rangle}{\langle\psi_E|\hat{T}|i\rangle}, \quad (6.5)$$

which determines the asymmetry of the absorption spectra. Here $|\Phi\rangle$ is the discrete state modified by the coupling with the continuum state $|\psi_E\rangle$

$$|\Phi\rangle = |\phi\rangle + \mathcal{P} \int dE \rho(E) \frac{V_E}{\omega - E} |\psi_E\rangle \quad (6.6)$$

where \mathcal{P} represents a principal value.

For FR experiments on GaAs/Al_xGa_{1-x}As semiconductor superlattice quantum wells, as the “reversed” bias field increases, the energy states in Wannier-Stark ladder fan-out and the exciton states meet sequentially the lower lying WSL states in the neighboring quantum well. Also, the WSL states form effectively a continuum energy band for which the DOS has sharp peaks [81].

For our study, we have used an MBE-grown GaAs/Al_{0.3}Ga_{0.7}As superlattice with 35 GaAs quantum wells of 97-Å thickness (34 mono-layers) separated by 17-Å thick (6 mono-layers) Al_{0.3}Ga_{0.7}As barriers, clad on both side by 2500-Å Al_{0.3}Ga_{0.7}As buffer layers. This superlattice structure is similar to a structure previously studied for Bloch oscillations in [82]. It has a width of 19 meV for the lowest electron mini-band and 2 meV for the heavy-hole mini-band. For semi-transparent electric contact, a 500-Å thick Be-doped GaAs contact layer with a 100-Å nickel oxide and a 50-Å gold layers are prepared on the top of the structure. The entire structure was grown on a Si-doped GaAs substrate. Photo-reflectance measurements are carried out at a temperature of 4 K using a Fourier Transform Infrared Spectrometer (FTIR) [83].

In the absence of the Coulomb interaction, we know how the WSL state evolves from a continuum into resonant states as the bias Stark field increases. Assuming that the coupling does not occur among

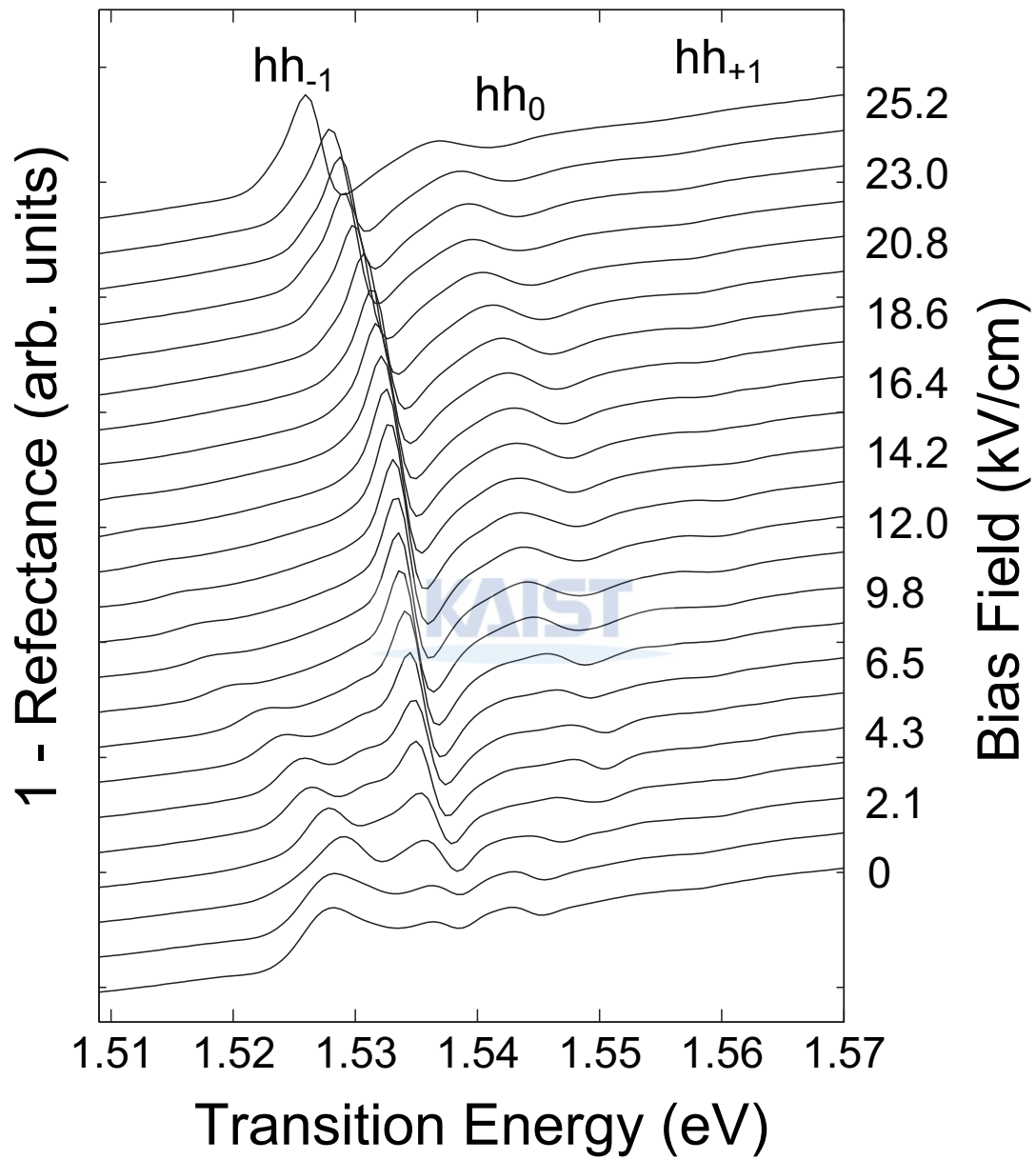


Figure 6.2: Excitonic spectra of a 97/17 Å superlattice for different bias Stark fields, measured in reflection.

the WSL states with different band indices, the field dependence of the single-particle WSL energy is given by Ref. [84]

$$E_n = E_0 + neFd \quad (n = 0, \pm 1, \pm 2, \dots). \quad (6.7)$$

This formula is applicable to our case, because the first band gap energy (≈ 60 meV) is larger than the maximum energy shift due to the bias field (≈ 23.8 meV). Hereafter we assume that every parameter implies the first band index.

Now, turning on the Coulomb interaction, the bound exciton state is formed below the lower miniband edge at zero bias field. Increasing the bias field, the bound exciton state and the continuum WSL state evolve so as to be coupled each other if their energies are matched. Such a coupling mechanism leads to the asymmetric FR in the absorption spectra [77]. In Fig. 6.2, the FR peak is the most prominent at the $n = -1, 0$ transitions. This is because the electronic portion of the $n = -1, 0$ exciton states is maximally overlapped with the heavy-hole state localized at the $n = 0$ quantum well so that the exciton state obtains the strongest absorption strength [78, 85].

The experimental reflection spectra as a function of the applied field is shown in Fig. 6.2. As the reverse bias field increases, the miniband-related excitons develop into WSL states. Below the onset of where the WSL starts to develop, three delocalized exciton lines in the SL miniband regime are identified, which we associate with the fundamental heavy-hole exciton (hh) and the light-hole exciton (lh) followed by the excited heavy-hole excitons and continuum, as previously observed [86, 82]. The continuum miniband has the width of 19 meV, from the Kronig-Penny model [87], and is located 4.9 meV above the exciton state. The spacings of WS states become 10 meV as the bias field of 13 kV/cm is applied. As the bias field increases, the energy levels of continuum states in neighboring quantum wells are dragged down or up, proportional to their spatial displacements from a particular quantum well where the exciton is formed. The edge of the continuum starts to meet the fanned-out WS state in the neighboring quantum well.

Figure 6.3 depicts the Fano coupling parameter Γ [Part (a)] and the shape parameter q [Part (b)], extracted using Eq. (6.1), for the hh_{-1} transition as the bias electric field was changed from 4.3 to 25.2 kV/cm. We observe a conventional behavior of an initial decrease of Γ followed by an anomalous behavior of an increase with increasing field. However, the DOS contribution to FR can be eliminated using the newly defined Fano “bare” coupling parameter Γ_o and “bare” shape parameter q_o

$$\Gamma_o = \frac{\rho(\bar{E})}{\rho(E)}\Gamma, \quad q_o = \frac{\rho(E)}{\rho(\bar{E})}q, \quad (6.8)$$

where $\rho(\bar{E})$ is the DOS measured at the center of the energy band. Then, the monotonous behavior of decreasing Fano resonance is retrieved. The extracted values for Fano shape parameter q displayed in Fig. 6.3(b) also show anomalous behavior, but it can be also corrected by the “bare” parameter q_o . If the effective DOS of the continuum has the shape of a suspension bridge, with local minimum in the middle and sharp edges on both sides as shown in Fig. 6.1, we expect that the Fano coupling Γ to be turned on fast, then it slowly becomes weaker near the central DOS minimum, and then becomes strong again as the other edge of the DOS approaches. While, Γ_o and q_o are defined to re-scale the DOS effect of FR resonance and therefore the monotonic behavior of these parameters are recovered. Eliminating the DOS contribution, the reasons of lowering Γ such as the momentum mismatch and the wave-function localization prevail. On the other hand, 67/17 Å superlattice used in [72] has a larger bandwidth (43 meV) of continuum band than in this experiment, which is almost twice of the resonance energy shift. The exciton level did not seem to bypass the DOS minimum and, therefore, the effect of DOS contribution to the FR has not arisen.

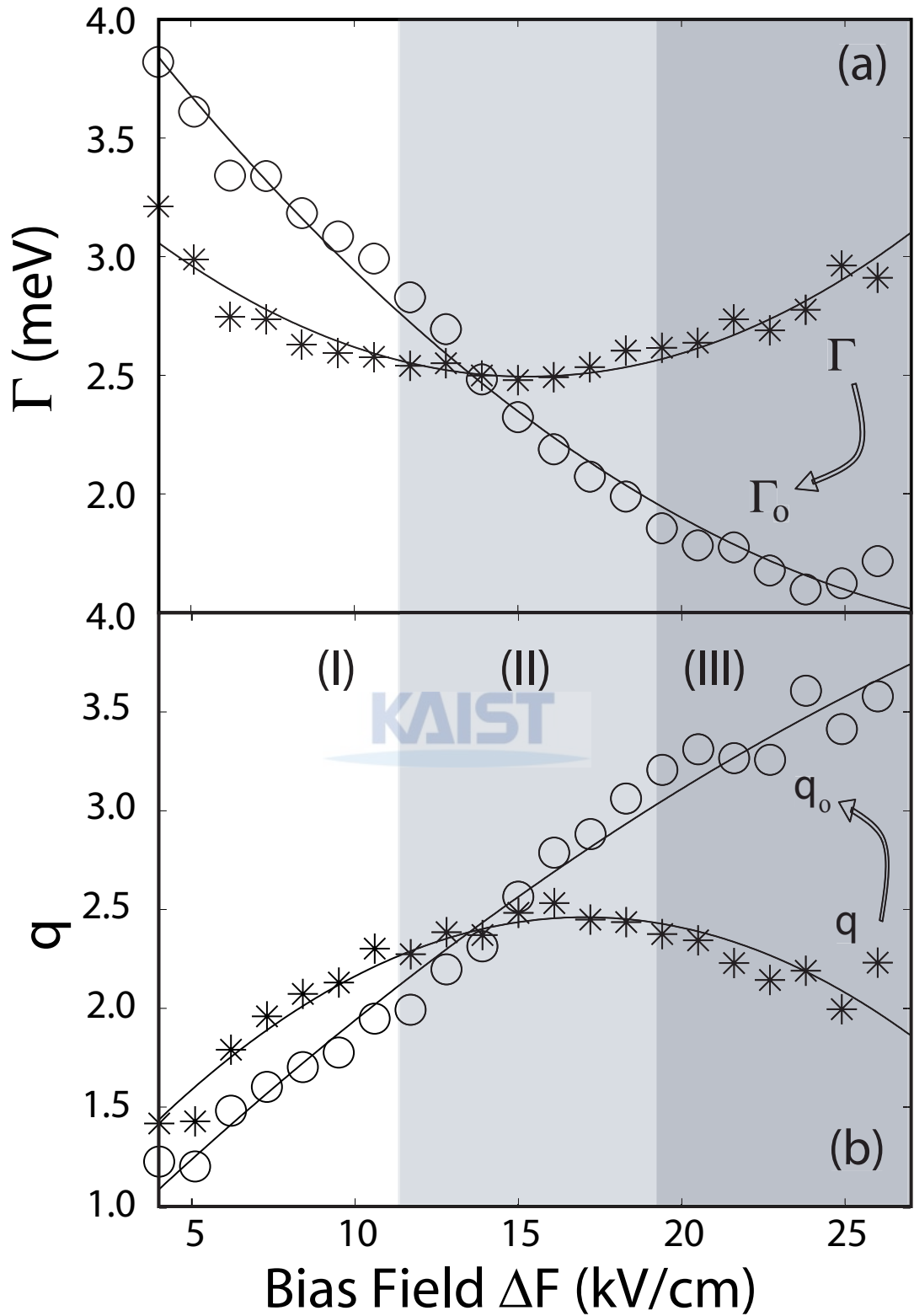


Figure 6.3: (a) The conventional Fano coupling parameter Γ (asterisks) and the “bare” coupling parameter Γ_o (circles) which compensates the effects of the density of continuum states, depicted as a function of the Stark field for the hh_{-1} transition. (b) The Fano shape parameter q (asterisks) and the Fano “bare” shape parameter q_o (circles).

The field dependence of the WSL states mostly changes the DOS which we speculate to cause the DOS dependence of Fano Γ and q parameters. When the bias electric field starts to exceed a threshold value, the WSL states, or the excitonic continuum states in [72], start to split off from the mini-band energy state. At the same time, the delocalized nature of the WS state gradually weakens as the field increases. In our experiment, the operating range of bias field is $F = 4.3 \sim 25.2$ (kV/cm), within which bias field the spacial extension of WSL states changes from 3 neighboring quantum wells down to 2 quantum wells. Thus, the hh_{-1} bound exciton, which we studied for FR, is first coupled to the next nearest neighboring lower WSL state ($n = -3$) and later coupled to the nearest neighboring state ($n = -2$), as in Fig. 6.4(I) and (III). In between, the bound exciton state passes through the valley, as in Fig. 6.4(II), between the two WSL states ($n = -3, -2$). As a result, the effective DOS felt by the hh_{-1} exciton transition is a parabolic shape as shown in the inset of Fig. 6.4.

The behavior of the Fano coupling and shape parameters in Fig. 6.3 is, therefore, related to the shape of DOS of WSL states. If the DOS effect is neglected, the Fano coupling decreases monotonically as the bias field increases, because of the two reasons: the axial localization of the wave function of the WSL state and the increasing momentum mismatch of energy transitions, which explains the (I) and (II) regimes of our experiments, as in Fig. 6.3 and 6.4. However, in the high-field regime (15.3 kV/cm \sim 25.2 kV/cm), the increase of the DOS of the WS state can be more dominant than the decrease of the coupling matrix element so that the Fano coupling increases as in Fig. 6.3(III).

In summary, we report an experimental observation of an anomalous behavior of FR coupling in a biased semiconductor superlattice. We attribute this observation to the effect of the non-uniform shape of the density of continuum states which is caused by resonant sweeping of an exciton state in between two neighboring extended WS states. The anomalous behavior of the Fano coupling and shape parameters in FR of superlattice is explained by a newly derived “bare” Fano parameters, Γ_o and q_o , with which the FR without DOS contribution is retrieved.

6.2 Semiconductor quantum well V -type systems

In this section, we consider semiconductor heterostructures, or quantum wells, made of III-V compounds as a possible experimental candidate for the 2D-FTCCS of V -type three-level systems. A quantum well is a semiconductor heterostructure that forms a well-known energy-level structure with a potential well. This structure can be grown by molecular beam epitaxy or chemical vapor deposition with high precision control technology of the layer thickness down to monolayers. The quantum well comprises a thin layer of a narrower-gap semiconductor sandwiched by layers of a wider-gap semiconductors. The carrier motion is limited to the quasi two dimensional planar region in the potential well. The density of states in bulk semiconductors, in which the carriers freely move in three dimensions, has a function of continuous square root of energy above the bandgap energy region. However, in the quantum well, the quasi two dimensional nature leads to the density of states being of distinct step values.

To build a quantum well heterostructure, more than two kinds of semiconductor materials are used. The materials must be lattice matched with each other. Figure 6.5 shows the bandgap energies given as a function of lattice constants of various III-V compounds. In fig. 6.5, GaAs, AlAs, and $Al_xGa_{1-x}As$ are lattice-matched for all Al compositions, and their bandgaps differ as a function of composition ratio x . Therefore, the binary compounds GaAs, and AlAs, and the ternary compounds $Al_xGa_{1-x}As$ are widely used for semiconductor quantum well systems.

To form a V -type system, we consider a double quantum well structure. For this, we need to

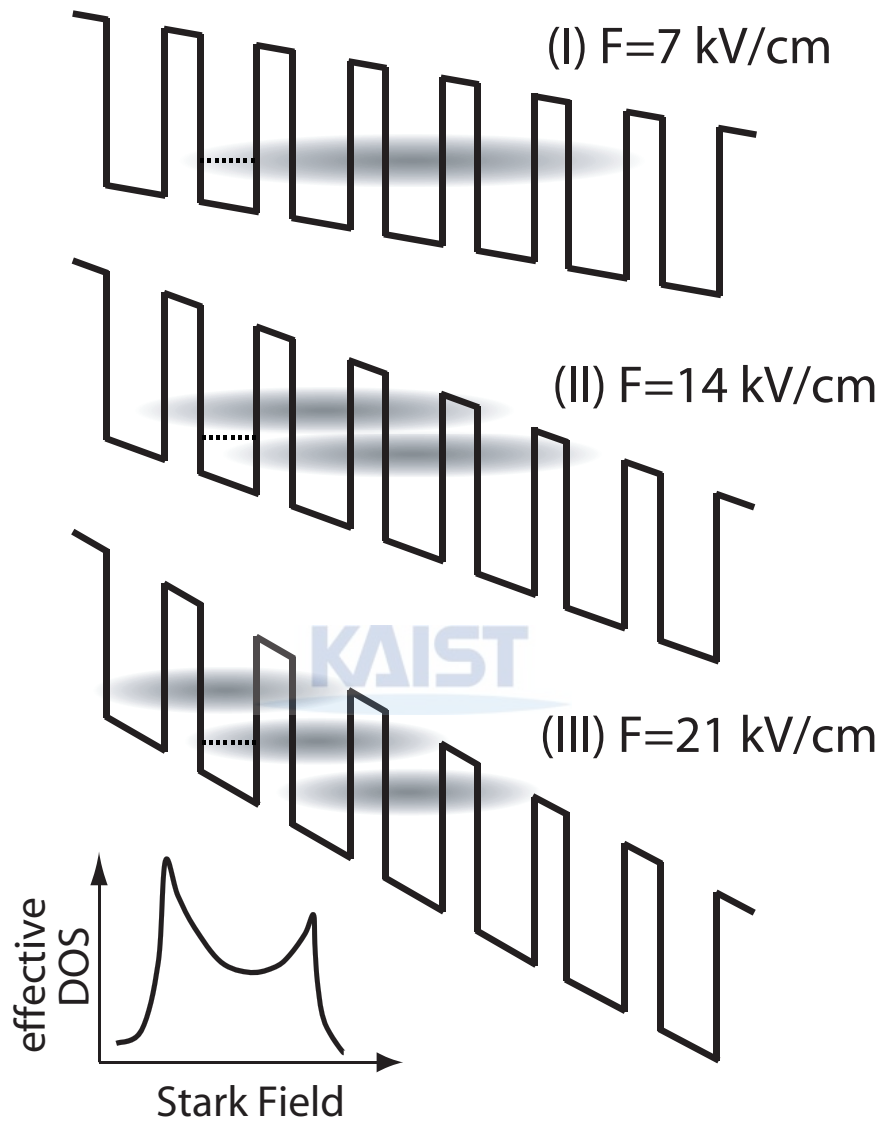


Figure 6.4: Fano resonance of an exciton state with neighboring extended Wannier-Stark states. Between the resonant couplings with the next nearest neighboring WS state in (I) and with the nearest neighboring WS state in (III), the exciton state resonantly sweeps through the energy interval, having the minimal coupling somewhere in between as in (II). The effective density of states felt by the exciton states as a function of bias electric field shows a parabolic behavior.

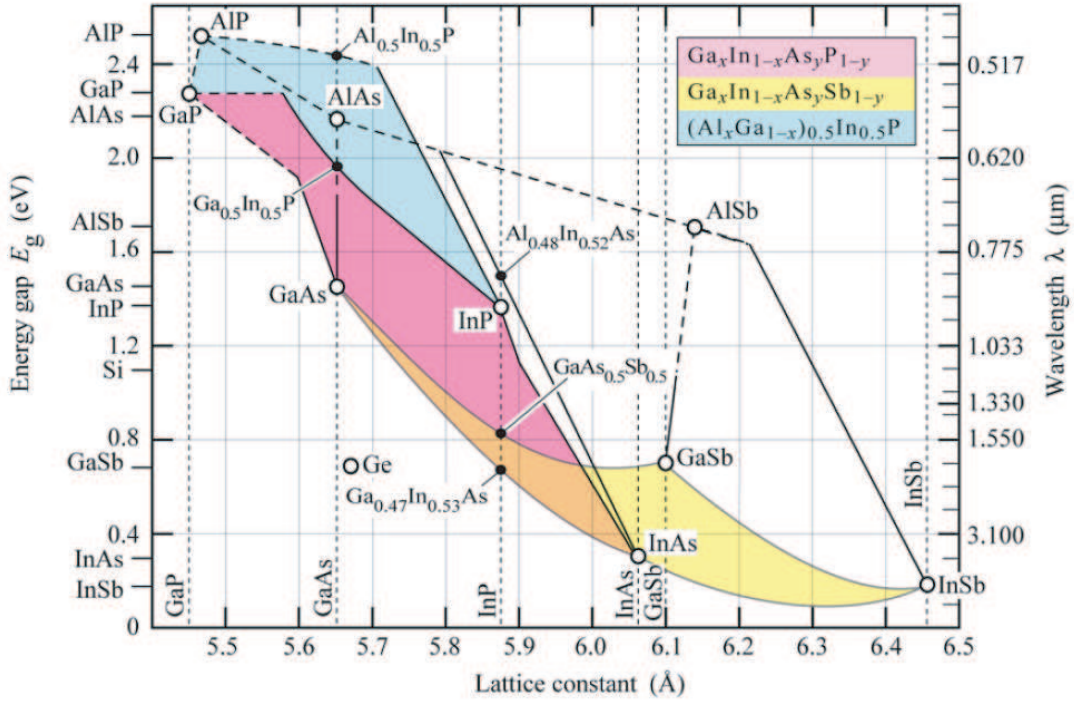


Figure 6.5: Bandgap energy and lattice constant of various III-V compounds at room temperature (adopted from Tien 1988).

compose the transition energies between the ground and excited states. One of the advantages of the semiconductor quantum well is the freedom to design the transition energies. In the case of $\text{Al}_x\text{Ga}_{1-x}\text{As}$ compounds, the energies can be tuned by changing the mole-fraction x . However, this method changes the ground state energy significantly due to the band offset, resulting the quantum system to become a four-level system. Another way is that we can also change the transition energies by modifying the well width L . Using the simplest method of the infinite well approximation, the quantum energies of the carrier are given by

$$E_n = \frac{\hbar^2}{2m^*} \left(\frac{(n+1)\pi}{L} \right)^2, \quad (6.9)$$

where E_n s are the bound state energies, m^* the effective mass of the carrier, L the potential well width, and n the index of the bound states ($n = 0, 1, 2, \dots$). By selecting L , the quantized energy E_n can be designed. Figure 6.6 (a) shows the band diagram of a GaAs/AlGaAs double quantum well system composed of 17-Å thick $\text{Al}_{0.3}\text{Ga}_{0.7}\text{As}$ (6 mono-layers) barrier, and two quantum wells of 79.2-Å thick GaAs (28 mono-layers, labeled as 1), and 73.6-Å thick GaAs (26 mono-layers, labeled as 2) clad on both side by $\text{Al}_{0.3}\text{Ga}_{0.7}\text{As}$ buffer layers. In this case, at room temperature, the transition energies $E_1 = 1.522\text{eV}$ (815 nm) and $E_2 = 1.536\text{eV}$ (807 nm), suited for our experimental condition. The excited states energies are shown in Fig 6.6 (a) along with the ground state energy. As expected, the excited states are split and the ground state energy is almost the same in both layers due to the heavier effective hole mass. The wavefunctions of the excited states and the ground state are depicted in Fig. 6.6 (b).

However, the inter-well transition, or quantum tunneling, is much weaker than the inner-well transition. Also, the splitting of the ground state energy causes a peak broadening which is important factor in 2D-FTOS technique. To satisfy the ideal condition of one ground state and two excited states, and also a comparable transition strength for the both excited states, we consider a more sophisticated structure.

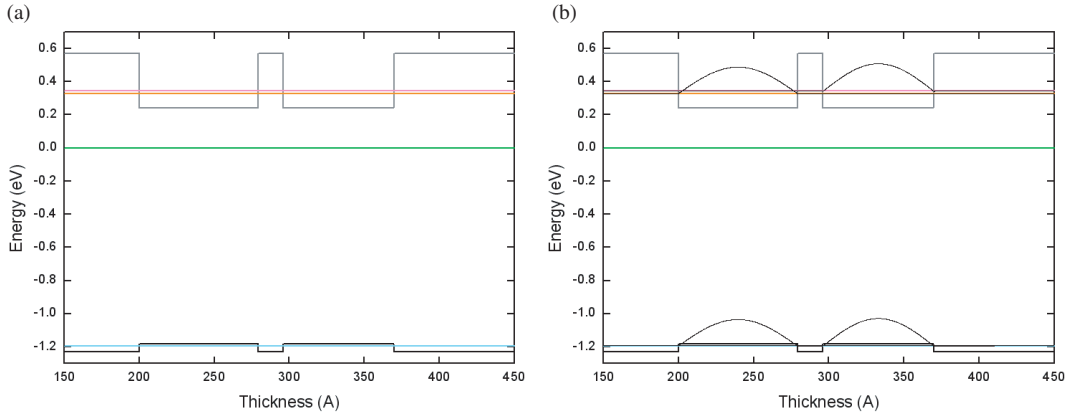


Figure 6.6: (a) Band diagram of the double-quantum well structure and the energies of the bound states. Band diagrams are shown in black (valence band) and gray (conduction band) lines, and the excited states energies in pink (narrower well) and orange (wider well). Green line is the Fermi energy. (b) Band diagram with wavefunctions of the bound states.

Figure 6.7 shows the band diagram of the devised double quantum well structure in which one ground state is in 2-layer, and two excited states are in 1- and 3-layers. Again, the widths of 1- and 3-layers are different.

To make this band diagram, we must satisfy three requirements: the valence band and conduction band of the 2-layer are higher than those of 1- and 3-layers, the valence bands and conduction bands of 1- and 3-layers are lower than those of outside cladding layers, and all compounds in each layer must be lattice matched. Figure 6.8 shows band edges of III-V compounds as a function of lattice constant. In this diagram, the combination of $\text{Al}_x\text{Ga}_{1-x}\text{As}$ and InGaP satisfies the conditions. Figure 6.7 is the calculated band diagram of a $\text{InGaP}/\text{Al}_{0.3}\text{Ga}_{0.7}\text{As}/\text{InGaP}$ quantum well system, composed of 79.2-Å thick $\text{In}_{0.5}\text{Ga}_{0.5}\text{P}$ (28 mono-layers) for 1-layer, 48.1-Å thick $\text{Al}_{0.3}\text{Ga}_{0.7}\text{As}$ (17 mono-layers) for 2-layer, and 73.6-Å thick $\text{In}_{0.5}\text{Ga}_{0.5}\text{P}$ (26 mono-layers) for 2-layer clad on both side by $\text{Al}_{0.9}\text{Ga}_{0.1}\text{As}$ layers. At room temperature, the transition energies are calculated by solving 1-D Poisson equation as $E_1 = 1.525\text{eV}$ (814 nm) and $E_2 = 1.535\text{eV}$ (808 nm). The aluminium mole-fraction of 2-layer and the widths of 1- and 3-layers are tested for a number of sets, and the above mentioned structure fulfills the experimental requirements.

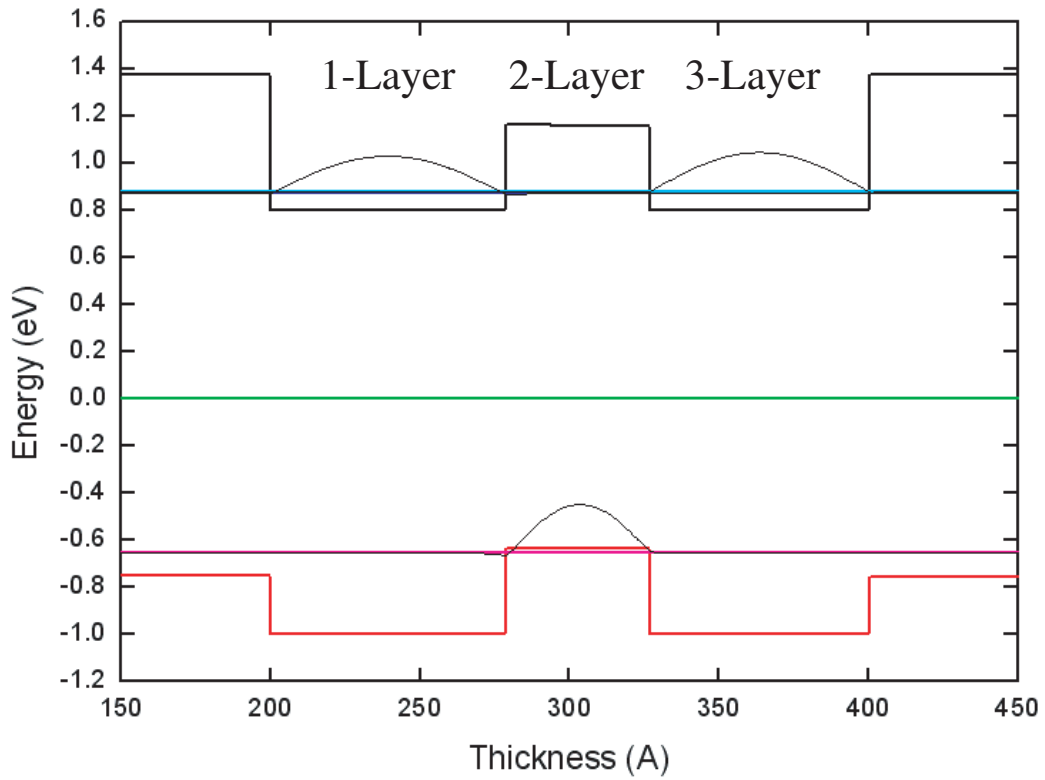


Figure 6.7: Band diagram of the newly designed double-quantum well structure forming a V-type quantum system and the wavefunctions of one ground state and two excited states.

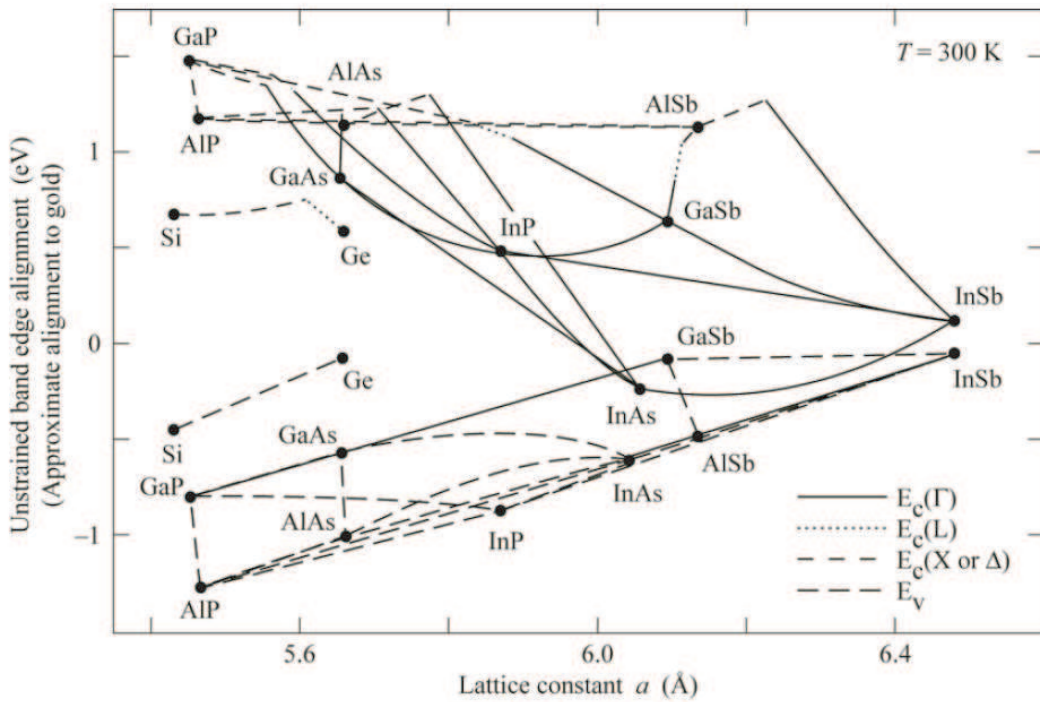


Figure 6.8: Band edges as a function of lattice constant of various III-V compounds at room temperature, relative to Fermi level of gold Schottky contact (after Tiwari and Frank, 1992).

Chapter 7. Conclusion

One of the fundamental goals in chemical physics and biophysics is to understand how molecular structural dynamics, which are often manifested in *inter-excited electronic state transitions*, proceed during chemical reactions or interactions with light and what the implications are for known chemical and biological processes. The best known tool is two-dimensional nuclear magnetic resonance (2D-NMR) spectroscopy, which is especially useful for the detailed analysis of molecular structures. However, 2D-NMR is primarily limited to probing relatively small molecular systems, and structural evolution occurring in sub-picosecond time scale is too fast for 2D-NMR to resolve. Alternatively, 2D Fourier transform optical spectroscopy (2D-FTOS), an optical extension of 2D-NMR, has been recently developed to probe femtosecond electronic and vibrational dynamics. It can be applied to molecules as large as small proteins and providing ultrafast time resolution which is crucial for understanding reaction dynamics and energy transfer processes.

In this thesis, we pursued a new method that harnesses the ability of controlling the evolution of quantum systems to 2D-FTOS, 2D-Fourier transform coherent control spectroscopy (2D-FTCCS). Quantum mechanical control of matters, known as quantum control or coherent control, utilizes programmed light forms, and has become one of the general scientific subjects of extreme interest because of its unprecedented control capability over the dynamics of atoms and molecules. In particular, with the recent development of the ultrafast optical technique of shaping laser pulses, termed ultrafast pulse shaping, coherent control has been demonstrated in a variety of material substances extending from atoms and molecules to solid-state and biological systems.

We described the first experimental demonstration of coherent control of transitions between two excited states in a V -type system. To do this, we adopted 2D-FTCCS to lowest three energy levels of atomic rubidium: the target transition probabilities were retrieved from distinct 2D Fourier-transform spectral peaks that are inherent to their transition pathways, thereby the controlled transition probability amplitudes were obtained. By shaping one of the three laser pulses used in 2D-FTOS, we selectively turned on and off the $5P_{1/2}$ - $5P_{3/2}$ transition of atomic rubidium. Furthermore considering the quantum interference of possible transition paths analytically, the target transition was engineered tripled relative to the Fourier-transform limited pulse case. Also, we showed that the conventional coherent transients (CTs) in a simple two-level system is mimicked by two-photon coherent control in a V -shape three-level system. Here, higher order chirps of a shaped laser pulse play the roles of time and linear chirp in CTs. In use of 2D-FTCCS, the phase and amplitude of controlled transition probability were successfully retrieved from a 2D Fourier-transform spectral peak.

We expect that this novel coherent control technique or advanced 2D-FTOS scheme, demonstrated on an atomic model system, to be applied to various fields of researches and practical systems. We proposed to perform the advanced 2D-FTOS study on semiconductor V -type systems for realization of quantum computing via multiple quantum operations within excited states.

References

- [1] K. Bergmann, H. Theuer, and B. W. Shore, “Coherent population transfer among quantum states of atoms and molecules,” *Rev. Mod. Phys.* **70**, 1003-1025 (1998).
- [2] M. Shapiro and P. Brumer, *Principles of the Quantum Control of Molecular Processes*, (Wiley, New York, 2003).
- [3] D. J. Tanner and S. A. Rice, “Control of selectivity of chemical reaction via control of wavepacket evolution,” *J. Chem. Phys.* **83**, 5013-5018 (1985).
- [4] M. Shapiro, P. Brumer, “Laser control of product quantum state populations in unimolecular reactions,” *J. Chem. Phys.* **84**, 4103-4104 (1986).
- [5] E. D. Potter, J. L. Herek, S. Pedersen, Q. Liu, and A. H. Zewail, “Femtosecond laser control of a chemical reaction,” *Nature* **355**, 66-68 (1992).
- [6] A. Assion, T. Baumert, J. Helbing, V. Seyfried, and G. Gerber, “Coherent control by a single phase shaped femtosecond laser pulse,” *Chem. Phys. Lett.* **259**, 488 (1996).
- [7] L. Costa, M. Betz, M. Spasenovic, A. D. Bristow, and H. M. van Driel, “All-optical injection of ballistic electrical currents in unbiased silicon,” *Nature Physics* **3**, 632 (2007).
- [8] T. C. Weinacht, J. Ahn, and P. H. Bucksbaum, “Controlling the shape of a quantum wavefunction,” *Nature* **397**, 233-235 (1999).
- [9] J. P. Ogilvie, D. Debarre, X. Solinas, J.-L. Martin, E. Beaurepaire, and M. Joffre, “Use of coherent control for selective two-photon fluorescence microscopy in live organisms,” *Opt. Express* **14**, 759-766 (2006).
- [10] P. F. Moulton, “Spectroscopic and laser characteristics of Ti:Al₂O₃,” *J. Opt. Soc. Am. B*, **3**, 125-133 (1986).
- [11] D. E. Spence, P. N. Kean, and W. Sibbett, “60-fsec pulse generation from a self-mode-locked Ti:sapphire laser,” *Opt. Lett.* **16**, 42 (1991).
- [12] A. M. Weiner, D. E. Leaird, G. P. Wiederrecht, and K. A. Nelson, “Femtosecond Pulse Sequences Used for Optical Manipulation of Molecular Motion,” *Science* **247**, 1317-1319 (1990).
- [13] C. J. Bardeen, V. V. Yakovlev, K. R. Wilson, S. D. Carpenter, P. M. Weber, and W. S. Warren, “Feedback quantum control of molecular electronic population transfer,” *Chem. Phys. Lett.* **280**, 151-158 (1997).
- [14] N. Dudovich, B. Dayan, S. M. Gallagher-Faeder, and Y. Silberberg, “Transform-limited pulses are not optimal for resonant multiphoton transitions,” *Phys. Rev. Lett.* **86**, 47 (2001).
- [15] M. C. Stowe, A. Peer, and J. Ye, “Control of Four-Level Quantum Coherence via Discrete Spectral Shaping of an Optical Frequency Comb,” *Phys. Rev. Lett.* **100**, 203001 (2008).

- [16] S. D. Clow, C. Trallero-Herrero, T. Bergeman, and T. Weinacht, “Strong Field Multiphoton Inversion of a Three-Level System Using Shaped Ultrafast Laser Pulses,” *Phys. Rev. Lett.* **100**, 233603 (2008).
- [17] S. Lee, J. Lim, J. Ahn, V. Hakobyan, and S. Guerin, “Strong-field two-level two-photon transition by phase shaping,” *Physical Review A* **82**, 023408 (2010).
- [18] D. M. Jonas, “Two-dimensional femtosecond spectroscopy,” *Annu. Rev. Phys. Chem.* **54**, 425 (2003).
- [19] P. Tian, D. Keusters, Y. Suzuki, and W. S. Warren, “Femtosecond phase-coherent two-dimensional spectroscopy,” *Science* **300**, 1553 (2003).
- [20] K. W. Stone, K. Gundogdu, D. B. Turner, X. Li, S. T. Cundiff, and K. A. Nelson, “Two-quantum 2D FT electronic spectroscopy of biexcitons in GaAs quantum wells,” *Science* **324**, 1169 (2009).
- [21] G. E. Martin, and A. S. Zekter, *Two-Dimensional NMR Methods for Establishing Molecular Connectivity*, (Wiley-VCH, New York, 1988).
- [22] T. Brixner, J. Stenger, H. M. Vaswani, M. Cho, R. E. Blankenship, and G. R. Fleming, “Two-dimensional spectroscopy of electronic couplings in photosynthesis,” *Nature* **434**, 625 (2005).
- [23] R. S. Judson and H. Rabitz, “Teaching lasers to control molecules,” *Phys. Rev. Lett.* **68**, 1500 (1992).
- [24] A. Assion, T. Baumert, M. Bergt, T. Brixner, B. Kiefer, V. Seyfried, M. Strehle, and G. Gerber, “Control of chemical reactions by feedback-optimized phase-shaped femtosecond laser pulses,” *Science* **282**, 919 (1998)
- [25] R. Bartels, S. Backus, E. Zeek, L. Misoguti, G. Vdovin, I. P. Christov, M. M. Murnane, and H. C. Kapteyn, “Shaped-pulse optimization of coherent emission of high-harmonic soft X-rays,” *Nature (London)* **406**, 164 (2000).
- [26] H. Rabitz, R. de Vivie-Riedle, M. Motzkus, and K. Kompa, “Whither the future of controlling quantum phenomena?” *Science* **288**, 824 (2000).
- [27] D. Meshulach and Y. Silberberg, “Coherent quantum control of two-photon transitions by a femtosecond laser pulse,” *Nature (London)* **396**, 239 (1998).
- [28] D. Meshulach and Y. Silberberg, “Coherent quantum control of multiphoton transitions by shaped ultrashort optical pulses,” *Phys. Rev. A* **60**, 1287 (1999).
- [29] R. L. Fork, B. I. Greene, and C. V. Shank, “Generation of optical pulses shorter than 0.1 psec by colliding pulse mode locking,” *Appl. Phys. Lett.* **38**, 671 (1981).
- [30] R. L. Fork, C. H. Brito Cruz, P. C. Becker, and C. V. Shank, “Compression of optical pulses to six femtoseconds by using cubic phase compensation,” *Opt. Lett.* **12**, 483 (1987).
- [31] C. Froehly, B. Colombeau, and M. Vampouille, *Shaping and Analysis of Picosecond Light Pulses*, in *Progress in Optics*, edited by E. Wolf **20**, 65-153 (1983).
- [32] A. M. Weiner, “Femtosecond pulse shaping using spatial light modulators,” *Rev. Sci. Instrum.* **71**, 1929 (2000).

- [33] A. M. Weiner, J. P. Heritage, and E. M. Kirschner, “High-resolution femtosecond pulse shaping,” *J. Opt. Soc. Am. B* **5**, 1563 (1988).
- [34] A. M. Weiner, J. P. Heritage, and J. A. Salehi, “Encoding and decoding of femtosecond pulses,” *Opt. Lett.* **13**, 300 (1988).
- [35] L. Brillouin, “Diffusion of Light and X-rays by a Transparent Homogeneous Body,” *Ann. Phys. (Paris)* **17**, 88-122 (1922).
- [36] P. Debye, and F.W. Sears, “On the scattering of light by supersonic waves,” *Proc. Nat. Acad. Sci. USA* **18**, 409-414 (1932).
- [37] R. Lucas, and P. Biquard, “Optical properties of solid and liquid medias subjected to high-frequency elastic vibrations,” *Journal Phys.* **71**, 464-477 (1932).
- [38] F. Verluise, V. Laude, Z. Cheng, Ch. Spielmann, and P. Tournois, “Amplitude and phase control of ultrashort pulses by use of an acousto-optic programmable dispersive filter: pulse compression and shaping,” *Optics Letters* **25**, 575 (2000).
- [39] P. Tournois, “Acousto-optic programmable dispersive filter for adaptive compensation of group delay time dispersion in laser systems,” *Opt. Commun.* **140**, 245 (1997).
- [40] F. Verluise, V. Laude, J.-P. Huignard, P. Tournois, and A. Migus, “Arbitrary dispersion control of ultrashort optical pulses with acoustic waves,” *J. Opt. Soc. Am. B* **17**, 138 (2000).
- [41] W. S. Warren, H. Rabitz, and M. Dahleh, “Coherent control of quantum dynamics: the dream is alive,” *Science* **259**, 1581 (1993).
- [42] R. J. Gordon, and S. A. Rice, “Active control of the dynamics of atoms and molecules,” *Annu. Rev. Phys. Chem.* **48**, 601 (1997).
- [43] T. Brixner, N. H. Damrauer, B. Kiefer, and G. Gerber, “Liquid-phase adaptive femtosecond quantum control: Removing intrinsic intensity dependencies,” *J. Chem. Phys.* **118**, 3692 (2003).
- [44] N. H. Damrauer, T. R. Boussie, M. Devenney, and J. K. McCusker, “Effects of Intraligand Electron Delocalization, Steric Tuning, and Excited-State Vibronic Coupling on the Photophysics of Aryl-Substituted Bipyridyl Complexes of Ru(II),” *J. Am. Chem. Soc.* **119**, 8253 (1997).
- [45] S. Zamith, J. Degert, S. Stock, B. de Beauvoir, V. Blanchet, M. Aziz Bouchene, and B. Girard, “Observation of coherent transients in ultrashort chirped excitation of an undamped two-level system,” *Phys. Rev. Lett.* **87**, 033001 (2001).
- [46] J. Degert, W. Wohlleben, B. Chatel, M. Motzkus, and B. Girard, “Realization of Time-Domain Fresnel Lens with Coherent Control,” *Phys. Rev. Lett.* **89**, 203003 (2002).
- [47] N. Dudovich, D. Oron, and Y. Silberberg, “Coherent Transient Enhancement of Optically Induced Resonant Transitions,” *Phys. Rev. Lett.* **88**, 123004 (2002).
- [48] A. Monmayrant, B. Chatel, and B. Girard, “Quantum state measurement using Coherent transients,” *Phys. Rev. Lett.* **96**, 103002 (2006).

- [49] Jonseok Lim, Han-gyeol Lee, Jae-uk Kim, and Jaewook Ahn, “Quantum control of two-photon transitions between intrashell excited states with 2D Fourier transform spectroscopy,” *Phys. Rev. Lett.* submitted.
- [50] G. S. Engel, T. R. Calhoun, E. L. Read, T. Ahn, T. Mancal, Y. Cheng, R. E. Blankenship, and G. R. Fleming, “Evidence for wavelike energy transfer through quantum coherence in photosynthetic systems,” *Nature* **446**, 782-786 (2007).
- [51] Hohjai Lee, Yuan-Chung Cheng, and Graham R. Fleming, “Coherence dynamics in photosynthesis: protein protection of excitonic coherence,” *Science* **316**, 1462-1465 (2007).
- [52] M. Mohseni, P. Rebentrost, S. Lloyd, and A. Aspuru-Guzik, “Environment-assisted quantum walks in photosynthetic energy transfer,” *J. Chem. Phys.* **129**, 174106 (2008).
- [53] D. E. Tronrud, and M. F. Schmid, and B. W. Matthews, “Structure and X-ray amino acid sequence of a bacteriochlorophyll a protein from *Prosthecochloris aestuarii* refined at 1.9 Å resolution,” *J. Mol. Biol.* **188**, 443-454 (1986).
- [54] R. E. Fenna, and B. W. Matthews, “Chlorophyll arrangement in a bacteriochlorophyll protein from *Chlorobium limicola*,” *Nature* **258**, 573-577 (1975).
- [55] S. I. E. Vulto, S. Neerken, R. J. W. Louwe, M. A. de Baat, J. Amesz, and T. J. Aartsma, “Exciton simulations of optical spectra of the FMO complex from the green sulfur bacterium *Chlorobium tepidum* at 6 K,” *J. Phys. Chem. B.* **102**, 10630-10635 (1998).
- [56] M. Wendling, D. Gulen, S. I. E. Vulto, T. J. Aartsma, R. van Grondelle, and H. van Amerongen, “The quantitative relationship between structure and polarized spectroscopy in the FMO complex of *Prosthecochloris aestuarii*: refining experiments and simulations,” *Photosynth. Res.* **71**, 99-123 (2002).
- [57] S. Savikhin, D. R. Buck, and W. S. Struve, “Toward level-to-level energy transfers in photosynthesis: The Fenna-Matthews-Olson protein,” *J. Phys. Chem. B* **102**, 5556-5565 (1998).
- [58] A similar expression for a two-photon transition in a ladder-type quantum system is given by Eq. (3) in Ref. [14].
- [59] X. Li, T. Zhang, C. N. Borca, and S. T. Cundiff, “Many-body interactions in semiconductors probed by optical two-dimensional Fourier transform spectroscopy,” *Phys. Rev. Lett.* **96**, 057406 (2006).
- [60] Jongseok Lim, Han-gyeol Lee, Jae-uk Kim, and Jaewook Ahn, “Coherent transients mimicked by two-photon coherent control of a three-level system,” *Phys. Rev. A* accepted.
- [61] Jongseok Lim, Woo-Ram Lee, Heung-Sun Sim, Richard D. Averitt, Joshua M. Zide, Arthur C. Gossard, and Jaewook Ahn, “Effect of non-uniform continuum density of states on Fano resonance in semiconductor quantum wells,” *Phys. Rev. B* **80**, 035322 (2009).
- [62] U. Fano, “Effects of configuration interaction on intensities and phase shifts,” *Phys. Rev.* **124**, 1866 (1961).
- [63] A. R. P. Rau, “Perspectives on the Fano resonance formula,” *Physica Scripta* **69**, C10 (2004).
- [64] See, for instance, H. C. Bryant, et al., *Phys. Rev. Lett.* **38**, 228 (1977).

- [65] S. Bar-Ad, P. Kner, M. V. Marquezini, S. Mukamel, D. S. Chemla, “Quantum confined Fano interference,” *Phys. Rev. Lett.* **78**, 1363 (1997).
- [66] J. F. Song, Y. Ochiai, and J. P. Bird, “Fano resonances in open quantum dots and their application as spin filters,” *Appl. Phys. Lett.* **82**, 4561 (2003).
- [67] S. Glutsch, U. Siegner, M.-A. Mycek, and D. S. Chemla, “Fano resonances due to coupled magnetoexciton and continuum states in bulk semiconductors,” *Phys. Rev. B* **50**, 17009 (1994).
- [68] L. Esaki, and R. Tsu, “Superlattice and negative differential conductivity in semiconductors,” *IBM J. Res. Dev.* **14**, 61 (1970).
- [69] S. Glutsch, D. S. Chemla, and F. Bechstedt, “Fano resonances in the optical spectra of semiconductor quantum structures,” *Phys. Rev. B* **51**, 16885 (1995).
- [70] K. Kobayashi, H. Aikawa, S. Katsumoto, and Y. Iye, “Tuning of the fano effect through a quantum dot in an aharonov-bohm interferometer,” *Phys. Rev. Lett.* **88**, 256806 (2002).
- [71] S. Fan, W. Suh, and J. D. Joannopoulos, “Temporal coupled-mode theory for the Fano resonance in optical resonators,” *J. Opt. Soc. Am. A* **20**, 569 (2003).
- [72] C. P. Holfeld, F. Löser, M. Sudzius, K. Leo, D. M. Whittaker, and K. Köhler, “Fano resonances in semiconductor superlattices,” *Phys. Rev. Lett.* **81**, 874 (1998).
- [73] S. A. Rice, “New ideas for guiding the evolution of a quantum system,” *Science* **258**, 412 (1992); P. Brumer, and M. Shapiro, “Laser control of chemical reactions,” *Sci. Am.* **272**, 34 (1995).
- [74] W. S. Warren, H. Rabitz, and M. Dahleh, “Coherent control of quantum dynamics: the dream is alive,” *Science* **259**, 1581 (1993).
- [75] D. Meshulach and Y. Silberberg, “Coherent quantum control of two-photon transitions by a femtosecond laser pulse,” *Nature* **396**, 239, (1998).
- [76] D. Y. Oberli, G. Böhm, G. Weimann, and J. A. Brum, “Fano resonances in the excitation spectra of semiconductor quantum wells,” *Phys. Rev. B* **49** 5757 (1994).
- [77] D. M. Whittaker, “Saddle-points and Stark ladders: high-resolution calculations of exciton spectra in superlattices,” *Europhys. Lett.* **31**, 55 (1995).
- [78] M. M. Dignam and J. E. Sipe, “Exciton Stark ladder in GaAs/Ga_{1-x}Al_xAs superlattices,” *Phys. Rev. Lett.* **64**, 1797 (1990); M. M. Dignam and J. E. Sipe, “Exciton Stark ladder in semiconductor superlattices,” *Phys. Rev. B* **43**, 4097 (1991).
- [79] K. Gibb, M. M. Dignam, J. E. Sipe, and A. P. Roth, “Observation of Wannier-Stark localization by electroreflectance spectroscopy,” *Phys. Rev. B* **48**, 8156 (1993).
- [80] S. Glutsch, “Optical absorption of the Fano model: General case of many resonances and many continua,” *Phys. Rev. B* **66**, 075310 (2002).
- [81] S. Glutsch and F. Bechstedt, “Interaction of Wannier-Stark ladders and electrical breakdown in superlattices,” *Phys. Rev. B* **60**, 16584 (1999).

- [82] C. Waschke, H. G. Roskos, R. Schwedler, K. Leo, H. Kurz and K. Köhler, “Coherent submillimeter-wave emission from Bloch oscillations in a semiconductor superlattice,” *Phys. Rev. Lett.* **70**, 3319 (1993).
- [83] H. C. Chui, S. M. Lord, E. Martinet, M. M. Fejer, and J. S. Harris, Jr., “Intersubband transitions in high indium content InGaAs/AlGaAs quantum wells,” *Appl. Phys. Lett.* **63** 364 (1993).
- [84] E. O. Kane, “Zener tunneling in semiconductors,” *J. Phys. Chem. Solids* **12**, 181 (1959).
- [85] N. Linder, “Excitons in superlattices: Absorption asymmetry, dimensionality transition, and exciton localization,” *Phys. Rev. B* **55**, 13664 (1997).
- [86] E. E. Mendez, F. Agullo-Rueda, and J. M. Hong, “Stark localization in GaAs-GaAlAs superlattices under an electric field,” *Phys. Rev. Lett.* **60**, 2426 (1988).
- [87] G. Bastard, “Superlattice band structure in the envelope-function approximation,” *Phys. Rev. B* **24**, 5693 (1981).
- [88] C. B. Alcock, V. P. Itkin, and M. K. Horrigan, “Vapor Pressure Equations for the Metallic Elements: 298-2500K,” *Canadian Metallurgical Quarterly* **23**, 309 (1984).
- [89] David R. Lide (Ed.), *CRC Handbook of Chemistry and Physics*, 82nd ed. (CRC Press, Boca Raton, 2001).
- [90] S. Chelkowski and A. D. Baundrauk, “Control of molecular vibrational excitation and dissociation by chirped intense infrared laser pulses. Rotational effects,” *J. Chem. Phys.* **99**, 4279-4287 (1993).
- [91] B. Amstrup, G. Szabo, R. A. Sauebrey, and A. Lörincz, “Chirped pulse control of CsI fragmentation: an experimental possibility,” *Chem. Phys.* **188**, 87-97 (1994).
- [92] U. Gaubatz, P. Rudecki, S. Schiemann, and K. Bergmann, “Population transfer between molecular vibrational levels by stimulated Raman scattering with partially overlapping laser fields. A new concept and experimental results,” *J. Chem. Phys.* **92**, 5363 (1990).
- [93] J. Karczmarek, J. Wright, P. Corkum, and M. Ivanov, “Optical centrifuge for molecules,” *Phys. Rev. Lett.* **82**, 3420-3423 (1999).
- [94] E. Hecht, *Optics, (4th ed.)* (Addison Wesley, 2002).
- [95] W. Merkel, H. Mack, W. P. Schleich, E. Lutz, G. G. Paulus, and B. Girard, “Chirping a two-photon transition in a multistate ladder,” *Phys. Rev. A* **76**, 023417 (2007).

Summary

Quantum Control in Two-Dimensional Fourier Transform Optical Spectroscopy

자연현상을 관찰하고 논리적으로 인식하는 것을 목적으로 하는 물리학에서, 양자상태함수를 준비하고 프로그램된 방향으로 전개, 그리고 측정을 통해 자연법칙을 이해하는 활동은 물리학을 연구하는 사람들의 근본적인 연구방법이다. 따라서 원자, 분자, 또는 반도체 등 다양한 양자계에서 만들어지는 양자상태를 이루는 전자를 재단된 광자로 조정하는 양자제어기술은 제안됨과 동시에 집중적 관심속에 활발한 연구가 이루어져 왔다. 또한, 양자계의 결맞음을 이용하여 양자함수를 이루는 상태함수들 사이의 연결법칙을 직접적으로 보여주는 이차원 푸리에 분광학은 양자계, 나아가 자연현상을 이해하고자 하는 물리학에서 전도유망한 혁신적인 도구로 관심을 모으고 있다.

이차원 푸리에 분광학의 기본 도구로 사용되는 펨토초 레이저는 시간상에서 매우 짧은 시간폭을 갖는 장점을 통해 피코초 시간 수준에서 이뤄지는 분자, 반도체, 그리고 생물질의 동역학을 관찰하는데 사용되고 있다. 하지만, 펨토초 레이저가 가지는 또다른 장점인 넓은 스펙트럼을 이용한 양자제어기술은 사용되지 않았다. 이 논문에서는 이차원 푸리에 분광학과 양자제어기술의 접목을 통해 얻게 되는 강력한 장점에 대해 서술하였다. 발전된 이차원 푸리에 분광학의 관점에서 보자면, 양자계를 이루는 여러 상태함수 중 특정 상태함수를 여기시키는 준비과정을 통해 복잡한 과정을 단순화하여 볼 수 있으며, 재단된 펨토초 레이저를 통해 상태함수간 연결세기를 조절할 수 있음을 알칼리 원자(루비듐)에 적용하여 실험적으로 보였다. 양자제어기술의 발전 관점에서 보면, 기존 방식으로는 측정의 어려움으로 인하여 연구가 진행되지 못하던 V-형 양자계에서 양자함수의 변화를 주도하는 1차 천이속에서 여기상태함수간의 2차 천이를 성공적으로 양자제어함과 동시에 측정할 수 있음을 보였다. 이 과정에서 천이의 절대값만이 아니라, 양자물리에서 매우 중요한 요소인 위상의 직접적인 측정도 가능함을 보였다. 더 나아가, V-형 양자계에서 여기상태함수간의 2차 천이는 재단된 펨토초 레이저의 위상이 미분된 형태로 정리되어 2레벨 양자계에서 보여지는 결맞는 과도 현상으로 해석됨을 보였다.

본 논문을 통해 단순화된 모델인 알칼리 원자에서 시연된 이차원 푸리에 변환 양자 제어 분광학을 이용하여, 반도체 V-형 양자계, 더 나아가 다단레벨구조 양자계에서의 양자제어를 통해 다중양자제어 등 양자전산으로의 응용을 기대하고 있다. 또한 복잡한 구조를 갖는 분자 또는 박테리아와 같은 생물질, 광합성 물질 등에서 복잡한 연결 과정을 단순화하고 조절하는 기술을 통해, 더 깊은 이해에 필요한 정보를 얻음으로써 분자동역학, 생물질의 연결구조, 그리고 효과적인 광합성 방식을 이해하고 얻을 수 있으리라 기대한다.